Automated Segmentation and Pathology Detection in Ophthalmic Images

A DISSERTATION
SUBMITTED TO THE FACULTY OF THE GRADUATE SCHOOL
OF THE UNIVERSITY OF MINNESOTA
BY

Sohini Roy Chowdhury

IN PARTIAL FULFILLMENT OF THE REQUIREMENTS
FOR THE DEGREE OF
Doctor of Philosophy

Professor Keshab K. Parhi, Advisor; Dr. Dara D. Koozekanani, Co-advisor

July, 2014

Acknowledgements

First of all, I would like to thank my advisor Professor Keshab K. Parhi for his continued guidance, support and encouragement for my work. I also would like to thank my co-advisor Dr. Dara D. Koozekanani for his constant guidance and inputs that helped me hone my skills of retinal image processing.

I would like to thank Professor Mostafa Kaveh and Professor Jarvis Haupt for their support as members of my Ph.D. committee. I would like to thank Dr. Salma Radwan, Dr. Sam Kuchinka and Dr. Michael Reinsbach for providing manually annotated data sets and helping me understand retinal image diagnostics. I would like to thank the Graduate School, the Department of Electrical and Computer Engineering and The Department of Ophthalmology and Vision Neurosciences at the University of Minnesota for their financial support.

I would like to thank my parents, my brother, sister-in-law and little nephew for their love and unwavering support through my trying times. I want to thank my fiance and in-laws for their unquestioned affection and constant inspiration for perfection.

I want to thank my lab mates Bo Yuan, Tingting Xu, Manohar Ayinala, Shu-Hsein Chu, Yin Liu, Yingjie Lao, Zisheng Zhang and Chuan Zhang for their friendship, enlightening talks about research and the future ahead.

Last, but not the least, I want to thank my friends Ayan Paul, Rajasree Roy Burman, Shubharajit Roychowdhury, Sanjoy Dey for their friendship and kindness. I want to thank Somnath Kundu for the many long walks across Minneapolis and for being such a worthy accomplice as graduate school munchies. I want to thank Lucy Marie, Joseph Bennett and little Jonah Reed Bennett for cheering me up at all moments, especially when it meant the most.

Abstract

Computer-aided medical diagnostic system design is an emerging inter-disciplinary technology that assists medical practitioners for providing quick and accurate diagnosis and prognosis of pathology. Since manual assessments of digital medical images can be both ambiguous and time-consuming, computer-aided image analysis and evaluation systems can be beneficial for baseline diagnosis, screening and disease prioritization tasks. This thesis presents automated algorithms for detecting ophthalmic pathologies pertaining to the human retina that may lead to acquired blindness in the absence of timely diagnosis and treatment. Multi-modal automated segmentation and detection algorithms for diabetic manifestations such as Diabetic Retinopathy and Diabetic Macular Edema are presented. Also, segmentation algorithms are presented that can be useful for automated detection of Glaucoma, Macular Degeneration and Vein Occlusions. These algorithms are robust to normal and pathological images and incur low computationally complexity.

First, we present a novel blood vessel segmentation algorithm using fundus images that extracts the major blood vessels by applying high-pass filtering and morphological transforms followed by addition of fine vessel pixels that are classified by a Gaussian Mixture Model (GMM) classifier. The proposed algorithm achieves more than 95% vessel segmentation accuracy on three publicly available data sets. Next, we present an iterative blood vessel segmentation algorithm that initially estimates the major blood vessels, followed by iterative addition of fine blood vessel segments till a novel stopping criterion terminates the iterative vessel addition process. This iterative algorithm is specifically robust to thresholds since it achieves 95.35% vessel segmentation accuracy with 0.9638 area under ROC curve (AUC) on abnormal retinal images from the publicly available STARE data set.

We propose a novel rule-based automated optic disc (OD) segmentation algorithm that detects the OD boundary and the location of vessel origin (VO) pixel. This algorithm initially detects OD candidate regions at the intersection of the bright regions and the blood vessels in a fundus image subjected to certain structural constraints, followed by the estimation of a best fit ellipse around the convex hull that combines all the

detected OD candidate regions. The centroid of the blood vessels within the segmented OD boundary is detected as the VO pixel location. The proposed algorithm results in an average of 80% overlap score on images from five public data sets.

We present a novel computer-aided screening system (DREAM) that analyzes fundus images with varying illumination and fields of view, and generates a severity grade for non-proliferative diabetic retinopathy (NPDR) using machine learning. Initially, the blood vessel regions and the OD region are detected and masked as the fundus image background. Abnormal foreground regions corresponding to bright and red retinopathy lesions are then detected. A novel two-step hierarchical classification approach is proposed where the non-lesions or false positives are rejected in the first step. In the second step, the bright lesions are classified as hard exudates and cotton wool spots, and the red lesions are classified as hemorrhages and micro-aneurysms. Finally, the number of lesions detected per image is combined to generate a severity grade. The DReAM system achieves 100% sensitivity, 53.16% specificity and 0.904 AUC on a publicly available MESSIDOR data set with 1200 images. Additionally, we propose algorithms that detect post-operative laser scars and fibrosed tissues and neovascularization in fundus images. The proposed algorithm achieves 94.74% sensitivity and 92.11% specificity for screening normal images in the STARE data set from the images with proliferative diabetic retinopathy (PDR).

Finally, we present a novel automated system that segments six sub-retinal thickness maps from optical coherence tomography (OCT) image stacks of healthy patients and patients with diabetic macular edema (DME). First, each image in the OCT stack is denoised using a Wiener Deconvolution algorithm that estimates the speckle noise variance using a Fourier-domain based structural error. Next, the denoised images are subjected to an iterative multi-resolution high-pass filtering algorithm that detects seven sub-retinal surfaces in six iterative steps. The thicknesses of each sub-retinal layer for all scans from a particular OCT stack are then combined to generate sub-retinal thickness maps. Using the proposed system the average inner sub-retinal layer thickness in abnormal images is estimated as $275\mu m$ ($r = 0.92$) with an average error of 9.3 μm, while the average thickness of the outer segments in abnormal images is estimated as 57.4 μm ($r = 0.74$) with an average error of 3.5 μm. Further analysis of the thickness maps from abnormal OCT image stacks demonstrates irregular plateau

regions in the inner nuclear layer (INL) and outer nuclear layer (ONL), whose area can be estimated with $r = 0.99$ by the proposed segmentation system.

Contents

List of Tables

List of Figures

Chapter 1

Introduction

1.1 Introduction

Computer-aided diagnosis (CAD) has become a vital part of medical evaluations and pathology detection in the United States [1]. Systematic use of CAD systems since 1980s has caused a significant change in the utilization of the computer output for pathology diagnosis, disease prognosis and treatment prioritization. Automated pathology detection and screening systems assist in interpretation of the medical signals, achieving a baseline evaluation and automatically analyzing disease severity, which in turn helps to prioritize patients for treatment follow-ups. Examples of popular CAD systems include analysis of X-ray, Magnetic Resonance Imaging (MRI) and Ultrasound images.

Medical images can be considered as 2-dimensional signals from a particular part of the human body that are accompanied by significant background noise from other neighboring parts of the body. Thus, automated analysis of medical images involves elegant solutions engineered from the concepts of digital signal processing and machine-learning. Studies in [2] have shown that automated ophthalmic screening programs alone could save the US healthcare budget nearly 400 million USD per year. Additionally, automated prioritization of eye-care delivery could reduce time delays in treatment by 50%, thereby significantly reducing the chances of acquired blindness [2]. With such increasing costs of health care, research dedicated towards engineering optimal solutions for ophthalmic image analysis will lead to faster and cheaper diagnostic systems and cost-effective treatment delivery. An example of an existing opthalmic fundus imaging

system is shown in Fig. 1.1.

Figure 1.1: An Ophthalmic imaging system for the Retina (anterior portion of the eye). The acquired image is called a fundus image.

In this work, automated algorithms are presented for the analysis of two separate modalities of ophthalmic images. These images capture the human retina, or the anterior part of the eye that is sensitive to light and that triggers nerve impulses of vision that are carried to the brain by the optic nerve. Retinal pathologies may be triggered as symptoms of prolonged diseases like diabetes, hypertension, high cholesterol etc., causing blood vessel leakage or hemorrhaging, impacting the structure and functionalities of the retinal arteries or veins, accumulation of lipids on the retinal surfaces or impacting the axiomatic plasma. If untreated or undiagnosed in a timely manner, such retinal abnormalities can lead to acquired blindness. Examples of change in vision due to retinal pathologies are shown in Fig. 1.2.

The first modality of retinal images analyzed in this work is retinal fundus imaging. Fundus images typically include the optic disc (OD, head of the optic nerve), macula (the spot which is most sensitive to vision) and blood vessels as shown in Fig. 1.3

Figure 1.2: Changes in vision due to retinal pathologies [Source:http://www.ucdenver.edu].

(a). Automated analysis of fundus images aids detection of abnormalities caused by pathologies. Abnormal regions that appear due to diabetic retinopathy (DR) are shown in Fig. 1.3 (b). Algorithms based on the principles of image denoising, spatial filtering and segmentation can be used to separate the abnormal regions of interest followed by machine-learning based algorithms that guide the decision making process regarding the presence or absence of a particular retinal pathology.

Automated detection of the OD aids analysis of the changes caused by pathologies such as Glaucoma and proliferative diabetic retinopathy (PDR). Automated segmentation of blood vessels helps analysis of the blood vessel width, vessel density, tortuosity etc. for detection of disease such as PDR, Retinopathy of Prematurity (RoP), retinal vein occlusions (RVO) and age-related macular degeneration (AMD). Also, detection of

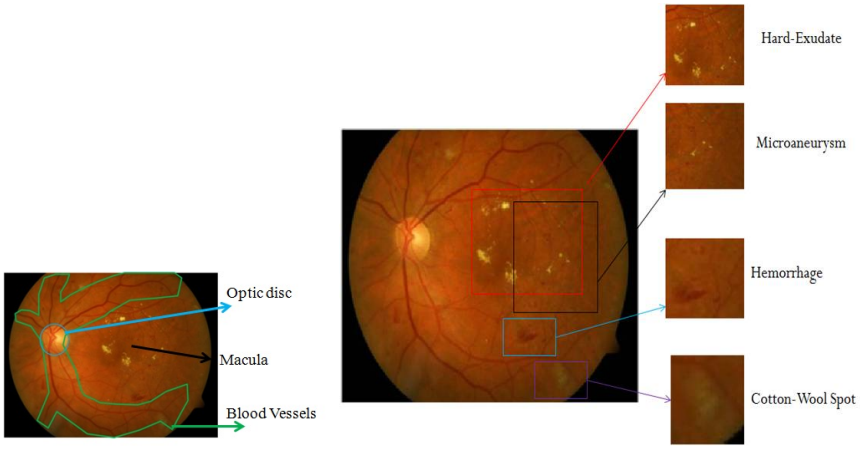

Figure 1.3: Example of fundus images. (a) Anatomy of a fundus image. (b) Abnormalities in fundus image due to DR.

bright and red abnormalities that occur as manifestation of non-proliferative diabetic retinopathy (NPDR) using automated algorithms can help screening and prioritization of patients based on disease severity.

The second modality of images under analysis is acquired using Optical Coherence Tomography (OCT). An example of OCT images is shown in Fig. 1.4. This imaging modality captures the micrometer-resolution of the third dimension, or the depth of retinal tissue. OCT is an interferometric technique that measures the depth of sub-retinal layers in the form of lateral scans. These lateral scans when combined can represent the 3-dimensional view of the retina that can be then used to locate and treat macular pathologies. Automated segmentation and analysis of OCT images can aid clinical studies regarding the progression of diseases over time, the impact of treatment and pathology localization for laser surgeries.

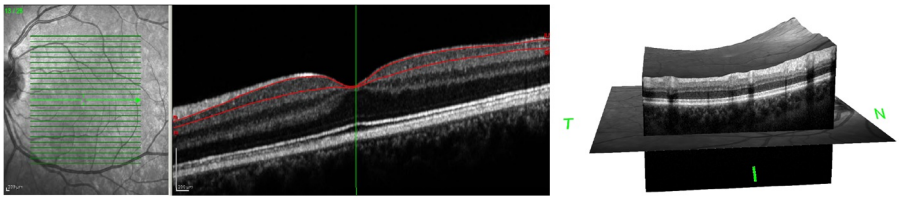

Figure 1.4: Example of the OCT imaging modality. Several lateral scans are combined to obtain a 3-D retinal microstructure.

1.2 Summary of Contributions

The automated segmentation and pathology detection algorithms presented in this thesis can be beneficial for assisting primary eye-care providers in obtaining a quick automated screening result or semi-automated screening capability for diseases such as diabetic retinopathy (DR). Also, telemedicine, with distributed, remote retinal fundus imaging in local primary care offices and centralized grading by eye care specialists may increase access to screening and thus necessary treatment [3]. Automated retinal screening systems such as the ones proposed in this thesis will help augment a telemedicine approach using a web-based interface, where retinal images can be uploaded, that results in end reports that can be then analyzed by specialists to provide quicker evaluations. An example of such a web-based telemedicine system is shown in Fig. 1.5.

Our main contributions can be classified under three main categories: automated segmentation of various anatomical regions of fundus images, automated screening systems for detecting severity and presence of pathologies such as NPDR and PDR using fundus images, and automated segmentation of the sub-retinal micro-structure to aid clinical analysis of OCT images from patients with diabetic macular edema (DME). The contributions made in each of these categories are summarized below.

1.2.1 Segmentation of Retinal Anatomical Regions in Fundus Images

Certain retinal pathologies cause variations in the anatomical regions in fundus images. For instance, glaucoma causes variation in the cup-to-disc ratio of the optic disc, or neovascularization at the disc (NVD) caused by PDR, causes a dense mesh of new blood

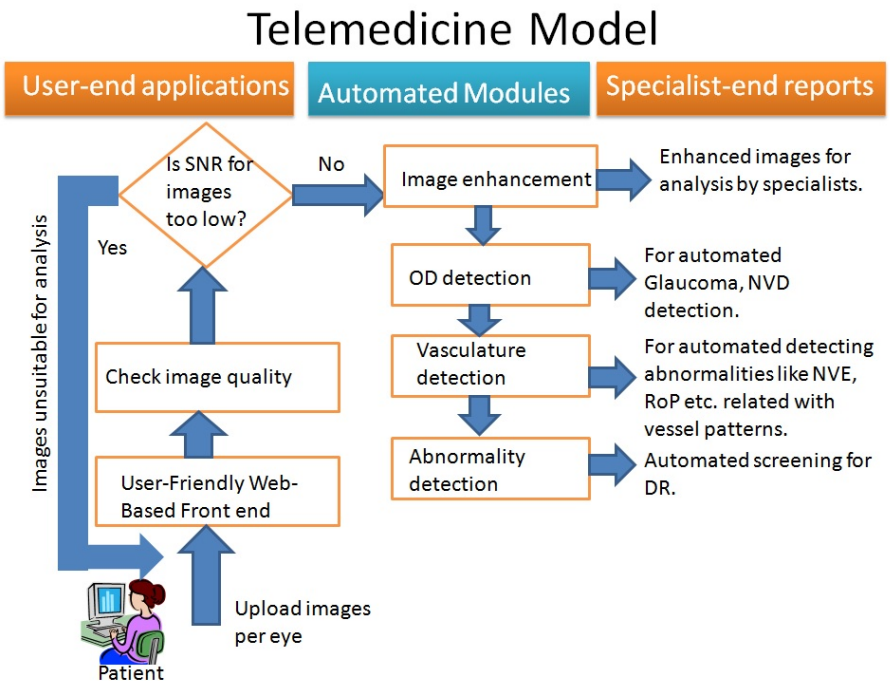

Figure 1.5: Schematic for a web-based telemedicine system.

vessels in and around the optic disc. Besides, pathologies such as neovascularization elsewhere (NVE), caused by PDR, or vein occlusions cause changes in the blood vessel patterns. In this thesis we present algorithms that utilize domain knowledge and image processing algorithms to extract the basic anatomical features such as the optic disc, or the blood vessel structure to detect the presence of pathology. This problem is challenging since fundus images suffer from variations in contrast and illumination based on the artifacts introduced by the non-mydriatic cameras, variations due to different fields of view (FOV) and due to the presence of multiple abnormalities that hinder the detection of the exact region of interest. There are two primary advantages of the algorithms presented in this thesis. First, the algorithms are generalizable and robust to variations due to imaging limitations or due to retinal abnormalities. Second, the algorithms have low computational complexity, thus making them preferable for automated screening systems.

1.2.2 DR Screening Systems using Funds Images

Guidelines from the American Diabetes Association (ADA) specify that all patients with diabetes must be screened annually for DR. However, 90% of the images thus acquired has no signs of DR. Thus, automated screening systems for DR can be used to screen the patients with DR and thereby help to prioritize and enhance the resourcefulness of eye-care delivery. In this thesis, we introduce the DREAM (Diabetic Retinopathy Analysis using Machine Learning [3]) system that is capable of screening patients with mild, moderate to severe NPDR from the patients with no DR. Another screening system that detects the presence of PDR based on the presence of post-operative laser scar marks, fibrosed tissue, NVD or NVE is also presented.

1.2.3 Automated Segmentation of OCT images

OCT images typically suffer from low signal to noise ratio (SNR) owing to the micron-level resolution of the images. Additionally, pathologies such as DME causes variations in the retinal micro-structure poses challenges for automated segmentation algorithms that are robust to both normal and pathological OCT images. In this thesis, we present automated denoising and segmentation algorithms that utilize adaptive thresholds for enhancing the image SNR and segmenting the sub-retinal layers in normal and abnormal OCT images with DME. These algorithms can be beneficial for conducting clinical studies that monitor the progression of pathology over time.

1.3 Outline of this Thesis

The thesis is outlined as follows. An automated blood vessel segmentation algorithm that uses pixel-based classification for vessel detection is presented in Chapter 2. The pixel-based features that are capable of discriminating finer vessel pixels from the background pixels are described.

Chapter 3 introduces an iterative algorithm that iteratively detects and adds fine blood vessels to an existing vessel estimate using fundus images. This iterative algorithm is capable of detecting fine blood vessels with high precision in pathological images.

Chapter 4 presents a rule-based algorithm for detecting the OD in normal and

pathological fundus images. This algorithm detects the exact OD boundary and the point of vessel origin.

Chapter 5 presents the DREAM system for screening images with NPDR from the images without any retinopathy. This three-stage system separates the image background from the foreground, identifies region-based features that discriminate bright lesions and red lesions that are caused by NPDR, and grades the severity of NPDR.

Chapter 6 presents a screening system for detection of PDR. This system utilizes the iterative vessel segmentation algorithm from Chapter 3 to detect the fine vessel structures followed by rule-based decision regarding the presence of NVD and NVE. Also the presence of laser scars and fibrosis are detected in fundus images.

Chapter 7 presents an automated denoising and segmentation system for OCT image stacks. OCT stacks from healthy eyes and pathological eyes (with DME) are segmented to extract seven sub-retinal surfaces and six sub-retinal layers. Thickness maps constructed from the segmented sub-retinal layers from an OCT stack of images are also analyzed.

Finally, Chapter 8 presents conclusions regarding all the automated algorithms presented in this thesis and provides directions for future work.

Chapter 2

Automated Vessel Segmentation: A Classification Approach

2.1 Introduction

Analysis of the retinal blood vessels (vasculature) from fundus images has been widely used by the medical community for diagnosing complications due to hypertension, arteriosclerosis, cardiovascular disease, glaucoma, stroke and diabetic retinopathy (DR) [4]. According to the American Diabetes Association, DR and glaucoma are the leading causes of acquired blindness among adults aged 20-74 years with estimates of 4.2 million Americans having DR and 2.3 million having glaucoma in 2011 [5]. Automated blood vessel segmentation systems can be useful in determining variations in the blood vessels based on the vessel branching patterns, vessel width, tortuosity and vessel density as the pathology progresses in patients [6]. Such analyses will guide research towards analyzing patients for hypertension [7], variability in retinal vessel diameters due to a history of cold hands and feet [8], and flicker responses [9].

Existing automated detection systems for non-proliferative DR detection, such as [10] [3], require masking of the vasculature to ensure that the blood vessels are not mistaken for red lesions that are caused by DR. Also, automated detection of proliferative DR requires analysis of the density, vessel width and tortuosity of the blood vessels. A fast and accurate segmentation algorithm for detecting the blood vessels is necessary for such automated detection and screening systems for retinal abnormalities

such as DR. Some existing unsupervised vessel segmentation methods have achieved up to 92% segmentation accuracy on normal retinal images by line-detector and template matching methods [11] that are computationally very fast. However, increasing the segmentation accuracy above 92% for abnormal retinal images with bright lesions (exudates and cotton wool spots), or red lesions (hemorrhages and microaneurysms), or variations in retinal illumination and contrast, while maintaining low computational complexity is a challenge. In this chapter we separate the vessel segmentation problem into two parts, such that in the first part, the thick and predominant vessel pixels are extracted as major vessels and in the second part, the fine vessel pixels are classified using neighborhood-based and gradient-based features.

This chapter makes two major contributions. First, the number of pixels under classification is significantly reduced by eliminating the major vessels that are detected as the regions common to thresholded versions of high-pass filtered image and morphologically reconstructed negative fundus image. This operation is *key* to more than 90% reduction in segmentation time complexity compared to the existing methods where all the vessel pixels are classified in [12], [13]. Additionally, the proposed method is *more* robust to vessel segmentation in abnormal retinal images with bright or red lesions than thresholded high-pass filtered and tophat reconstructed images. The second major contribution is the identification of an optimal 8-feature set for classification of the fine blood vessel pixels using the information regarding the pixel neighborhood and first and second-order image gradients. These features reduce the dependence of vessel pixel classification on the training data and enhance the robustness of the proposed vessel segmentation for test images with 45^o, 35^o and 30^o fields of view (FOV), and for images with different types of retinal abnormalities.

The organization of this chapter is as follows. In Section 2.2, the existing automated vessel segmentation algorithms in the literature are reviewed. The proposed method and materials are described in Section 2.3. In section 2.4, the experimental setup for analyzing the performance of vessel segmentation and results are presented. Finally, in Section 2.5, discussion and conclusions are presented.

2.2 Prior Work

The problem of automated segmentation of retinal blood vessels has received significant attention over the past decade [14]. All prior works for vasculature segmentation can be broadly categorized as *unsupervised* and *supervised* approaches.

In the unsupervised methods category, algorithms that apply matched filtering, vessel tracking, morphological transformations and model-based algorithms are predominant. In the matched filtering-based method in [15], a 2-D linear structuring element is used to extract a Gaussian intensity profile of the retinal blood vessels, using Gaussians and their derivatives, for vessel enhancement. The structuring element is rotated 8-12 times to fit the vessels in different configurations to extract the boundary of the vessels. This method has high time complexity since a stopping criterion is evaluated for each end pixel. In another vessel tracking method [16], Gabor filters are designed to detect and extract the blood vessels. This method suffers from over-detection of blood vessel pixels due to the introduction of a large number of false edges. A morphology-based method in [17] combines morphological transformations with curvature information and matched-filtering for center-line detection. This method has high time complexity due to the vessel center-line detection followed by vessel filling operation, and it is sensitive to false edges introduced by bright region edges such as optic disc and exudates. Another morphology based method in [18] uses multiple structuring elements to extract vessel ridges followed by connected component analysis. In another model-based method [19], blood vessel structures are extracted by convolving with a Laplacian kernel followed by thresholding and connecting broken line components. An improvement of this methodology was presented in [20], where the blood vessels are extracted by the Laplacian operator and noisy objects are pruned according to center lines. This method focuses on vessel extraction from images with bright abnormalities, but it does not perform very effectively on retinal images with red lesions (such as hemorrhages or microaneurysms). The method in [21] presents perceptive transformation approaches to segment vessels in retinal images with bright and red lesions.

A model-based method in [22] applies locally adaptive thresholding and incorporates vessel information into the verification process. Although this method is more

generalizable than matched-filter based methods, it has a lower overall accuracy. Another model-based vessel segmentation approach proposed in [23] uses active contour models, but suffers from computational complexity as well. Additionally, multi-scale vessel segmentation methods proposed in [24] and [25] use neighborhood analysis and gradient-based information for determining the vessel pixels. All such unsupervised methods are either computationally intensive or sensitive to retinal abnormalities.

The supervised vessel segmentation algorithms classify pixels as vessel and non-vessel. In [26], the k-Nearest Neighbor (kNN) classifier uses a 31-feature set extracted using Gaussians and their derivatives. The approach in [27] improved this method by applying ridge-based vessel detection. Here each pixel is assigned to its nearest ridge element, thus partitioning the image. For each pixel, a 27 feature set is then computed and is used by a kNN classifier. Both these methods are slowed down by the large size of the feature sets. Also, these methods are training data dependent and sensitive to false edges. Another method presented in [28] uses Gaussian Mixture Model (GMM) classifier and a 6-feature set extracted using Gabor-wavelets. This method is also training data dependent, and it requires hours for training GMM models with a mixture of 20 Gaussians. The method in [29] uses line operators and a support vector machine (SVM) classifier with a 3-feature set per pixel. This method is very sensitive to the training data and is computationally intensive due to the SVM classifiers. The method in [12] applies boosting and bagging strategies with 200 decision trees for vessel classification using a 9-feature set extracted by Gabor filters. This method suffers from high computational complexity as well due to the boosting strategy. The only other supervised method that is independent of the training data set is proposed in [13] that applies neural network classifiers using a 7-feature set extracted by neighborhood parameters and a moment invariants-based method. The proposed vessel segmentation method is motivated by the method in [13] to design a segmentation algorithm that has low dependence on training data and is computationally fast. So far, computational complexity of vessel segmentation algorithms has been addressed only in [11] and [21]. In this chapter we reduce the number of pixels under classification, and identify an optimal feature set to enhance the consistency in the accuracy of blood vessel segmentation, while maintaining a low computational complexity.

2.3 Method and Materials

For every color fundus photograph, the proposed vessel segmentation algorithm is performed in three stages. In the first stage, two thresholded binary images are obtained: one by high-pass filtering and another by tophat reconstruction of the red regions in the green plane image. The regions common to the two binary images are extracted as the major vessels and the remaining pixels in both binary images are combined to create a vessel sub-image. In the second stage, the pixels in the vessel sub-image are subjected to a 2-class classification. In the third post-processing stage, all the pixels in the sub-image that are classified as vessels by the classifier are combined with the major vessels to obtain the segmented vasculature. Depending on the resolution of the fundus images, in the post-processing stage, the segmented vessels are further enhanced to ensure higher vessel segmentation accuracy. Here, the proposed vessel segmentation algorithm is evaluated using three publicly available data sets.

2.3.1 Data

The vessel segmentation algorithm is trained and tested with the following data sets that have been manually annotated for the blood vessel regions.

- STARE [15] data set contains 20 images with 35^o FOV that are manually annotated by two independent human observers. Here, 10 images represent patients with retinal abnormalities (STARE Abnormal). The other 10 images represent normal retina (STARE Normal).

- DRIVE [27] data set contains 40 images with 45^o FOV. This data set is separated by its authors into a training set (DRIVE Train) and a test set (DRIVE Test) with 20 images in each set. The DRIVE Train set of images are annotated by one human observer while the DRIVE Test data set is annotated by two independent human observers.

- CHASE_DB1 [30] data set contains 28 images with 30^o FOV corresponding to two images per patient (one image per eye) for 14 children. Each image is annotated by two independent human observers [12].

2.3.2 Problem Formulation

The first pre-processing stage requires the green plane of the fundus image scaled in [0, 1] (I), and a fundus mask (g). In the green plane image, the red regions corresponding to the blood vessel segments appear as dark pixels with intensities close to 0. In such cases, the fundus mask removes the dark background region from the photographs and helps to focus attention to the retinal region only. The fundus mask is superimposed on image I followed by contrast adjustment and vessel enhancement, resulting in a vessel enhanced image I_e. The vessel enhancement operation involves squaring each pixel intensity value and re-normalizing the image in [0, 1] range thereafter. This is a vital operation since the dark pixels corresponding to the vessel regions (with pixel values closer to 0), when squared, become darker, while the non-vessel bright regions become brighter, hence resulting in the enhancement of the blood vessel regions.

To extract the dark blood vessel regions from I_e, two different pre-processing strategies are implemented. First, a smoothened low-pass filtered version of I_e ($LPF(I_e)$) is subtracted from I_e to obtain a high-pass filtered image. Here, the low-pass filter is a median filter with window size [20x20] as used in [10] [31]. This high-pass filtered image is thresholded to extract pixels less than 0, and the absolute pixel strengths of the thresholded image are contrast adjusted to extract the vessel regions. This is referred to as the pre-processed image H (2.1). For the second pre-processed image, the red regions corresponding to the dark pixels are extracted from the negative of image I_e, thus resulting in image R. Next, 12 linear structuring elements each of length 15 pixels and 1 pixel width and angles incremented by 15^o from 0 through 180^o are used to generate tophat reconstructions of R [17] [12]. The length of 15 pixels for the linear structuring element is chosen to approximately fit the diameter of the biggest vessels in the images [12]. For each pixel location, the reconstructed pixel with the highest intensity is selected, thereby resulting in image T (2.2). An example of the two pre-processed images H and T is shown in Fig. 2.1. These two pre-processed images H, and T can be thresholded to obtain baseline unsupervised models to analyze the importance of the proposed method in the following sections. Both the pre-processed images H and T are thresholded for pixel values greater than 'p' to obtain binary images H' and T' (2.3-2.4). For images from DRIVE and STARE and CHASE_DB1 data sets, '$p = 0.2$', which ensures the red regions to be highlighted in the vessel enhanced binary images. Next, the intersecting

regions between the pre-processed binary images H' and T' are retained as the major portions of the blood vessels, or the major vessels ($\hat{V}$) (2.5). Once the major vessels are removed from the two binary images, the resulting images are called vessel sub-images H_1 corresponding to binary image H' (2.6) and sub-image T_1 corresponding to binary image T' (2.7), respectively. These steps are summarized in equations (2.1)-(2.7).

In the second stage, the pixels in sub-images H_1 and T_1 are combined to form a vessel sub-image C (2.8), and the pixels in C are classified using a GMM classifier that classifies each pixel as vessel (class 1) or non-vessel (class 0). Thus, for all pixels in C, a GMM classifier is trained once using the images from the DRIVE Train set of images and tested on the DRIVE Test image set, STARE image set, and CHASE_DB1 image set, independently, to identify the vessel pixels in each test image. The optimal feature set selection for vessel pixel classification is described in the following subsection. The pixels in sub-image C that are classified as vessel result in image $\hat{V}'$ (2.9).

$$\forall(x,y), H(x,y) = abs(I_e(x,y) - LPF(I_e(x,y)) < 0) \tag{2.1}$$

$$R = (1 - I_e) \circ g, T = tophat(R) \tag{2.2}$$

$$\forall(x,y), \qquad H'(x,y) = \begin{cases} 1 & : H(x,y) > p \\ 0 & : Otherwise. \end{cases} \tag{2.3}$$

$$T'(x,y) = \begin{cases} 1 & : T(x,y) > p \\ 0 & : Otherwise. \end{cases} \tag{2.4}$$

$$\hat{V}(x,y) = \begin{cases} 1 & : H(x,y) = T(x,y) = 1 \\ 0 & : Otherwise. \end{cases} \tag{2.5}$$

$$\Rightarrow \hat{V} = H' \cap T'.$$

$$H_1(x,y) = \begin{cases} 1 & : H'(x,y) = 1 \ \& \quad \hat{V}(x,y) = 0 \\ 0 & : Otherwise. \end{cases} \tag{2.6}$$

$$T_1(x,y) = \begin{cases} 1 & : T'(x,y) = 1 \ \& \quad \hat{V}(x,y) = 0 \\ 0 & : Otherwise. \end{cases} \tag{2.7}$$

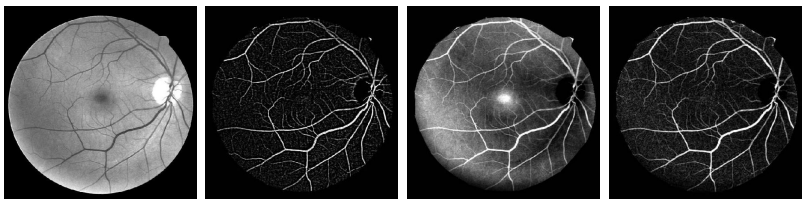

(a) (b) (c) (d)

Figure 2.1: Each fundus image is subjected to contrast adjustment and pixel enhancement followed by high-pass filtering and tophat reconstruction. (a) Contrast adjusted vessel enhanced image (I_e). (b) High-pass filtered image (H). (c) Red regions enhanced image (R). (d) Tophat reconstructed version of R (T).

$$C(x,y) = \begin{cases} 1 & : H_1(x,y) = 1 \text{ or } \quad T_1(x,y) = 1 \\ 0 & : Otherwise. \end{cases} \tag{2.8}$$
$$\Rightarrow C = H_1 \cup T_1.$$

$$\hat{V}'(x,y) \leftarrow \text{GMMclassify}(C(x,y)). \tag{2.9}$$

$$\hat{V}_f = \hat{V} \cup \hat{V}'. \tag{2.10}$$

In the third post-processing stage, sub-image $\hat{V}'$ representing all the pixels in C that are classified as vessel, are combined with the major vessels $\hat{V}$ to obtain the segmented vasculature $\hat{V}_f$ (2.10). Finally, the complete segmented blood vessel $\hat{V}_f$ is post-processed such that the regions in the segmented vasculature with area greater that 'a' are retained while smaller regions are discarded. The values of 'a' were empirically determined as [20, 40, 50], for the images from DRIVE, STARE and CHASE_DB1 data sets, respectively.

The images from the CHASE_DB1 data set are different from the DRIVE and STARE set of images since all these images are centered at the papilla and they have thicker blood vessels. Hence, to post-process images from CHASE_DB1 data set, the segmented vasculature $\hat{V}_f$ is superimposed on the tophat reconstructed image T, and the resulting image ($\hat{V}_f \circ T$) is region grown at pixel threshold value 240 followed by vessel filling [13]. The performance of vasculature segmentation on each image is then analyzed with reference to manually marked blood vessels by human observers in image

V_f. This three-stage vessel segmentation algorithm is demonstrated for an image from the DRIVE Test data set in Fig. 2.2.

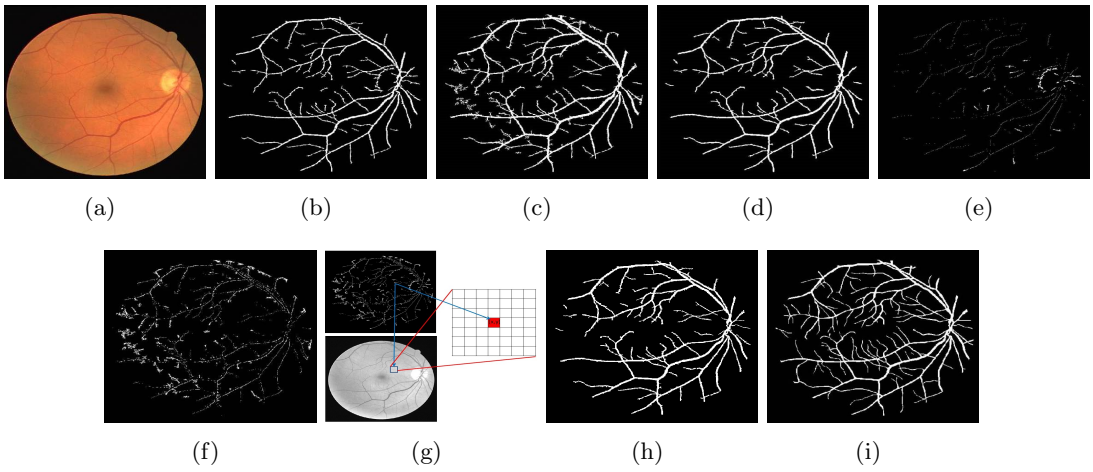

Figure 2.2: Proposed vasculature segmentation algorithm. (a) Original image. (b) Binary image from high-pass filtering (H'). (c) Binary image from top hat reconstruction (T'). (d) Major vessels are the intersecting regions between H' and T' ($\hat{V}$). (e) Sub-image regions remaining in H' after masking out $\hat{V}$ (H_1). (f) Sub-image regions remaining in T' after masking out $\hat{V}(T_1)$. (g) Example of feature extraction for each pixel in sub-image C using a window size $s = 7$. (h) Post-processed vasculature after classification of the sub-image pixels and combining the major vessels ($\hat{V_f}$). (i) Manually marked vessels (V_f).

2.3.3 Pixel-based Classification

Blood vessels in fundus images can be broadly categorized into two kinds. The first category includes wide and thick vessels that are easily distinguishable from the neighboring based on the pixel intensities. The second category includes the fine small blood vessel branches that are not very distinct against the neighboring pixels. The extraction of major vessels extraction ensures segmentation of the first category of blood vessels while the classification of the pixels in the vessel sub-image aids identification of the second category of fine vessels.

The proposed approach of separating the methods for identifying the thick and

fine blood vessel regions enhances the robustness of vessel segmentation on normal and abnormal retinal images in two ways. First, the major vessel regions comprising of 50-70% of the total blood vessel pixels are segmented in the first stage, thereby significantly reducing the number of sub-image vessel pixels for classification. This reduction in the number of vessel pixels under classification reduces the computational complexity and vessel segmentation error when compared to methods that classify all major and fine vessel pixels alike [13] [12] [29]. Second, the optimal feature set identified for sub-image vessel pixel classification are discriminative for the fine vessel pixel segmentation. These features aid elimination of sub-image vessel pixels from large red lesions and false bright lesion edges in retinal images with pathology.

The most important aspect of sub-image vessel pixel classification is identification of features that classify the fine vessel pixels from false edge pixels. Hence, we analyze the performance of pixel-based features that distinguish a vessel pixel from its immediate neighborhood, and select an optimal feature set that is suitable for fine vessel segmentation in fundus images regardless of their FOV, illumination variability and abnormality due to pathology. These features under analysis and the method for selecting the optimal feature set are described below.

Feature Description

For each pixel '(x,y)' in vessel sub-image C, 57 features are analyzed to detect a discriminative optimal feature set for classifying the vessel pixels. These features utilize the information regarding the pixel neighborhood and pixel gradient to identify a fine vessel pixel from false edge pixels. The neighborhood-based features under analysis are motivated from the supervised segmentation method in [13] where major and fine vessel pixels are classified alike. The gradient-based features have been analyzed in [25] [24] for multi-level vessel pixel identification. In this chapter, the goal is to identify discriminating features for fine vessel classification specifically, and hence, we analyze a range of neighborhood-based features to select the optimal feature set using images from the DRIVE Train data set.

For extracting the neighborhood-based features for each vessel sub-image pixel '(x,y)', 5 features are defined by placing the desired pixel '(x,y)' as the central pixel in a square window of side-length 's' pixels on image I_e. This 2-D window is represented as $W^s_{(x,y)}$,

where the window side length 's' can be varied. We limit the size s to less than 15 pixels since the width of the widest vessel is about 15 pixels in the DRIVE Train data set. The first 4 features (f_1 to f_4) are determined by mean, standard deviation, maximum pixel intensity and minimum pixel intensity among all pixels extracted in the windowed-image $I_e^{W^s_{(x,y)}}$, and are described in (2.11)-(2.13). These features are motivated from the prior work [13], where $s = 9$. The fifth new feature (f_5) introduced in this chapter is a *relative neighborhood discriminator* feature. False edges that are introduced by the edges of bright regions such as exudates and optic disc are discriminated by this function.

$$f_1(s) = \text{mean}(I_e^{W^s_{(x,y)}}), f_2(s) = \text{std. dev}(I_e^{W^s_{(x,y)}}), \tag{2.11}$$

$$f_3(s) = \max(I_e^{W^s_{(x,y)}}), f_4(s) = \min(I_e^{W^s_{(x,y)}}). \tag{2.12}$$

$$\begin{aligned} &\nu(s) = \#\text{pixels in } I_e^{W^s_{(x,y)}}, \\ &\nu_1(s) = [\#\text{pixels in } I_e^{W^s_{(x,y)}} > I_e(x,y)], f_5(s) = \frac{\nu_1(s)}{\nu(s)}. \end{aligned} \tag{2.13}$$

Two other neighborhood-based features, from the prior work [13], that extract moment-invariants based information are defined as f_6 and f_7. For extracting these two features, a square windowed-image with side-length s and centered at pixel '(x,y)' is extracted from the tophat reconstructed image T. In this windowed-image ($T^{W^s_{(x,y)}}$), the '(p+q)'th order moments for second-order moments are defined in (2.14)-(2.17). Here $p+q = 2$. Corresponding to each pixel, the second-order moments invariant-based features f_6 and f_7 as the window side length varies are given in (2.18)-(2.19).

$$\forall(x,y), \quad (p,q) = \{(0,2),(1,1),(2,0)\}, \tag{2.14}$$

$$m_{pq}(s) = \sum_u \sum_v u^p v^q T^{W^s_{(x,y)}}(u,v). \tag{2.15}$$

$$\mu_{p,q}(s) = \sum_u \sum_v (u-\bar{u})^p (v-\bar{v})^q T^{W^s_{(x,y)}}(u,v). \tag{2.16}$$

$$\eta_{pq}(s) = \frac{\mu_{pq}(s)}{\mu_{00}(s)^\gamma}, \quad \gamma = \frac{p+q}{2} + 1 = 2. \tag{2.17}$$

$$\theta_1(s) = \eta_{20}(s) + \eta_{02}(s), f_6(s) = |log(\theta_1(s)))|. \tag{2.18}$$

$$\theta_2(s) = (\eta_{20}(s) + \eta_{02}(s))^2 + 4\eta_{11}(s)^2,$$

$$f_7(s) = |log(\theta_2(s)))|. \tag{2.19}$$

The 7 features $f_1(s)$ to $f_7(s)$ are evaluated for each vessel sub-image pixel by varying window side-lengths $s = [3,5,7,9,11,13,15]$. Also, the pixel intensity $I_e(x,y)$ is another feature. Along with the 50 neighborhood-based features mentioned above, 7 additional gradient based features are also analyzed for vessel pixel classification. For these gradient-based features, the first and second-order gradient images of I_e are extracted. The first-order gradient images in the horizontal and vertical direction are extracted as g_h and g_v, respectively. Next, the second-order gradient images in the horizontal, vertical, and both directions are extracted as g_{hh}, g_{vv}, g_{hv}, respectively. The pixel intensity in the '(x,y)' location of these first and second-order gradient images are 5 gradient-based features. The final two gradient-based features are the Eigen values obtained by the Eigen decomposition of matrix G that is formed using the pixel intensities from the second-order gradient images as shown in (2.20).

$$G = \begin{bmatrix} g_{hh}(x,y) & g_{hv}(x,y) \\ g_{vh}(x,y) & g_{vv}(x,y) \end{bmatrix}. \tag{2.20}$$

Feature Selection

To select the most discriminating features from the 57 pixel-based features described above, we performed feature ranking and leave-one-out double cross-validation [32] on the 20 images from the DRIVE Train data set using GMM classifiers with 2-Gaussians (Gaussian with class label 0 corresponds to non-vessel pixels, Gaussian with class label

1 correspond to vessel pixels). In the first cross-validation step, one image is selected as the validation image and the pixels from its vessel sub-image are used to generate the validation data set. Pixels from the remaining 19 images are used to generate the training data set, hence the name leave-one-out. Corresponding to the 20 images from DRIVE Train data set, 20 such training/validation data sets are thus generated. Each training data set is then subjected to feature ranking using the minimal-redundancy-maximal-relevance (mRMR) criterion [33].

The mRMR criterion is based on mutual information from the individual features, such that, the features are ranked based on the top combination of features that have maximum relevance with the sample class labels and minimum redundancy. The mRMR criterion is chosen for feature ranking over other ranking strategies such as F-score or AdaBoost [32] since the neighborhood-based pixel features are mutually dependent, and the mRMR criterion aims at maximizing the information from these dependent features instead of ranking features independently.

Once the features from the training data set are ranked, GMM classifiers are trained using the top 'F' ranked features, and the classifier is tested on the validation data set. As F is varied from 1 to 57, and the threshold for GMM classifier is varied from 0 to 1 in increments of 0.01, the mean vessel segmentation accuracy (ACC) and the mean pixel classification error across each of the 20 validation images is shown in Fig. 2.3. In Fig. 2.3, we observe that the highest mean $ACC = 0.9541$ and least mean classification error$= 0.0961$ occurs at a threshold of 0.94 with a combination of top 12 features.

Since the feature ranking is done separately for each of the 20 training/validation data sets, hence the top 12 features appearing in each of the 20 sets may be different. To identify the optimal feature set that are common to all the training/validation data sets, feature voting is performed. We observe that by selecting the top F features for each of the 20 training/validation data sets, F_1 unique features are identified across the 20 training data sets. By varying $F = [2, 3, 4, 5, 6, 7, 8, 9, 10]$, we observe the variation in the number of uniquely identified features is $F_1 = [9, 10, 11, 16, 20, 23, 27, 31, 33]$. Here, we observe that by selecting the top 5 features for each training data set, a total of 16 features are uniquely identified. The number of occurrences for each of these 16 features among the 20 training/validation data sets is considered as the feature vote. These 16 features are ranked in decreasing order of their feature vote. In the second

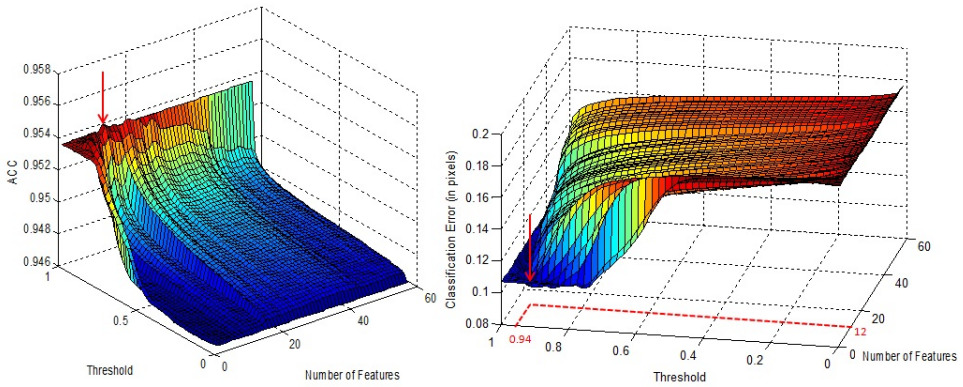

Figure 2.3: Mean ACC and pixel classification error obtained on the validation images in the first cross-validation step. Maximum ACC and minimum classification error occurs for a combination of 12 features and at classifier threshold of 0.94.

cross-validation step, these top 16 voted features are re-analyzed by leave-one-out cross-validation.

For the second cross-validation step, 20 training/validation data sets are re-generated using the top 16 voted features and the mean ACC and classification error on the validation images are shown in Fig. 2.4. In Fig. 2.4 we observe that, the highest mean $ACC = 0.9540$ and lowest mean pixel classification error$= 0.1067$ occurs at a threshold of 0.92 with a combination of top 8 features. These top 8 voted features and their respective votes are given in Table 2.1. At the end of the cross-validation, the 8 top features identified include four neighborhood-based features and four gradient-based features. These 8 features will henceforth be used for classification of vessel pixels from the vessel sub-image derived from test data sets.

2.4 Experimental Evaluation and Results

The performance of the proposed vessel segmentation algorithm is evaluated using the segmented vasculature and the manually marked vessels by the human observers. While manual vessel segmentation can take more than 2 hours [27], automated vessel segmentation algorithms aim to reduce the manual labor while maintaining acceptable accuracy

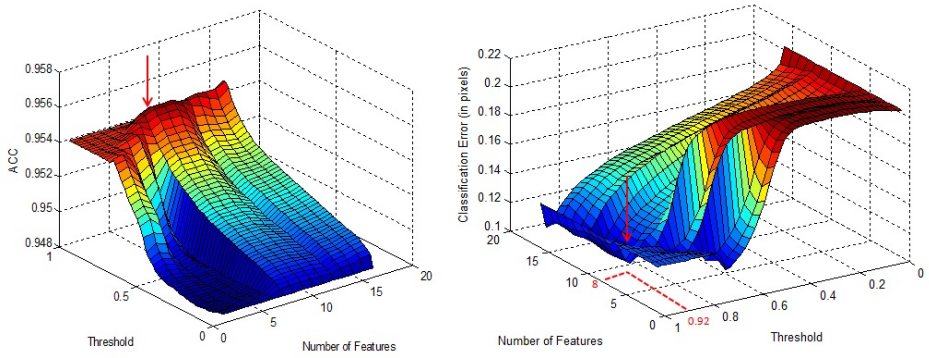

Figure 2.4: Mean ACC and pixel classification error obtained on the validation images in the second cross-validation step. Maximum ACC and minimum classification error occurs with the top 8 voted features and classifier threshold of 0.92.

of vessel segmentation. All prior works have used the manual segmentations of the first human observer for segmentation performance analysis. The vessel segmentation performance of the second human observer with respect to the first human observer within the retinal region is used to standardize the segmentation process.

The performance metrics for assessing the efficiency of the vessel segmentation is computed in terms of the number of vessel pixels that are correctly classified as vessels (true positives, TP), or non-vessels (true negatives, TN), pixels falsely classified as vessels (false positives, FP) and pixels falsely classified as non-vessels (false negatives, FN). Thus, the performance metrics are: pixel-based sensitivity (SEN), specificity (SPEC), ACC of vessel segmentation along with the Area Under the Receiver Operating Characteristic curve (AUC) obtained by varying the threshold in a GMM classifier in steps of 0.02 in range [0,1] [13]. The vessel segmentation time required per image in seconds for implementing the proposed segmentation system in MATLAB on a Laptop with Intel Core i3 processor, 2.6GHz and 2GB RAM is also recorded. The performance metrics of the proposed system are also compared to existing works in the following subsections.

For complete assessment of the proposed supervised vessel segmentation algorithm, we performed the following four sets of experimental evaluations. In the first experiment, the performance metrics of the overall vessel segmentation algorithm is analyzed

Table 2.1: Optimal feature set identified by feature voting and leave-one-out double cross validation.

Rank	Vote	Feature	Meaning
1	20	$f_3(3)$	Maximum pixel value in a square window of side length 3.
2	17	g_{hv}	Second-order gradient in horizontal and vertical directions.
3	13	g_v	First-order gradient in the vertical direction.
4	12	$f_1(5)$	Mean pixel value within a square window of side length 5.
5	7	g_h	First-order gradient in the horizontal direction.
6	6	$f_2(5)$	Standard deviation of pixels in a square window of length 5.
7	6	$f_5(5)$	Relative neighborhood discriminator in a square window of side length 5.
8	6	g_{hh}	Second-order gradient in the horizontal direction.

for all the three data sets. In the second experiment, the segmentation performance of the proposed method on abnormal retinal images is analyzed. In the third experiment, the dependence of the training data set on the vessel segmentation algorithm is analyzed by inter-changing the training and test data sets. In the fourth experiment, the performance of blood vessel segmentation in the peripapillary region is analyzed to assess the importance of the proposed vessel segmentation system for retinal abnormality detection.

2.4.1 Vessel Segmentation Performance

For the proposed vasculature segmentation algorithm, the GMM classifier is trained once with 8 pixel-based features using the vessel sub-images from the DRIVE Train set of images and then subsequent testing of vessel segmentation performance is performed on images from the DRIVE Test, STARE and CHASE_DB1 data sets, separately. In the proposed approach, the GMM classifier aids segmentation of fine blood vessels only and hence it does not need to be retrained on incoming test data set samples. This reduces the dependency of the proposed segmentation algorithm on the training data set when compared to existing supervised approaches where test images are sub-sampled to re-train classifiers [12] [29]. Since GMM classifiers are probabilistic in nature, the

vessel segmentation ACC varies with the threshold. The Receiver Operating Characteristic (ROC) curves in Fig. 2.5 demonstrate the variation in SEN and SPEC of vessel segmentation as classifier threshold varies. We observe that the DRIVE Train data set achieved highest segmentation ACC at a threshold on 0.92 but the test data sets do not achieve best segmentation SEN/SPEC at threshold probability 0.92. For the DRIVE Test, STARE and CHASE_DB1 data sets, the optimal threshold probability values are [0.92, 0.86, 0.82], respectively.

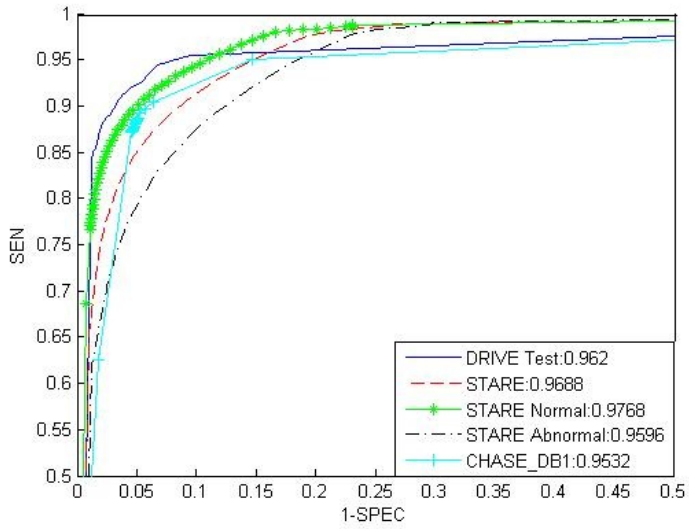

Figure 2.5: ROC curves for blood vessel segmentation on DRIVE test data set and STARE data set.

The performance of blood vessel segmentation for the three test data sets is given in Table 2.2. To analyze the incremental importance of the proposed supervised method over baseline unsupervised approaches, the high-pass filtered image (H) in (1) and the tophat transformed image (T) in (2) are thresholded at pixel values in increments of 0.01 in the range [0, 1]. These baseline unsupervised approaches have the highest mean ACC for all the three data sets at threshold probabilities of approximately [0.36, 0.44] for the high-pass filtered image (H) and tophat transformed image (T), respectively.

In Table 2.2, we observe that the baseline high-pass filtered image and top-hat

Table 2.2: Performance of the Proposed Method on the test data sets. Mean performance metrics and their standard deviation is given in ().

Segmentation	AUC	ACC	SEN	SPEC	Time(s)
DRIVE Test					
Second Observer	-	0.95 (0.005)	0.7798 (0.058)	0.97 (0.008)	-
High-Pass Filter (H)	0.91	0.94 (0.05)	0.5982 (0.055)	0.9854 (0.074)	0.34 (0.04)
Tophat Transform(T)	0.94	0.94 (0.01)	0.5871 (0.076)	0.9868 (0.007)	0.65 (0.08)
Proposed	0.962	0.952 (0.01)	0.7249 (0.0481)	0.983 (0.0071)	3.1 (0.7641)
STARE					
Second Observer	-	0.935 (0.01)	0.9024 (0.054)	0.939 (0.018)	-
High-Pass Filter (H)	0.943	0.932 (0.01)	0.5936 (0.088)	0.9788 (0.016)	0.39 (0.04)
Tophat Transform (T)	0.928	0.926 (0.01)	0.5535 (0.090)	0.9777 (0.012)	0.87 (0.09)
Proposed	0.969	0.952 (0.01)	0.772 (0.071)	0.9726 (0.012)	6.7 (2.417)
STARE Normal					
Second Observer	-	0.931 (0.01)	0.935 (0.01)	0.9304 (0.011)	-
High-Pass Filter (H)	0.948	0.939 (0.01)	0.603 (0.060)	0.9912 (0.003)	0.39 (0.04)
Tophat Transform (T)	0.935	0.930 (0.01)	0.5593 (0.067)	0.9868 (0.003)	0.87 (0.09)
Proposed	0.977	0.958 (0.005)	0.801 (0.06)	0.9785 (0.006)	5.0 (1.325)
STARE Abnormal					
Second Observer	-	0.94 (0.01)	0.87 (0.06)	0.9477 (0.019)	-
High-Pass Filter (H)	0.936	0.924 (0.02)	0.5842 (0.116)	0.9663 (0.024)	0.39 (0.04)
Tophat Transform (T)	0.913	0.923 (0.02)	0.5477 (0.113)	0.9686 (0.021)	0.87 (0.09)
Proposed	0.96	0.945 (0.02)	0.743 (0.07)	0.9718 (0.015)	8.4 (2.104)
CHASE_DB1					
Second Observer	-	0.959 (0.01)	0.829 (0.05)	0.9723 (0.009)	-
High-Pass Filter (H)	0.905	0.929 (0.01)	0.5256 (0.038)	0.9762 (0.004)	1.49 (0.08)
Tophat Transform (T)	0.919	0.929 (0.01)	0.5626 (0.052)	0.9713 (0.003)	0.87 (0.09)
Proposed	0.953	0.953 (0.01)	0.72 (0.04)	0.9824 (0.004)	11.7 (2.515)

transformed image can achieve up to 93% vessel segmentation accuracy across all the data sets. However, further improvement in vessel segmentation ACC and SEN is observed by the proposed major vessel extraction followed by classification of the pixels from the vessel sub-image. This observation is analogous with the work in [29], where SVM classifier is shown to improve the segmentation performance when compared to unsupervised line detector models.

Also, in Table 2.2, we observe for the retinal images with abnormalities due to pathology, such as bright or red lesions as in the STARE Abnormal data set, the baseline unsupervised models H and T introduce a lot of false positives by including the lesions as a part of the vasculature, thereby incurring a low segmentation ACC. In such cases,

the proposed method first extracts the major vessel regions, followed by classification of the fine vessel pixels using neighborhood-based and gradient-based features. Large lesion regions or bright region edges are removed in this classification step and hence, the proposed approach has higher segmentation ACC than the baseline models.

The images from the CHASE_DB1 data set correspond to retinal photographs from children that are centered at the papilla. These images have deeper pigmentation than the other data sets that causes false positive pixels to get introduced by the baseline models. In this case, the proposed method has a superior segmentation ACC due to the classification of vessel sub-images.

The best and worst vessel segmentation examples from all the three test data sets are shown in Fig. 2.6. It is noteworthy that the images with the worst segmentation accuracy in all the three test data sets resemble the manual annotations of the second human observer more than the first human observer. Since vessel segmentation performance is dependent on the manual annotations that are subjective to the observer, the proposed algorithm performs fairly accurately with respect to both human observers.

Next, the performance and segmentation time of the proposed blood vessel segmentation algorithm in comparison with existing vessel segmentation methods are shown in Table 2.3.

From Table 2.3, we observe that the proposed vessel segmentation algorithm outperforms most of the existing methods on the DRIVE Test data set in terms of segmentation ACC and AUC. However, on the STARE data set, the accuracy of the proposed algorithm is out-performed in terms of ACC and AUC by the existing methods Lam et. al [21] and Fraz et. al [12]. The method Marin et. al. [13] has better AUC and the method Ricci et. al. [29] has better ACC. The method by Lam et. al. [21] uses a perceptive transform model to handle abnormal images specifically and incurs considerably high computational complexity in this process. The method by Fraz et. al. [12] uses complex decision tree-based classifiers for vessel classification, and hence it suffers from high computational complexity and test data dependence. The proposed approach of segmenting the major vessel pixels and fine vessel pixels separately incurs lower computational complexity and consistent segmentation ACC. The method by Marin [13] trains neural network classifiers on a few hand-picked image pixels from the DRIVE Train data set and classifies major vessel pixels and fine vessel pixels using the same

7-dimensional feature set. Hence, the optimal threshold for vessel-pixel classification varies significantly with varying FOVs of the test data set, i.e., threshold for DRIVE Test data set and STARE data sets are 0.63 and 0.91, respectively. Since the proposed method applies classification for only for the fine vessel pixels, hence the optimal classification thresholds are observed to be less variable, thereby increasing the robustness of the proposed method with respect to the existing methods. The method by Ricci et. al. [29], trains support vector machine (SVM) classifiers using 20,000 manually segmented randomly chosen pixels from the DRIVE and STARE data set separately. This method requires SVM classifiers to be retrained for any new test data set and it suffers from computational complexity due to the SVM classifier.

The proposed method incurs low computational complexity since the major vessels are extracted by an unsupervised approach followed by supervised identification of fine blood vessel segments, thereby significantly reducing in the number of pixels under classification. However, segmentation time is dependent not only on algorithmic complexity but also on the implementation software and platform. The unsupervised methods by Budai et. al. (2010) [24] and Budai et. al. (2013) [25] achieve vessel segmentation in the least time since these methods are implemented using C++ while all the other methods in Table 2.3 are implemented using MATLAB.

2.4.2 Abnormal Image Analysis

High vessel segmentation performance on abnormal retinal images implies robustness of the method. To assess the robustness of the proposed method two images from the STARE Abnormal data set, one with red lesions, and another with bright lesions are subjected to vessel segmentation using the unsupervised baseline methods (H, T), and by the proposed method. The optimal segmentations are shown in Fig. 2.7. These two abnormal images have been specifically analyzed by some the methods in [19] [20] [21].

The performance of the proposed approach compared to existing segmentation methods on the two abnormal retinal images in Fig. 2.7 are shown in Fig. 2.8. Using the proposed method on such retinal images with abnormalities, about 50% of the vessel pixels are subjected to classification in the vessel sub-image. Small red lesions and bright lesion edges have similar gradient-based features as the fine vessels, and hence

such false edge pixels get classified as vessel pixels, thereby leading to a lower SPEC when compared to normal retinal images. In Fig. 2.8 (a), we observe that for the image with red lesions, only the methods by Soares et. al. [28] and Lam et. al. [21] have better performance than the proposed method. Since the method by Soares et. al. [28] performs vessel classification by leave-one-out strategy on the images from the STARE data set, it achieves better segmentation performance than the proposed method. The method by Lam et. al. [21] is trained specifically for such abnormal images and hence it has superior segmentation performance. The proposed method outperforms the methods by Marin et. al. [13], Lam and Yan [20], Hoover et. al. [15], Jiang et. al. [22] and Vermeer et. al. [19] that include most of the red lesion regions as vessels.

In Fig. 2.8 (b), for the image with bright lesions, we observe that the method Lam et. al. [21] has better segmentation performance than the proposed method. The methods by Soares et. al. [28] and Marin et. al. [13] have comparable performance with slightly less false positives than the proposed approach, but with lower SEN due to the broken vessel-like structures detected. Thus, we observe that the proposed approach has higher segmentation accuracy than most existing methods on normal and abnormal retinas and it is more robust for vessel segmentation when compared to baseline unsupervised models.

2.4.3 Cross-Training by inter-changing the Training/Test data

The dependence of the proposed segmentation method on the training data set is demonstrated by interchanging the training and test data sets and analyzing the change in mean and standard deviation of the vessel segmentation ACC in Table 2.4. As the training data is changed, the classifier threshold is determined by leave-one out cross validation on the training set of images. By training on the DRIVE Test, STARE, and CHASE_DB1 data sets, the threshold probabilities were found to be 0.94,0.9 and 0.8, respectively.

From the second column in Table 2.4, we observe that by training the GMM classifier on pixels from the STARE and CHASE_DB1 data set and testing the classifier on the DRIVE Test set of images, the mean ACC varies by 0.01% (0.9493 to 0.9494). The third column demonstrates that by varying the training data set from DRIVE Test to CHASE_DB1 and testing the classifier on STARE set of images, the ACC varies by

0.25% (0.951 to 0.9535). The fourth column demonstrates that by varying the training data set from DRIVE Test to STARE and testing the classifier on the CHASE_DB1 image set, the ACC varies by 0.34% (0.9486 to 0.952). Thus, the variation in ACC for each Test data set by varying the training data set is considerably small, which leads to low dependence on training data and high robustness of the proposed algorithm. Next, the performance of cross-training of the proposed algorithm is compared with existing methods in Table 2.5.

From Table 2.5, we observe that by cross-training, the absolute ACC variations between DRIVE Test and STARE data sets incurred by the Marin et. al. [13] method, Ricci et. al. [29] method, Fraz et. al. method [12] and the proposed method are 0.78%, 1.86%, 0.37% and 0.16%, respectively. Also, the absolute ACC variation between the STARE and CHASE_DB1 data set by cross-training is observed to be 0.78% for the Fraz. et. al. [12] method, and 0.24% for the proposed algorithm. Thus, the segmentation performance of the proposed method has lower dependence on the training data set when compared to the existing methods since the segmentation ACC remains significantly consistent when the training data set is changed.

2.4.4 Peripapillary vessel analysis

In retinal fundus images, the blood vessels in and around the optic disc are referred to as the peripapillary blood vessels. Many retinal abnormalities such as proliferative DR (PDR), glaucoma, central retinal vein occlusion, cilio retinal artery occlusion can lead to changes in the blood vessel structure mainly in the peripapillary region. For instance, neovascularization at the disc (NVD) caused due to PDR is evident if new blood vessels are visible within 1-optic disc diameter (1-DD) centered at the papilla [34]. For this purpose, the images from the DRIVE, STARE and CHASE_DB1 data set were manually annotated for the optic disc boundary and optic nerve head in each image, and then, a mask was created centered at the optic nerve head with 1-DD radius to extract the peripapillary region. The first 19 images from the STARE vessel segmentation data set contain the peripapillary region and hence peripapillary vessel detection was performed on these 19 images only.

The segmented vessel images using the Marin et. al. method [13][1] , Soares et.

[1] Available at http://www.uhu.es/retinopathy/eng/bd.php

al. method [28] [2] , Jiang et. al. method [22] and Staal et. al. method [27] [3] are downloaded from the respective websites for comparison. Next, the performance of the proposed vessel segmentation method in comparison with existing methods and the more detailed second human observer annotations for the STARE data set is shown in Fig. 2.9. The segmented vessel images are compared to the segmentation results produced by the Marin et. al. method [13], Soares et. al. method [28] and Hoover et. al. method [15] [4] . We observe that the proposed method has a better accuracy for segmenting the peripapillary vessels for both these blood vessels.

Finally, we compute the performance of peripapillary vessel segmentation for the three data sets with respect to the two human observers in Table 2.6. We observe that for the DRIVE Test data set, the proposed segmentation algorithm results in 0.1% (with respected to Marin et. al. [13]) to 6.1% (with respected to Jiang et. al. [22]) improvement in vessel accuracy when compared to existing methods using the first human observer annotations, and 0.8% to 7.0% improvement against the same methods using the second human observer.

For the STARE data set, the proposed vessel segmentation achieves 3.3% (with respected to Marin et. al. [13]) to 8.2% (with respected to Hoover et. al. [15]) improvement in vessel accuracy when compared to existing methods using the first human observer annotations, and 4.5% (with respected to Soares et. al. [28]) to 5.4% (with respected to Hoover et. al. [15]) improvement using the second human observer. For the CHASE_DB1 data set, peripapillary vessel segmentation accuracy greater than 83% is achieved with respect to both human observers.

2.5 Discussion and Conclusions

The most important feature of the proposed segmentation algorithm is separate segmentation of major vessel and fine vessel regions. Major vessels regions are identified as the intersecting regions between thresholded versions of two pre-processed images, i.e., the high-pass filtered image and tophat transformed image. The pixel threshold 'p'

[2] Available at http://sourceforge.net/apps/mediawiki/retinal/index.php ?title=Segmentation_results

[3] Available at http://www.isi.uu.nl/Research/Databases/DRIVE/browser.php

[4] Available at http://www.parl.clemson.edu/ ahoover/stare/probing/index.html

can be varied across images to increase or decrease the number of pixels identified as major vessels. If the number of major vessel pixels is decreased by varying the pixel thresholds for the two pre-processed images, then the number of pixels subjected to classification in the vessel sub-image increase. This process will aid automated segmentation of very fine vessel branches that are necessary for detecting retinal abnormalities such as intraretinal microvascular abnormalities (IRMA) or vessel beading.

In the second stage of the proposed algorithm, the major vessels are removed from the thresholded pre-processed images to generate a vessel sub-image. A GMM classifier with 2-Gaussians is then used to identify the fine vessel pixels in this vessel sub-image. Since the number of vessel pixels subjected to classification is lowered by major vessel region removal, hence the dependence of the classifier on training data is lower when compared to existing supervised methods that classify the complete vasculature [13] [29] [12]. Future work will be directed towards analyzing the variations in computational complexity and segmentation performance for the proposed method using other classifiers and GMM models with a mixture of more than 2-Gaussians [28].

The proposed vessel segmentation method not only achieves consistent vessel segmentation ACC of 95%, but it also ensures extraction of fine vessel branches. In Table 2.3 we observe that the existing methods in Budai et. al. (2013) [25], Marin et. al. [13] and Staal et. al. [27] have comparable segmentation ACC, but lower SEN and comparable or higher SPEC when compared to the proposed approach. Thus, for analysis of abnormalities in the fine blood vessels, the proposed approach is preferable over the other methods with lower SEN. However, the method by Ricci et. al. [29] demonstrates higher SEN but lower SPEC than the proposed approach. The proposed approach is preferable over this method in retinal images with significantly large number of red lesions in the vicinity of the vasculature, since it introduces lesser false vessel pixels in the final segmented blood vessels.

In this chapter, we have identified a set of 8 features that discriminate non-vessel pixels from fine vessel pixels in the vessel sub-image. These 8 features are ranked based on the mRMR criterion since the neighborhood-based features were mutually dependent and since the number of vessel and non-vessel pixels from the vessel sub-images obtained from the DRIVE Train data set were almost equally weighted.

The proposed segmentation method outperforms most existing methods for the 10

abnormal retinal images with pathology in the STARE Abnormal data set as shown in Table 2.7. The method by Marin et. al. [13], Lam and Yan [20] and Lam et. al. [21] have higher segmentation ACC or AUC than the proposed method, but they incur higher computational complexity as compared to the proposed approach.

The next most significant feature of the proposed method is the high accuracy of peripapillary blood vessel extraction that makes the proposed segmentation algorithm very useful for computer-aided screening for patients with PDR, glaucoma and retinal vein occlusions.

The low computational complexity and low dependence on training data make the proposed algorithm ideal for integration with retinal screening systems. Future work will be directed towards combining the proposed algorithm with DR screening systems such as [3] to detect neovascularization in the peripapillary region, and to reduce false positives while detecting red lesions. Also, the proposed method will be further fine-tuned for automated extraction of vessels in wide-field fundus images with 200^o FOV.

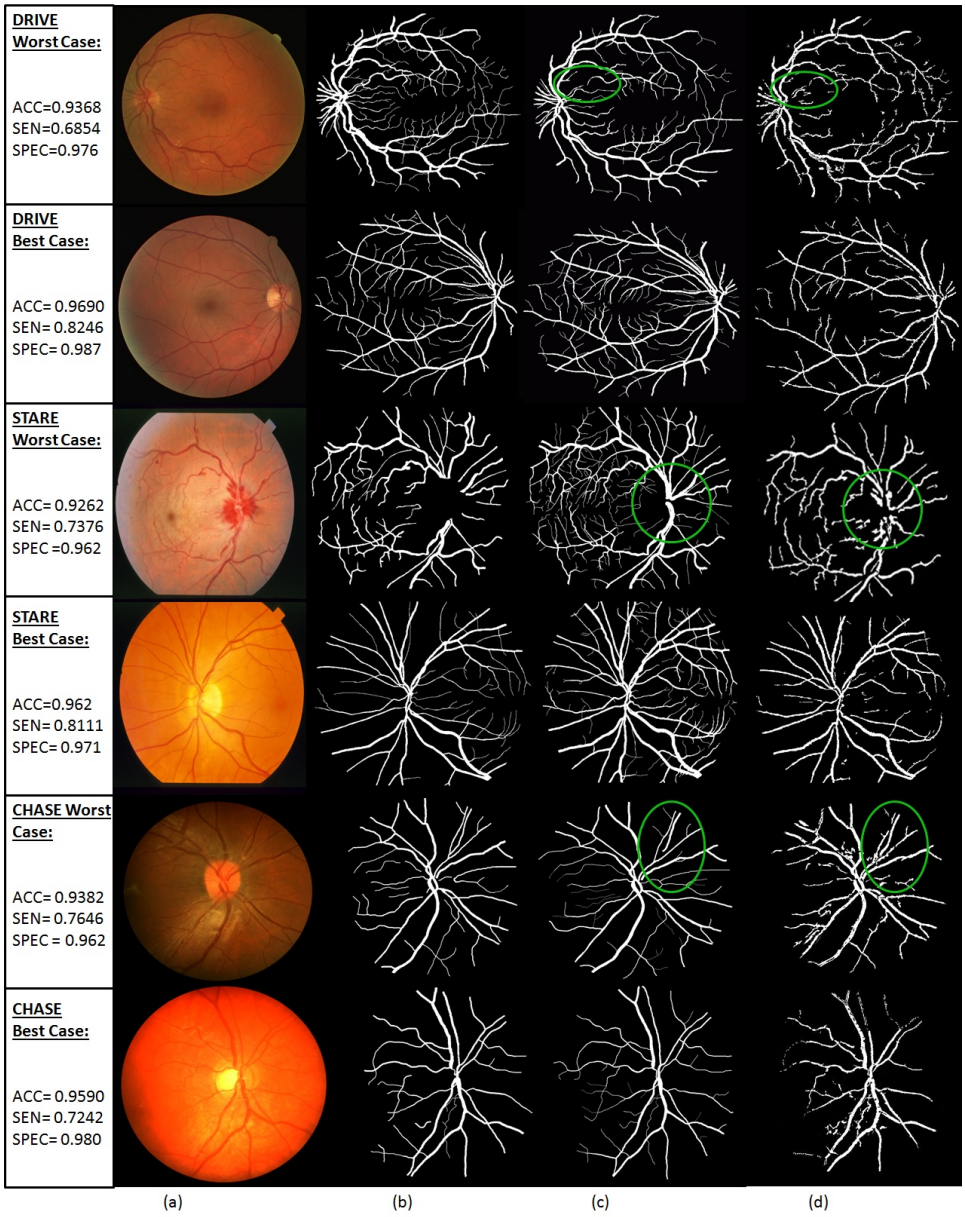

Figure 2.6: Best and worst vessel segmentation examples from the DRIVE Test, STARE, and CHASE_DB1 data sets. (a) Original image. (b) first human observer annotation. (c) second human observer annotation. (d) Segmented vessels using the proposed algorithm. In the images with worst ACC, the segmented vessels within the region enclosed by the green circle resemble the manual annotations of the second human observer more than the first human observer.

Table 2.3: Comparative Performance of Proposed Model with existing works on the DRIVE and STARE data sets.

Test Data:	DRIVE	Test			
Method	ACC	SPEC	SEN	AUC	Time
Jiang et. al. [22]	0.891	0.90	0.83	0.932	8-36 s
Niemeijer et. al. [26]	0.942	0.969	0.689	0.93	-
Staal et. al. [27]	0.944	0.977	0.719	0.952	15 mins
Mendonca et. al. [17]	0.945	0.976	0.734	-	2.5 mins
Soares et. al. [28]	0.946	0.978	0.733	0.961	∼3 mins
Ricci et. al. [29]	0.959	0.972	0.775	0.963	-
Al-Diri et. al.[23]	-	0.955	0.728	-	11 mins
Lam et. al. [21]	0.947	-	-	0.961	13 mins
Budai et. al.(2010)[24]	0.949	0.968	0.759	-	11 s
Budai et. al. (2013) [25]	0.9572	0.987	0.644	-	1.04s
Marin et. al. [13]	0.945	0.98	0.706	0.958	∼90 s
Miri et.al. [18]	0.943	0.976	0.715	-	∼50 s
Fraz et. al. [12]	0.948	0.981	0.74	0.974	∼100 s
Proposed	**0.952**	**0.983**	**0.725**	**0.962**	**3.11 s**
Test Data:	STARE				
Hoover et. al. [15]	0.927	0.81	0.65	0.75	5 mins
Jiang et. al. [22]	0.901	0.90	0.857	0.929	8-36 s
Staal et. al. [27]	0.952	0.981	0.697	0.961	15 mins
Mendonca et. al. [17]	0.944	0.973	0.699	-	3 mins
Soares et. al. [28]	0.948	0.975	0.72	0.967	∼3 mins
Ricci et. al. [29]	0.965	0.939	0.903	0.968	-
Lam and Yan [20]	0.9474	-	-	0.9392	8 mins
Al-Diri et. al.[23]	-	0.968	0.752	-	-
Lam et. al. [21]	0.957	-	-	0.974	13 mins
Budai et. al.(2010)[24]	0.938	0.975	0.651	-	16 s
Budai et. al. (2013) [25]	0.9386	0.982	0.58	-	1.31s
Marin et. al. [13]	0.952	0.982	0.694	0.977	∼90 s
Fraz et. al. [12]	0.953	0.976	0.755	0.976	∼100 s
Proposed	**0.951**	**0.973**	**0.772**	**0.969**	**6.7 s**

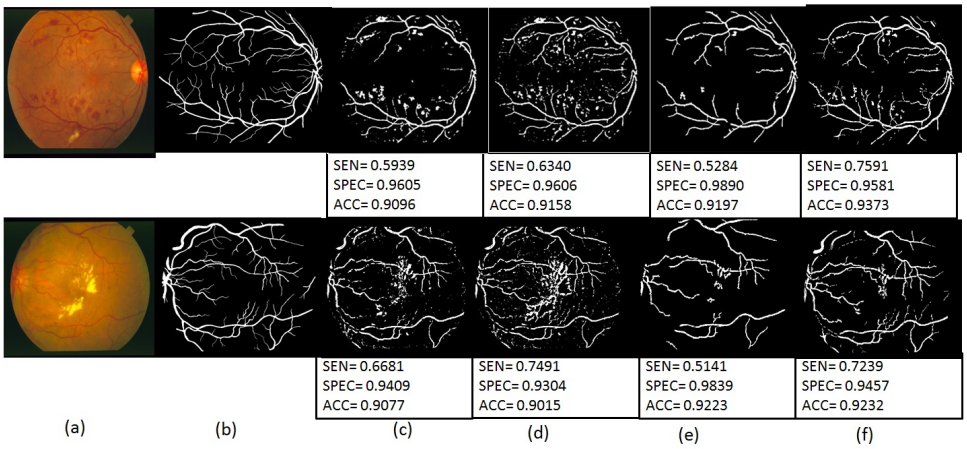

Figure 2.7: Vessel segmentation on abnormal images. First row depicts vessel segmentation on an image with red lesions while the second row depicts segmentation on an image with bright lesions. (a) Image (b) Manually marked vessels. (c) Thresholded tophat transformed image ($T > 0.44$). (d) Thresholded high-pass filtered image ($H > 0.36$). (e) Major vessels detected (P). (f) Final segmented vasculature using proposed method.

Table 2.4: Vessel Classification ACC by Cross-Training.

Train Data	Test Data		
	DRIVE Test	STARE	CHASE_DB1
DRIVE Test	NA	0.951 (0.013)	0.952 (0.005)
STARE	0.9494 (0.0072)	NA	0.9486 (0.011)
CHASE_DB1	0.9493 (0.0071)	0.9535 (0.016)	NA

Table 2.5: Segmentation Performance with Cross Training in terms of mean ACC given for Test Data (Training data).

Method	DRIVE Test (STARE)	STARE (DRIVE Test)	CHASE_DB1 (STARE)
Marin et al. [13]	0.9448	0.9526	-
Ricci et al. [29]	0.9266	0.9452	-
Fraz et. al. [12]	0.9456	0.9493	0.9415
Proposed	**0.9494**	**0.951**	**0.9486**

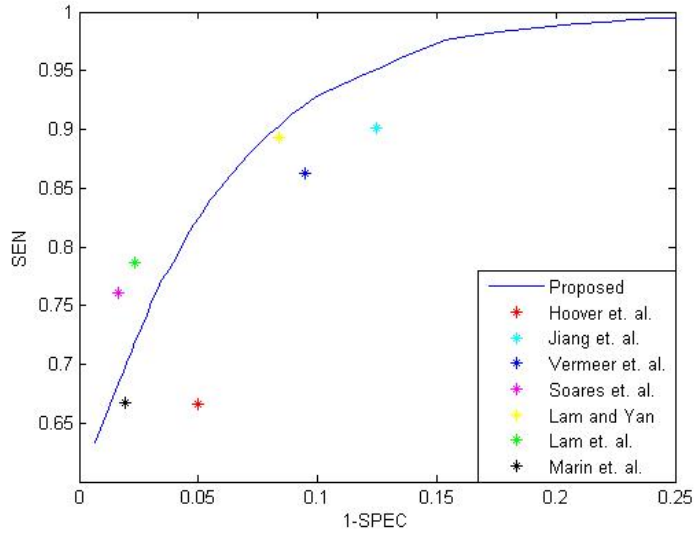

(a)

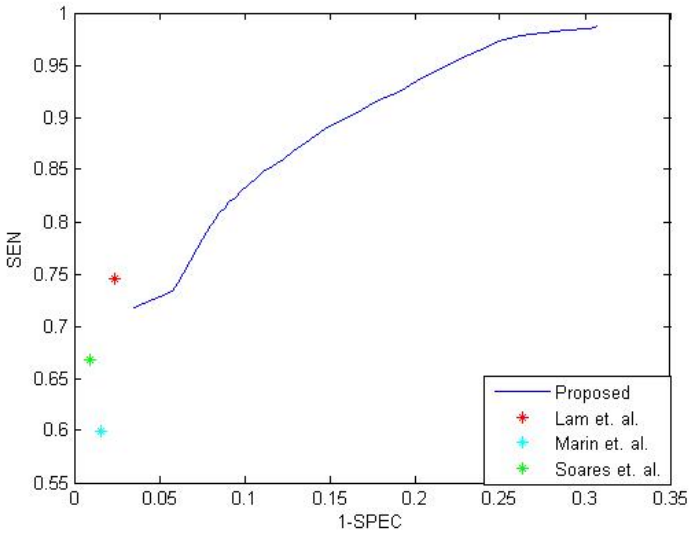

(b)

Figure 2.8: Comparative performance of existing methods with proposed method on the abnormal retinal images. (a) ROC curve for the first abnormal image with red lesions in Fig. 2.7. (b) ROC curve for the second abnormal image with bright lesions in Fig. 2.7.

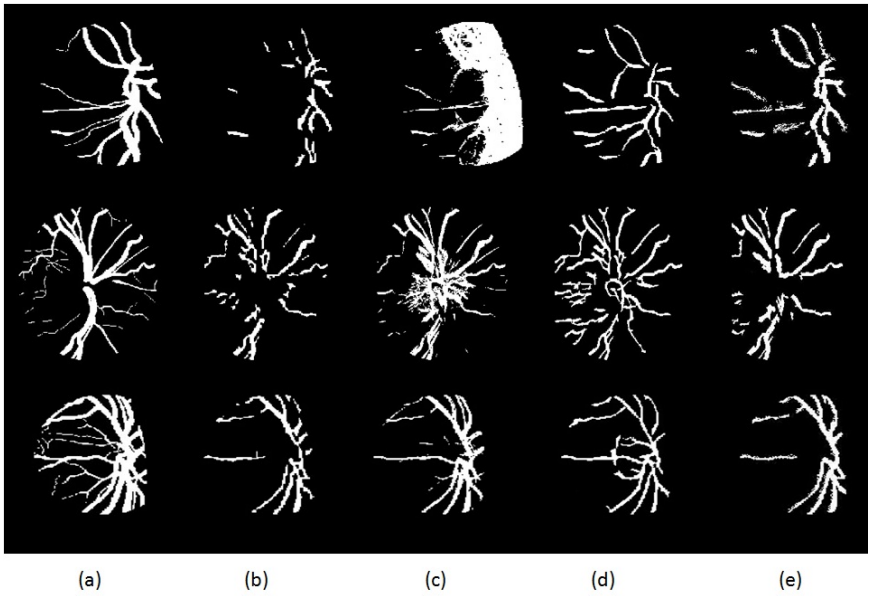

Figure 2.9: Peripapillary vessels segmented for the STARE set of images. (a) Second Human Observer. (b) Marin et. al. method. (c) Soares et. al. method, (d) Hoover et. al. method. (e) Proposed Method.

Table 2.6: Peripapillary Vessel Analysis. ACC and the standard deviation is given in () with respect to the two human observers.

Method	First Observer	Second Observer
	DRIVE Test	
Marin et. al. [13]	0.9141 (0.0165)	0.9189 (0.0177)
Soares et. al. [28]	0.9116 (0.0178)	0.9167 (0.0141)
Jiang et. al. [22]	0.8625 (0.0261)	0.8656 (0.0243)
Staal et. al. [27]	0.9103 (0.0202)	0.9146 (0.0176)
Proposed	**0.9150 (0.0233)**	**0.9261 (0.0201)**
	STARE	
Marin et. al. [13]	0.8053 (0.0372)	0.7189 (0.0584)
Soares et. al. [28]	0.8038 (0.0480)	0.7239 (0.0536)
Hoover et. al. [15]	0.7685 (0.0341)	0.7179 (0.0387)
Proposed	**0.8322 (0.0291)**	**0.7571 (0.0588)**
	CHASE_DB1	
Proposed	**0.8393 (0.0205)**	**0.8478 (0.0146)**

Table 2.7: Segmentation Performance on the STARE Abnormal data set.

Method	ACC	AUC	Time
Hoover et. al. [15]	0.9211	0.7590	5 mins
Jiang et. al. [22]	0.9352	0.9343	8-36 s
Mendonca et. al. [17]	0.9426	-	3 mins
Soares et. al. [28]	0.9425	0.9571	3 mins
Vermeer et. al. [19]	0.9287	0.9187	-
Marin et. al. [13]	0.9510	-	90 s
Lam and Yan [20]	0.9474	0.9392	8 mins
Lam et. al. [21]	0.9556	0.9707	13 mins
Proposed	**0.9453**	**0.9596**	**8.36 s**

Chapter 3

Automated Vessel Segmentation: An Iterative Algorithm

3.1 Introduction

Retinal blood vessel (vasculature) segmentation using fundus photographs has played a vital role in assessing the severity of retinal pathologies that can lead to acquired blindness such as retinopathy of prematurity [35], glaucoma, vein occlusions and diabetic retinopathy (DR) [36]. According to research statistics in the year 2011, retinal pathologies such as DR affect over 4.2 million Americans each year, while glaucoma affects about 2.3 million Americans annually [5]. In such a scenario, automated blood vessel segmentation algorithms can be very useful in screening patients that are affected by such retinal complications and require follow-up [4]. Also, automated blood vessel segmentation systems can be useful in determining variations in the blood vessels based on the vessel branching patterns, vessel width, tortuosity and vessel density as the pathology progresses in patients [6]. Such evaluations will help to enhance the resourcefulness of the present-day retinal therapeutics and guide research towards analyzing patients for hypertension [7], variability in retinal vessel diameters due to a history of cold hands and feet [8], and flicker responses [9].

Some existing automated detection systems for non-proliferative DR detection, such as [10] [3] [37], require masking of the blood vessels to ensure that the blood vessels are not mistaken for red lesions that are caused by DR. Additionally, proliferative DR

detection systems [34] require analysis of the vessel parameters for detecting neovascularization, vessel beading and intra retinal micro-vascular abnormalities (IRMA). A fast and accurate segmentation algorithm for detecting the blood vessels is necessary for such automated real-time detection and screening systems. In this chapter, we propose an unsupervised vasculature segmentation algorithm that iteratively estimates the blood vessels with significantly high accuracy in normal images as well as images with abnormalities such as bright lesions like exudates or red lesions like hemorrhages or micro-aneurysms. After an initial training with any arbitrary data set, this novel approach does not require any retraining on new datasets and is robust to variations in the fundus image fields of view (FOV), uneven illumination, pigmentation and pathology. Additionally, the proposed algorithm is computationally the fastest and most consistent in segmentation performance across the three data sets of DRIVE [27], STARE [15] and CHASE_DB1 [30].

Key contributions of the chapter include a *novel iterative* blood vessel segmentation algorithm, where vasculature estimates are identified by adding new pixels iteratively using adaptive global thresholding, and a novel *stopping criterion* to terminate the iterative vessel addition process thereby reducing the number of false edge pixels in the segmented image. The proposed vessel segmentation algorithm is robust to image variability, achieves high segmentation accuracy in normal as well as abnormal retinal images. For the images in STARE data set, the proposed approach achieves an average accuracy of 95.6%. We identify vessel segmentation accuracy in the peripapillary region as another important metric; this metric is well suited for images with abnormalities such as proliferative DR, glaucoma and retinal occlusions. The peripapillary blood vessels contain vessels within 1-optic disc diameter centered at the papilla [34]. It is shown that the proposed approach provides the highest vessel segmentation accuracy in the peripapillary region among all known algorithms.

The organization of this chapter is as follows. In Section 3.2, the prior automated vessel segmentation algorithms in the literature are reviewed. The proposed method and materials are described in Section 3.3. In section 3.4, the experimental results are presented and compared with existing methods, for normal and abnormal retinal images, and for peripapillary vessel extraction. Finally, in Section 3.5, discussion and significant conclusions are presented.

3.2 Prior Work

All existing algorithms for automated segmentation of blood vessels using fundus images can be broadly categorized as supervised and unsupervised methods. The methods belonging to these categories are explored below.

The supervised vessel segmentation algorithms classify pixels as vessel and non-vessel. One such method in [26] trains the k-Nearest Neighbor classifier with 31-features extracted using Gaussians and its derivatives of the fundus image. This method was further improved in [27] by applying ridge-based vessel detection, where each pixel is assigned to its nearest ridge element, thus partitioning the image. For classification, 27 features corresponding to each pixel are computed, followed by kNN classification. These methods are computationally intensive due to the large size of the classification feature sets. Other methods with smaller classification features include a Gaussian Mixture Model (GMM) classifier where 6-features are extracted using Gabor-wavelets for vessel classification [28]. This method is also computationally intensive since it requires several hours for training GMM models with a mixture of 20 Gaussians. Another method in [29] uses line operators and a support vector machine (SVM) classifier with 3-features per pixel for classification. The method in [13] applies neural network classifiers using 7-features extracted by neighborhood parameters and moment invariants-based method. Also, the method in [12] applies boosting and bagging strategies with 200 decision trees and 9-features for vessel classification extracted by Gabor filters. This method suffers from high computational complexity as well due to the boosting strategy. All these supervised vessel classification-based methods are dependent on the training data and sensitive to false edges as well.

Among the existing unsupervised methods, algorithms that apply matched filtering, vessel tracking, morphological transformations and model-based algorithms are predominant. In the matched filtering-based method in [15], a 2-D linear structuring element is used to extract Gaussian intensity profiles of the blood vessels. The structuring element is rotated 8-12 times to fit the vessels in different configurations to extract the vessel boundaries. This method has a high time complexity since a stopping criterion needs to be evaluated for each end pixel. A morphology-based method in [17] combines morphological transformations with curvature information and matched-filtering for detecting

the central line of the blood vessels. This method is sensitive to false edges introduced by bright region edges such as optic disc and exudates. Another morphology based method in [18] uses multiple structuring elements to extract vessel ridges followed by connected component analysis. In another model-based method [19], blood vessel structures are extracted by convolving with a Laplacian kernel followed by thresholding and connecting broken line components. An improvement of this methodology was presented in [20], where the blood vessels are extracted by the Laplacian operator and noisy objects are pruned according to center lines. This method focuses on vessel extraction from images with bright abnormalities, but it does not perform very effectively on retinal images with red lesions (such as hemorrhages or microaneurysms). The method in [21] presents perceptive transformation approaches to segment vessels in retinal images with bright and red lesions. A model-based method in [22] applies locally adaptive thresholding and incorporates vessel information into the verification process. Although this method is more generalizable than matched-filter based methods, it has a lower overall vessel segmentation accuracy. Another model-based vessel segmentation approach proposed in [23] uses active contour models. Additionally, a multi-scale vessel segmentation method proposed in [24] uses neighborhood analysis at each level of a 3-level Gaussian pyramid. All these unsupervised methods are computationally complex and hence they are not viable for real-time portable DR screening systems such as [3]. Most of the unsupervised approaches such as [28], [20] perform well on healthy retinal images but have low segmentation accuracy in images with pathology. Also, methods like [17] [21] have higher segmentation accuracy on pathological images than most other methods. Thus, there is a need for a general method that produces high segmentation accuracy for normal as well as pathological fundus images.

In this chapter, we propose an *iterative* vessel segmentation algorithm that segments the *major vessels* first, followed by addition of finer vessel branches by adaptive thresholding in iterative steps. A novel stopping criterion is designed to estimate the best segmented vessel estimate such that the algorithm stops before false positive pixels, due to uneven illumination or pigmentation, or edges of bright lesions, optic disc or red lesions, get added to the segmented vessel estimate. This iterative approach has high segmentation accuracy for vasculature in normal and abnormal retinal images. Also, the proposed method has lower computational complexity than all existing supervised

and unsupervised approaches.

3.3 Method and Materials

The principal idea behind iterative vessel segmentation is that in a vessel enhanced image, the bright and large vessels overshadow the thinner fine vessel branches. In such a situation, global thresholding would extract only the large prominent vessels while the finer vessel branches would remain unsegmented. Thus, to include these fine vessels into the segmented vasculature estimate, *iterative adaptive* global thresholding is proposed.

For every color fundus photograph, a vessel enhanced image is obtained by morphological tophat reconstruction of the negative green plane image. The brightest pixels from this vessel enhanced image are extracted as the major portions of the vasculature, or *major vessels*. A residual image is then generated by masking these major vessels from the vessel enhanced image followed by contrast adjustment and adaptive thresholding in an iterative manner to uncover new vessel pixels and add them to the existing vessel estimate. This method of iterative vessel addition and a novel stopping criterion for estimating the best segmented vasculature is presented in this section. The segmentation performance of the proposed algorithm is evaluated using three publicly available data sets with different resolutions and FOVs. The proposed algorithm has been implemented in MATLAB environment on a Laptop with Intel Core i3 processor, 2.6GHz and 2GB RAM.

3.3.1 Data

The following data sets have been manually annotated for the blood vessel regions for analyzing the performance of blood vessel segmentation algorithms.

- STARE [15] data set contains 20 images with 35^o FOV of size [605x700] pixels that are manually annotated by two independent human observers. Here, 10 images represent patients with retinal abnormalities (STARE Abnormal). The other 10 images represent normal retina (STARE Normal).

- DRIVE [27] data set contains 40 images with 45^o FOV of size [584x565] pixels. This data set is separated by its authors into a training set (DRIVE Train) and

a test set (DRIVE Test) with 20 images in each set. The DRIVE Train set of images are annotated by one human observer while the DRIVE Test data set is annotated by two independent human observers.

- CHASE_DB1 [30] data set contains 28 images with 30^o FOV of size [960x999] pixels corresponding to two images per patient (one image per eye) for 14 children. Each image is annotated by two independent human observers [12].

3.3.2 Proposed Method

As a pre-processing stage, the green plane of each fundus image is scaled in [0,1] (I). A fundus mask (g) is utilized to remove the dark background region from the photographs to focus attention on the retinal region only. The fundus masks for DRIVE, STARE and CHASE_DB1 data sets are generated as centered elliptical regions with diameters of [521x520], [550x650] and [860x869] pixels, respectively.

In the scaled green plane image (I), the red regions corresponding to the blood vessel segments appear as dark pixels with intensities close to 0. To focus attention on the blood vessel regions, image I is inverted to make the red regions appear the brightest, followed by superposition of the mask g, resulting in image I_v. I_v is then subjected to contrast enhancement followed by morphological tophat transformation. 12 linear structuring elements each of length 21 pixels and 1 pixel width and angles incremented by 15^o from 0 through 180^o are used to generate tophat reconstructions from I_v [17] [12]. The length of 21 pixels for the linear structuring element is chosen to approximately fit the diameter of the biggest vessels in the images [12]. For each pixel location, the reconstructed pixel with the highest intensity is selected, thereby resulting in tophat reconstructed vessel enhanced image T.

The *major vessels* (V_0) are extracted by thresholding image T for pixels greater than 0.5, and retaining the regions with area greater than 200 pixels. Thus, V_0 is the segmented vessel estimate (V_t) at iteration $t = 0$. Next, the following steps are iteratively performed:

For each iteration t, the pixels from the existing vessel estimate V_t are removed from image T and the remaining image is contrast enhanced resulting in residual image R_t. This image R_t is thresholded at pixel value $\phi_1(t)$ to extract a binary image V_{R_t}

containing new vessel regions that have an area of at least 10 pixels. Here, the pixel threshold value $\phi_1(t)$ varies with 't', the iteration number. However, it is desirable for the segmented vessel to have a continuous structure and hence it is imperative to fill any gaps or holes between the existing vessel estimate V_t and the newly identified vessel pixels in V_{R_t}. Thus, the pixels in V_t and V_{R_t} are added to vessel enhanced image T, followed by rescaling the pixels in [0,255], resulting in base image B_t. This image B_t is then region-grown with a threshold pixel value ($\phi_2(t)$) that is a function of the iteration number. The image obtained at the end of the regiongrow operation [38] is the new iterative vessel estimate (V_{t+1}).

The iterative addition of the newly identified vessel regions to the existing vessel estimate is continued till a stopping criterion is met. The notations and their definitions used in this iterative algorithm are defined in Table 3.1.

For an image from the DRIVE data set, the iterative vessel estimates are shown in Fig. 3.1 for 10 iterations, i.e., $t = [1, 2...10]$. The proposed iterative segmentation algorithm is given in Algorithm 1. For the example shown in Fig. 3.1, the best segmented vasculature is estimated at iteration $t = 4$.

For post-processing, the regions in the best vessel estimate with area less than 20 pixels are discarded, and the remaining vessel regions are median filtered with a [3x3] filter.

It is important to note that Algorithm 1 relies on two threshold parameters that impact the accuracy of the final vessel estimate. These two threshold parameters $\phi_1(t)$ and $\phi_2(t)$ affect the quality of new vessel pixels that are added to the existing vessel estimate. The other important feature in the iterative vessel segmentation algorithm is the estimation of the iteration number (t_f) at which the best vessel estimate with the highest segmentation accuracy occurs. To determine t_f, a stopping criterion is introduced. The methods for estimating the adaptive thresholds $\phi_1(t)$ and $\phi_2(t)$, and stopping criterion are given below.

Thresholds for vessel addition

In each iteration step 't', new vessels are identified from the iterative residual image in V_{R_t} using pixel threshold $\phi_1(t)$. Here, we initialize $\phi_1(t) = 1-(0.05*t)$. As the algorithm progresses to combine the new vessel pixels (V_{R_t}) to the existing vessel estimate (V_t), a

Algorithm 1 Iterative Vessel Segmentation (I, g)

Input: $I \in [0,1],\ g \in [0,1]$
Output: V_f
Pre-Processing:
$I_v \leftarrow$ contrast_adjust$((1-I) \circ g)$
$T \leftarrow$ tophat_reconstruction(I_v)
$V_0 \leftarrow [(T > 0.5)$, and area $> 200]$
Iterations:
$t = 0$, stop$\leftarrow$ 'No', stop $\in$ ['Yes','No'],
while [stop$\leftarrow$ 'No'] **do**
$\forall (i,j), R_t(i,j) = \{[T(i,j) - V_t(i,j)] | R_t(i,j) \geq 0\}$.
$V_{R_t} \leftarrow [R_t > \phi_1(t)$, and area $> 10]$
$B_t \leftarrow$ scale $(\{V_{R_t} \cup V_t\} + T \in [0, 255])$
$V_{t+1} \leftarrow$ regiongrow(B_t, seed=255, threshold=$\phi_2(t)$)
$t \leftarrow t + 1$
stop $\leftarrow$ Stopping_criterion (V_t, V_{t-1})
end while
$t_f \leftarrow t$
$V_f \leftarrow V_{t_f}$
return V_f

regiongrow operation [38] is performed by scaling the image $(V_{R_t} \cup V_t) + T$ in [0,255], using a seed pixel value of 255, and a threshold pixel value $\phi_2(t)$. The threshold function $\phi_2(t)$ that would result in significantly high accuracy for vessel segmentation is obtained by one-time training using the 20 images from the DRIVE Train data set. We consider $\phi_2(t)$ given by:

$$\phi_2(t) = 205 + \alpha * (t-1)^k,\ \alpha \in [1, 2...6],\ k \in [0, 0.2, ...3] \tag{3.1}$$

Each of the 20 images were subjected to vessel segmentation for all the 6x16 combinations of 'α' and 'k' values in (3.1) and $[t = 1, 2..10]$ iterations. For every image ($l = [1...20]$), and for each combination of $[\alpha, k]$, the highest segmentation accuracy (ACC^l) was achieved at iteration number t_l. The mean ACC^l and the corresponding mean t_l versus $[\alpha, k]$ are shown in Fig. 3.2 (a) and Fig. 3.2 (b), respectively. Since, a low mean iteration number implies higher segmentation speed for the algorithm, the goal was to select a threshold function that generates the highest mean vessel segmentation accuracy in less iterations. We observe that, the highest mean ACC_l occurs for

$\alpha = 1, k = 1.8$, with the mean iteration number $t_l = 4$. Thus, the threshold function $\phi_2(t)$ for Algorithm 1 was estimated as $\phi_2(t) = 205 + (t-1)^{1.8}$.

Stopping criterion design

In Fig. 3.1, we observe that the best vessel estimate occurs at some iteration between $t = 0$ to $t = 10$. Also, Algorithm 1 requires a stopping criterion to stop the iterative vessel addition process at iteration number t_f where a segmentation vasculature with highest accuracy exists. This stopping criterion can be determined by analyzing the quality of segmented vessel estimates in every iteration.

The initial vessel segment V_0 contains the major portions of the blood vessels and hence it is free from false edge pixels. In each iteration, new pixels are added to the existing blood vessels. While actual vessel pixels are added in each iteration, pixels corresponding to false edges also get introduced into the segmented vessel structure. Using the manually marked vessels V and the iterative vessel estimate V_t in each iteration t, the criteria for any pixel (i, j) to be a true positive (tp_t), true negative (tn_t), false positive (fp_t) and false negative (fn_t) are defined in (3.2)-(3.5). The total number of pixels that are true positives (TP_t), true negatives (TN_t), false positives (FP_t) and false negatives (FN_t) in each image are then computed using (3.6)-(3.9).

For the binary image V_t, in iteration t we define: (3.2)

$$\forall(i,j), i \in [1,2...n_1], j \in [1,2....n_2],$$

$$tp_t(i,j) = 1, \text{ if, } [V(i,j) = 1, V_t(i,j) = 1].$$

$$tn_t(i,j) = 1, \text{ if, } [V(i,j) = 0, V_t(i,j) = 0]. \quad (3.3)$$

$$fp_t(i,j) = 1, \text{ if, } [V(i,j) = 0, V_t(i,j) = 1]. \quad (3.4)$$

$$fn_t(i,j) = 1, \text{ if, } [V(i,j) = 1, V_t(i,j) = 0]. \quad (3.5)$$

$$\sum_{i=1}^{n_1}\sum_{j=1}^{n_2} tp_t(i,j) = TP_t, \sum_{i=1}^{n_1}\sum_{j=1}^{n_2} tn_t(i,j) = TN_t, \quad (3.6)$$

$$\sum_{i=1}^{n_1}\sum_{j=1}^{n_2} fp_t(i,j) = FP_t, \sum_{i=1}^{n_1}\sum_{j=1}^{n_2} fn_t(i,j) = FN_t. \quad (3.7)$$

The sum of all pixels in binary image V_t represents

the total number of TP_t and FP_t pixels in V_t.

$$\Rightarrow \sum_{i=1}^{n_1}\sum_{j=1}^{n_2} V_t(i,j) = TP_t + FP_t. \quad (3.8)$$

$$\text{Also, } n_1 \cdot n_2 = TP_t + TN_t + FP_t + FN_t. \quad (3.9)$$

For a fundus image with $[n_1 \cdot n_2]$ pixels, the metrics identifying the quality of segmented vessel (Q_t), the change in vessel estimate C_t and error in the vessel estimate E_t, are defined in (3.10) - (13). In (12), we observe that E_t has two non-zero components, one due to the FN_t pixels and the other due to FP_t pixels. The vessel segmentation accuracy ACC_t increases as E_t decreases as described by (13). Thus, the iteration t_f corresponding to minimum E_{t_f} will ensure a segmented vessel estimate with highest accuracy.

$$\textbf{Define :} Q_t = \frac{\sum_{i=1}^{n_1}\sum_{j=1}^{n_2}[tp_t(i,j)]}{\sum_{i=1}^{n_1}\sum_{j=1}^{n_2}[fp_t(i,j)]} = \frac{TP_t}{FP_t}. \tag{3.10}$$

$$C_t = \frac{1}{n_1 \cdot n_2}\sum_{i=1}^{n_1}\sum_{j=1}^{n_2}\left\{V_t(i,j) - V_0(i,j)\right\}. \tag{3.11}$$

$$E_t = \frac{1}{n_1 \cdot n_2}\sum_{i=1}^{n_1}\sum_{j=1}^{n_2}|V(i,j) - V_t(i,j)|. \tag{3.12}$$

$$\Rightarrow E_t = \frac{\sum_{i=1}^{n_1}\sum_{j=1}^{n_2}[fp_t(i,j) + fn_t(i,j)]}{TP_t + TN_t + FP_t + FN_t} = 1 - ACC_t. \tag{3.13}$$

Intuitively, C_t can be modeled as an odd-degree polynomial, and E_t can be modeled as an even-degree polynomial. The goal of segmentation is to stop at the iteration with least error to maximize the vessel segmentation accuracy. However, E_t requires knowledge of the manual annotated image and is not known. Therefore, E_t cannot be used as a parameter in the stopping criteria. However, an analysis of the trends in C_t and E_t based on known images demonstrates a correlation between these parameters. This allows us to derive a stopping criterion using C_t. Later in the section we propose to stop the iterations when the first three derivatives of C_t are non-negative. This is illustrated in Fig. 3.3. A key contribution of this chapter is that stopping criterion does not depend on the imaging parameters such as field of view.

To understand the trends of the curves C_t and E_t, we consider a theoretical example shown in Fig. 3.4, where curves C_x and E_x are odd and even functions of the same repeated root, respectively. In Fig. 3.4, E_x is a function of 4th degree repeated root, and hence we analyze the trends of the first three derivatives of E_x and C_x computed using backward difference rule as 'x' varies from [1 to 20] in intervals of 1. We observe that although E_x and C_x are both functions of repeated roots at $x = 10.5$, the first three derivatives of both E_x and C_x become non-negative, i.e., $[E_x^1, E_x^2, E_x^3] \geq 0, [C_x^1, C_x^2, C_x^3] \geq 0$ for $[x \geq 12]$. The region from $x = 9$ to $x = 12$ has very small variations in C_x and E_x and hence the major variations in the curve trends is observed only beyond $x = 12$. Also, we observe that in Fig. 3.4, three significant regions exist corresponding to high, medium and low quality of segmented vessel pixels (Q). The region with high Q corresponds to the early iterations when the number of actual vessel pixels identified are

more than the noisy false edge pixels ($TP_t >> FP_t$). The region with low Q corresponds to iterations when the number of false edge pixels being added exceed the actual vessel pixels ($TP_t << FP_t$). The third significant region is when Q is medium and change in iterative vessel estimates is significantly small.

The trends of the C and E curves in the regions when Q is high and Q is low are analyzed in (3.14)-(3.16). We observe that, curve C_t always has a non-decreasing trend (15).

$$C_{t+1} - C_t = \frac{1}{n_1 \cdot n_2} \sum_{i=1}^{n_1} \sum_{j=1}^{n_2} \{V_{t+1}(i,j) - V_t(i,j)\}, \tag{3.14}$$

Since new vessel pixels are added in each iteration,

$$\sum_{i=1}^{n_1} \sum_{j=1}^{n_2} V_{t+1}(i,j) \geq \sum_{i=1}^{n_1} \sum_{j=1}^{n_2} V_t(i,j) \Rightarrow C_{t+1} - C_t \geq 0. \tag{3.15}$$

$$\Rightarrow C_t \textbf{ always has non} - \textbf{decreasing trend}.$$

$$\textbf{Now, } E_{t+1} - E_t = \frac{1}{n_1 \cdot n_2} \sum_{i=1}^{n_1} \sum_{j=1}^{n_2} [|V(i,j) - V_{t+1}(i,j)| - |V(i,j) - V_t(i,j)|],$$

$$\Rightarrow \text{Using (12), } E_{t+1} - E_t = \frac{1}{n_1 \cdot n_2} \sum_{i=1}^{n_1} \sum_{j=1}^{n_2} [fp_{t+1}(i,j) + fn_{t+1}(i,j) - fp_t(i,j) - fn_t(i,j)]. \tag{3.16}$$

However, for E_t, we consider two separate cases to analyze the trends of E_t in high Q and low Q regions. In case 1 with high Q, $TP_t >> FP_t$. Here, the number of false vessel pixels in V_t (FP_t) are very small compared to the number of true vessel pixels (TP_t) added in consecutive iterations (3.17). Also, for each image, the sum of vessel pixels in the manually marked image remains constant, i.e., $TP_t + FN_t = constant$ (3.18). Hence in the high Q region, E_t has a non-increasing trend (3.19). In case 2 with low Q, $TP_t << FP_t$. Here, the number of false vessel pixels in V_t (FP_t) are significantly larger than the true vessel pixels (TP_t) (3.20). We observe that E_t has a non-decreasing trend in this region (3.21). Thus, to achieve the most accurate segmented vessel estimate, the iteration process must be stopped in the transition region from high Q to low Q.

Case 1: High Q, $[TP_t << FP_t]$.

$$\text{Iteratively, } TP_{t+1} \geq TP_t, FP_{t+1} \approx FP_t. \tag{3.17}$$

$$\Rightarrow TP_t + FN_t = \sum_{i=1}^{n_1}\sum_{j=1}^{n_2} V(i,j) = \text{constant}. \tag{3.18}$$

Using, (17), (18), $FN_{t+1} \leq FN_t$.

From (16), $\Rightarrow E_{t+1} - E_t \leq 0$.

$$\Rightarrow E_t \textbf{ has non} - \textbf{increasing trend}. \tag{3.19}$$

Case 2: Low Q, $[TP_t << FP_t]$.

$$\text{Iteratively, } FP_{t+1} \geq FP_t, TP_{t+1} \approx TP_t \tag{3.20}$$

$\Rightarrow FN_{t+1} \approx FN_t$.

From (16), $\Rightarrow E_{t+1} - E_t \geq 0$.

$$\Rightarrow E_t \textbf{ has non} - \textbf{decreasing trend}. \tag{3.21}$$

From the experimental standpoint, for an image from the DRIVE Test data set, the curve E and C as iterations proceed from $t = 0$ to $t = 10$ are shown in Fig. 3.5. Here, we observe that the best fit polynomial for C is of degree 3 and the best fit polynomial for E is of degree 4. Thus, the first, second and third derivatives must exist for both curves C and E. Let these derivatives be denoted by C_t^m and E_t^m, for $m = [1, 2, 3]$, respectively. These derivatives are computed iteratively using the backward difference rule as shown in (3.22).

$$\text{If, } C_t^0 = C_t, E_t^0 = E_t, \text{ then,} \tag{3.22}$$

$$E_t^m = E_t^{m-1} - E_{t-1}^{m-1}, m = [1, 2, 3].$$

$$C_t^m = C_t^{m-1} - C_{t-1}^{m-1}, m = [1, 2, 3].$$

Further, from Fig. 3.4, we observe that the iterative change in C_t and E_t are significantly small in the *medium* Q region than the high and low Q regions. This is intuitive

since in the *medium Q* region, fine vessel branches are detected and added to the existing vessel estimate. However, as soon as the noisy false edge regions, that are significantly larger in area when compared to the fine vessel branches, start getting identified and added to the vessel estimates, the change in C_t and E_t become considerably large, and this is when the *low Q* region begins. Based on this observation, a stopping criterion is designed for Algorithm 1 using the following property.

Property 1 *Assume C_t, E_t exist for $t = [1, 2...10..]$, and, they can be approximated as $C_t \approx \Lambda_0(t - t^*)^3 + \Lambda_1$, and $E_t \approx \Omega_0(t - t^*)^4 + \Omega_1$, where $\Lambda_0, \Lambda_1, \Omega_0, \Omega_1$ are constants. If the region with medium Q exists for at least 3 consecutive iterative steps (i.e., the change in the iterative vessel estimates are very small for at least 3 iterations), then the iteration t_f at which the first instance of $[C^1_{t_f} \geq 0, C^2_{t_f} \geq 0, C^3_{t_f} \geq 0]$ occurs will result in the best segmented vessel estimate.*

Let the region *medium Q* exist for at least 3 consecutive iterations starting at iteration t^* such that beyond the (t^*+3)th iteration the quality of pixel addition deteriorates, i.e., the number false positive pixels added as vessels increases. Then,

$$\sum_{i=1}^{n_1}\sum_{j=1}^{n_2} V_{t^*}(i,j) \approx \sum_{i}^{n_1}\sum_{j=1}^{n_2} V_{t^*+1}(i,j), \tag{3.23}$$

$$\sum_{i=1}^{n_1}\sum_{j=1}^{n_2} V_{t^*+1}(i,j) \approx \sum_{i=1}^{n_1}\sum_{j=1}^{n_2} V_{t^*+2}(i,j),$$

$$\sum_{i=1}^{n_1}\sum_{j=1}^{n_2} V_{t^*+3}(i,j) \geq \sum_{i=1}^{n_1}\sum_{j=1}^{n_2} V_{t^*+2}(i,j).$$

While transitioning from medium Q to low Q region,

both C_t and E_t have non-decreasing trends.

$$\Rightarrow C_{t^*} \approx C_{t^*+1} \approx C_{t^*+2}, C_{t^*+3} \geq C_{t^*+2}.$$

$$\Rightarrow E_{t^*} \approx E_{t^*+1} \approx E_{t^*+2}, E_{t^*+3} \geq E_{t^*+2}. \tag{3.24}$$

Using (3.24), and (3.22), we have,

$$\Rightarrow C^1_{t^*+1} = 0, C^1_{t^*+2} = 0, C^1_{t^*+3} \geq 0, \tag{3.25}$$
$$\Rightarrow E^1_{t^*+1} = 0, E^1_{t^*+2} = 0, E^1_{t^*+3} \geq 0.$$
$$\Rightarrow C^2_{t^*+2} = 0, C^2_{t^*+3} \geq 0, \tag{3.26}$$
$$\Rightarrow E^2_{t^*+2} = 0, E^2_{t^*+3} \geq 0.$$
$$\Rightarrow C^3_{t^*+3} \geq 0, E^3_{t^*+3} \geq 0. \tag{3.27}$$

Combining (3.24)-(3.27) at $t^* + 3$, we have,

$$[C^1_{t^*+3} \geq 0, C^2_{t^*+3} \geq 0, C^3_{t^*+3} \geq 0], \tag{3.28}$$
$$[E^1_{t^*+3} \geq 0, E^2_{t^*+3} \geq 0, E^3_{t^*+3} \geq 0].$$

For iterations $t > t^* + 3$, the number of false edge pixels that are identified and added becomes higher than the number of actual vessel pixels, which in turn reduces the accuracy of the segmented vessel estimate. Thus, for Algorithm 1, $t_f = t^* + 3$ is the iteration at which the best segmented vasculature with highest accuracy can be estimated.

Even though our assumption that C_t and E_t have repeated root at same iteration number (with constant terms removed) does not hold, the proposed stopping criterion still works well. In general, C_t behaves like an odd-degree polynomial. Thus, it may behave like a 5th-degree polynomial instead of 3rd. This may require stopping at the iteration where first 5 derivatives are non-negative. However, the proposed stopping criterion still leads to high accuracy due to two reasons. First, C_t is approximately constant in the entire medium Q region. Constant C_t over few iterations means fewer new vessels are added. Second, the medium Q region often spans a few iterations. Thus, stopping at any iteration in this region leads to similar accuracy. This is illustrated using sample images chosen from the datasets: DRIVE Test and STARE in Fig. 3.6. In Fig. 3.6 (a), the three consecutive derivatives of C_t and E_t become non-negative at the same iteration number; however, in Fig. 3.6 (b), C_t and E_t do not represent polynomials for the same repeated root, and hence, the first three derivatives of C_t become non-negative

in iteration $t = 4$, while the derivatives of E_t become non-negative at $t = 6$. However, since iterations $t = [4, 5, 6]$ lie in the medium Q region, where the change in iterative vessel estimates is very small, the accuracy of the segmented vessel in iteration $t = 4$ is similar to the accuracy of the vessel estimate at $t = 6$.

Based on (3.28) from Property 1, the stopping criterion for Algorithm 1 is defined as the iteration when the first three derivatives of curve C_t become non-negative. It is important to note that this iterative process continues for at least 3 iterations to obtain the first three derivatives for C_t.

3.4 Experimental Evaluation and Results

The performance of the proposed vessel segmentation algorithm is evaluated using the segmented vasculature and the manually marked vessels by the human observers. While manual vessel segmentation can take more than 2 hours [27], automated vessel segmentation algorithms aim to reduce manual computation time while maintaining acceptable accuracy of vessel segmentation. Like all prior works, we use the manual segmentations of the first human observer as ground truth for segmentation performance analysis. The vessel segmentation performance of the second human observer with respect to the first human observer within the retinal region is used to standardize the segmentation process.

The performance metrics that are used to evaluate the performance of the proposed iterative vessel segmentation algorithm are: pixel-based sensitivity (SEN), specificity (SPEC) and accuracy (ACC) of vessel segmentation and time taken to achieve the segmented vasculature. Also, the area under the ROC curves [21] is computed by varying the thresholds $\phi_1(t), \phi_2(t)$, and applying the stopping criterion for the particular choice of threshold functions. The threshold functions are varied as (3.29)-(3.30).

$$\text{If, } k = [1, 1.1, 1.2, ...3], \tag{3.29}$$

$$\phi_1(t) = 0.905 - 0.005[10k(t-1) - 9t],$$

$$\phi_2(t) = 205 + (t-1)^k. \tag{3.30}$$

To assess the overall performance of of vessel segmentation by the proposed iterative

method, we performed the following three sets of experimental evaluations. In the first experiment, the segmentation performance metrics were compared to the existing methods. In the second experiment, abnormal images with bright and red lesions from the STARE Abnormal data set were analyzed for segmentation performance. In the third experiment, segmentation performance of the peri-papillary vessel pixels were analyzed.

3.4.1 Vessel Segmentation Performance

For the proposed iterative vasculature segmentation algorithm, the segmentation performance metrics are given in Table 3.2.

Next, the performance and computational complexity of the proposed blood vessel segmentation algorithm in comparison with existing vessel segmentation methods is shown in Table 3.3.

From Table 3.3, we observe that the proposed iterative vessel segmentation approach outperforms all the existing methods except for the supervised approach by Ricci. et. al. [29] on the DRIVE Test data set, and the unsupervised Lam et. al. [21] method on the STARE data set. In the method by Ricci et. al. [29], support vector machine (SVM) classifiers were separately trained using 20,000 manually segmented randomly chosen pixels from the DRIVE and STARE data sets. This method is computationally more complex due to the use of the SVM classifier, and the classifier may need retraining for new data sets. Also, we observe that the proposed method is computationally faster than all existing unsupervised and supervised approaches since it requires less time for vessel segmentation. From Table 3.3, we observe that the AUC of the supervised methods is comparable to that of the proposed method. This is indicative of the robustness of the stopping criterion design with varying thresholds $[\phi_1(t), \phi_2(t)]$.

The ROC curves for all the three data sets are shown in Fig. 3.7 (a). In Fig. 3.7 (b), the variations in mean ACC by varying the thresholds as given in (3.29)-(30) are shown. Here, we observe that the images from the DRIVE and STARE data sets maintain significantly high ACC as k varies in the range $[1 \leq k \leq 2.2]$. For $k > 2.2$, the rate of change in vessel estimates becomes significantly high, such that C_t does not maintain a *medium* Q region for 3 consecutive iterations or more. This causes the iterative process to pick up a lot of false positive pixels before stopping, thus reducing

the segmentation ACC. The images from the CHASE_DB1 data set are 30^o FOV images from children that are centered at the papilla. For these images, if $[1 \leq k \leq 1.4]$, rate of new vessel addition is very small, resulting in low segmentation SEN and ACC. For $k > 2.4$, the rate of change in vessel estimates becomes very high. Thus, the *medium* Q region is limited to less than 3 consecutive iterations, causing a lot of false edge pixels to be added to the final segmented vessel estimate, thereby causing a sharp decrease in ACC as seen in Fig. 3.7 (b).

3.4.2 Abnormal Image Analysis

Existing works in [11], [29], [20], [21], [17] have shown that robustness of a vessel segmentation algorithm depends on the segmentation performance on abnormal retinal images with red lesions such as micro-aneurysms or hemorrhages and bright lesions such as exudates or cotton-wool spots. Vessel segmentations from two images with significant red and bright lesions from the STARE Abnormal data set have been analyzed by a number of existing methods [20], [21], [28] and [13]. The vessel segmentation performances on these two abnormal images by the proposed method in comparison with the methods in [28], and [13] are shown Fig. 3.8.

In Table 3.4, we compare the segmentation performance of all known methods with the proposed approach on the 10 images from the STARE Abnormal data set. We observe that the proposed method outperforms all other methods except the perceptive transform based method in Lam et. al. [21]. However, the computational complexity of the proposed approach is the lowest when compared to all other supervised and unsupervised methods.

3.4.3 Peripapillary vessel analysis

In retinal fundus images, the blood vessels in and around the optic disc are referred to as the peripapillary blood vessels. Many retinal abnormalities such as proliferative DR (PDR), glaucoma, central retinal vein occlusion, cilio retinal artery occlusion can lead to changes in the blood vessel structure mainly in the peripapillary region. For instance, neovascularization at the disc (NVD) caused due to PDR is evident if new blood vessels are visible within 1-optic disc diameter (1-DD) centered at the papilla [34]. Thus, the

performance of the proposed vessel segmentation system for extracting the peripapillary blood vessels in normal and abnormal images is analyzed here. For this purpose, the images from the DRIVE, STARE and CHASE_DB1 data set were manually annotated for the optic disc boundary and optic nerve head in each image, and then, a mask was created centered at the optic nerve head with 1-DD radius to extract the peripapillary region. The first 19 images from the STARE vessel segmentation data set contain the peripapillary region and hence peripapillary vessel detection was performed on these 19 images only.

The segmented vessel images of the DRIVE data set using the Marin et. al. method [13][1] , Soares et. al. method [28] [2] , Jiang et. al. method [22] and Staal et. al. method [27] [3] are downloaded from the respective websites for comparison. Next, the performance of the proposed vessel segmentation method in comparison with existing methods and the more detailed second human observer annotations for the STARE data set is shown in Fig. 3.9. The segmented vessel images are compared to the segmentation results produced by the Marin et. al. method [13], Soares et. al. method [28] and Hoover et. al. method [15] [4] .

Finally, we compute the performance of peripapillary vessel segmentation for the three data sets with respect to the two human observers in Table 3.5. We observe that for the DRIVE Test data set, the proposed segmentation algorithm results in 0.7% (with respect to Marin et. al. [13]) to 6.7% (with respect to Jiang et. al. [22]) improvement in vessel accuracy when compared to existing methods using the first human observer annotations, and 0.4% to 6.6% improvement against the same methods using the second human observer.

For the STARE data set, the proposed vessel segmentation achieves 1.81% (with respect to Marin et. al. [13]) to 6.45% (with respect to Hoover et. al. [15]) improvement in vessel accuracy when compared to existing methods using the first human observer annotations, and 6.9% (with respect to Soares et. al. [28]) to 7.8% (with respect to Hoover et. al. [15]) improvement using the second human observer annotations. For the

[1] Available at http://www.uhu.es/retinopathy/eng/bd.php

[2] Available at http://sourceforge.net/apps/mediawiki/retinal/index.php ?title=Segmentation_results

[3] Available at http://www.isi.uu.nl/Research/Databases/DRIVE/browser.php

[4] Available at http://www.parl.clemson.edu/ ahoover/stare/probing/index.html

CHASE_DB1 data set, the peripapillary vessel segmentation accuracy is greater than 90% with respect to both human observers.

3.5 Discussion and Conclusions

In this chapter, we have proposed an unsupervised iterative blood vessel segmentation algorithm using fundus images and tested it on three public data sets of DRIVE, STARE and CHASE_DB1. This algorithm iteratively extracts vessel pixels from a morphological vessel enhanced image from the negative green plane from each fundus image. The algorithm initiates with an initial estimate of the major portions of the blood vessels. Next, iteratively new vessel pixels are added to the existing vessel estimate by adaptive global thresholding until a stopping criterion is met. The proposed iterative segmentation algorithm is computationally simple, general and faster than all supervised and unsupervised algorithms developed so far.

The proposed algorithm depends on two threshold parameters that determine the rate at which vessel estimates change iteratively. The ROC curves that are constructed by varying these threshold probabilities demonstrate that the stopping criterion is robust to change in the adaptive threshold values since an average AUC of 0.9656 is achieved across the three data sets. Also, the proposed algorithm relies on the first 3 derivatives of the change in iterative vessel estimates to identify a novel stopping criterion that terminates the iterative vessel addition process while ensuring high accuracy of the segmented vasculature. Future efforts may be directed towards the analysis of the first 5 orders of derivatives for the change in iterative vessel estimates to develop a stopping criterion for high resolution fundus images.

The proposed vessel segmentation algorithm is very effective in abnormal retinal images with large red or bright lesions in close vicinity of the main vasculature, since the algorithm will stop before the iteration in which the large lesion regions are identified and added to the existing vessel estimate. However, this algorithm has one limitation. In retinal images with small microaneurysms close to the vasculature, the microaneurysms will be included as a part of the vasculature due to the regiongrow operation. Future work will be directed towards combining the proposed method with decision making approaches to further enhance the segmentation performance on abnormal retinal images

with such small lesions close to the vasculature.

The most significant features of the proposed segmentation algorithm is that it does not need to be retrained for new incoming data sets, and incurs low computational complexity. Unlike the proposed method, existing supervised segmentation approaches require a training set of pixels to train the vessel classifiers, and a specific threshold probability value at which the blood vessels with highest segmentation accuracy occur. For instance, the method developed by Fraz et. al. [12] need to be trained using 20,000 pixels, while the method by Soares et. al. [28] require 10^6 pixels from each data set under test for classifier parameter tuning. Such methods are more likely to perform poorly in the absence of manually marked groundtruth for new image sets with varying illumination and FOVs.

Another significant contribution of the proposed method is that it provides segmented vessels with high accuracy for peripapillary blood vessel extraction. It achieves greater than 90% peripapillary vessel segmentation accuracy for the DRIVE and CHASE_DB1 data set and greater than 77% accuracy for the STARE data set with respect to both human observers. Thus, the proposed segmentation algorithm can be useful for automated algorithms that detect the density, tortuosity or width of these peripapillary vessels for severity analysis of pathologies such as vein occlusions and glaucoma.

Unlike some methods that are fine tuned to handle abnormal retinal images in [21], the proposed vessel segmentation algorithm is generalizable, and robust against false edges, uneven illumination and pigmentation. The high speed, computational simplicity, and data independence of the proposed method makes it ideal for automated vessel pathology analysis for future research problems that analyze changes in the retinal vessel width [6] [8] [9]. Future work will be directed towards combining the proposed algorithm with DR screening systems such as [10] and to detect neovascularization in the peripapillary region. Redesigning the proposed method for vessel segmentation on wide field images with greater than 200^o FOV is a topic that requires further study.

Table 3.1: Definition of Notation.

Notation	Meaning
V	Manually marked vessel image.
V_f	Final segmented vasculature.
T	Tophat transformed vessel enhanced image.
V_t	Binary image representing vasculature estimated in iteration t. V_0 represents the major vessels at $t = 0$.
R_t	Residual image obtained by removing the pixels in the existing vessel estimate (V_t) from T.
V_{R_t}	Thresholded residual image from R_t using threshold $\phi_1(t)$. This contains the new vessel pixels identified in iteration t.
B_t	Base image to fill gaps between the new vessel pixels and the existing vessel estimate. It is the union of vessel pixels in V_{R_t} and V_t added to image T.
V_{t+1}	Vasculature at iteration $t+1$ obtained from region grown base image (B_t) with an adaptive threshold $\phi_2(t)$.
C_t	Change in the segmented vessel estimate in iteration 't' defined as the difference between number of pixels in V_t and V_0 divided by the total number of image pixels.
C_t^m	For $m = [1, 2, 3]$, the first, second and third order derivatives of C_t computed using backward difference method.
E_t	Error in the number of vessel pixels between V_t and manually marked vessels V divided by the total number of pixels.
E_t^m	For $m = [1, 2, 3]$, the first, second and third order derivatives of E_t computed using backward difference method.
Q_t	Quality of the segmented vessel estimate V_t in iteration 't' defined as the ratio between the number of actual vessel pixels and the number of false edge pixels.

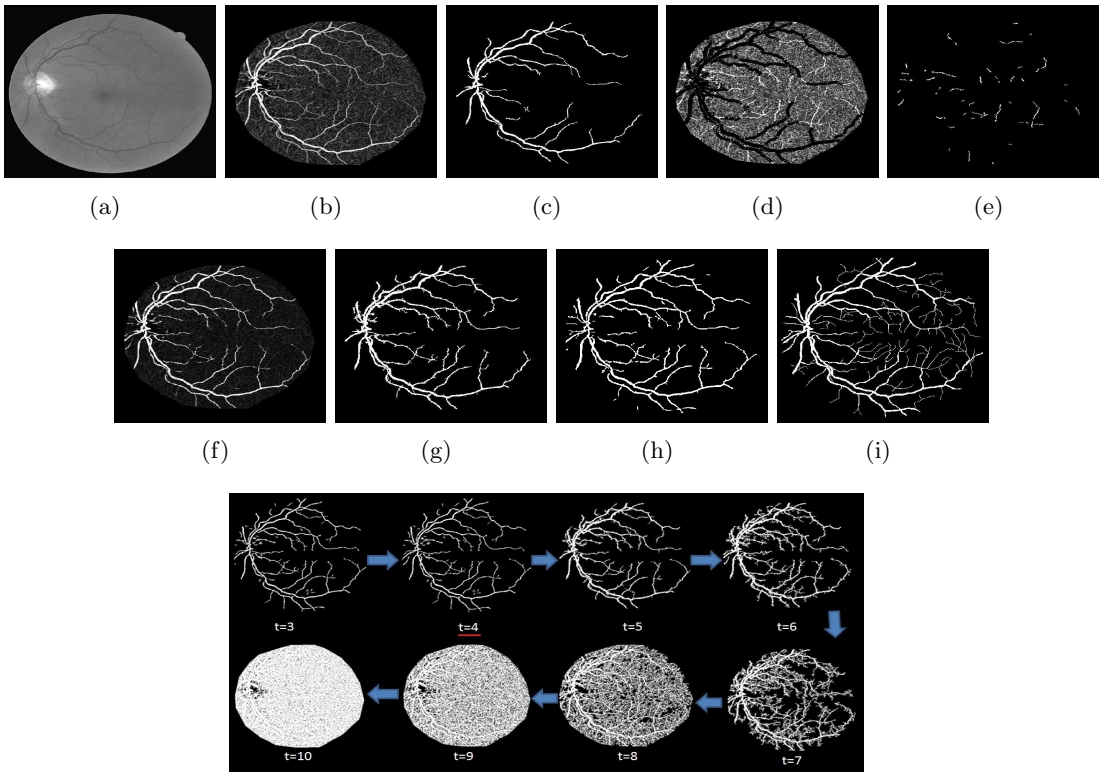

Figure 3.1: The iterative vessel segmentation algorithm on an image with 45^o FOV. (a) Green plane image (I). (b) Vessel enhanced image by tophat reconstruction (T). (c) Major vessels extracted from T (V_0). (d) Residual image R_0 with pixels from V_0 removed from image T. (e) New vessel pixels identified by thresholding R_0 (V_{R_0}). (f) Base image B_0 obtained by combining pixels in V_{R_0} and V_0 on image T. (g) V_1 extracted after region-growing. (h) Final vasculature estimate obtained after 4 iterations (V_f). (i) Manually marked vasculature (V). (j) Vessel estimates extracted after each iteration $t = 3$ to $t = 10$ by repeating steps (d) to (g) iteratively. A stopping criterion is required to stop the iteration at $t = 4$ to prevent over-segmentation.

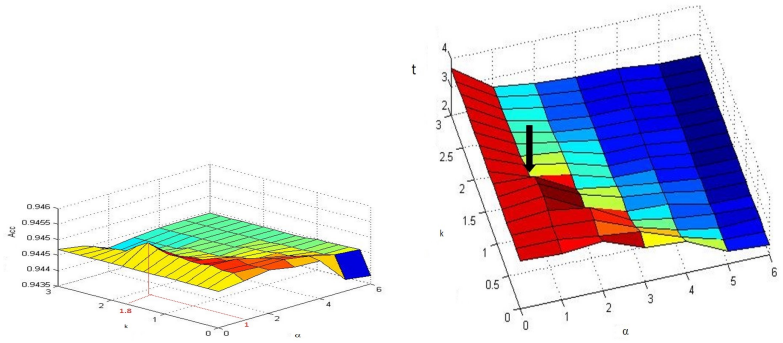

(a) (b)

Figure 3.2: Estimation of threshold function $\phi_2(t)$ for region-growing. (a) The highest mean vessel segmentation accuracy (ACC^l) versus the threshold function parameters $[\alpha, k]$. (b) The mean iteration number (t_l) corresponding to highest ACC^l versus threshold function parameters $[\alpha, k]$ on the DRIVE Train set of images. The arrow marks the ideal choice of threshold function parameters.

Table 3.2: Performance of the Proposed Method on the test data sets. Mean performance metrics and their standard deviation is given in ().

Segmentation	AUC	ACC	SEN	SPEC	Time
DRIVE Test					
Second Observer	-	0.9485 (0.005)	0.7798 (0.058)	0.973 (0.008)	-
Proposed	0.967	0.9494 (0.005)	0.7395 (0.062)	0.9782 (0.007)	2.45 (0.32)
STARE					
Second Observer	-	0.9356 (0.013)	0.9024 (0.054)	0.939 (0.018)	-
Proposed	0.967	0.9560(0.01)	0.7317 (0.053)	0.9842 (0.007)	3.96 (0.27)
STARE Normal					
Second Observer	-	0.931 (0.01)	0.9353 (0.015)	0.9304 (0.011)	-
Proposed	0.971	0.9586 (0.006)	0.7571 (0.088)	0.9877 (0.003)	4.04 (0.28)
STARE Abnormal					
Second Observer	-	0.940 (0.014)	0.8694 (0.059)	0.9477 (0.019)	-
Proposed	0.964	0.9535 (0.017)	0.7062 (0.10)	0.9808 (0.026)	3.88 (0.25)
CHASE_DB1					
Second Observer	-	0.959 (0.0068)	0.8286 (0.052)	0.9723 (0.01)	-
Proposed	0.962	0.9467(0.0076)	0.7615 (0.052)	0.9575 (0.003)	7.91 (0.68)

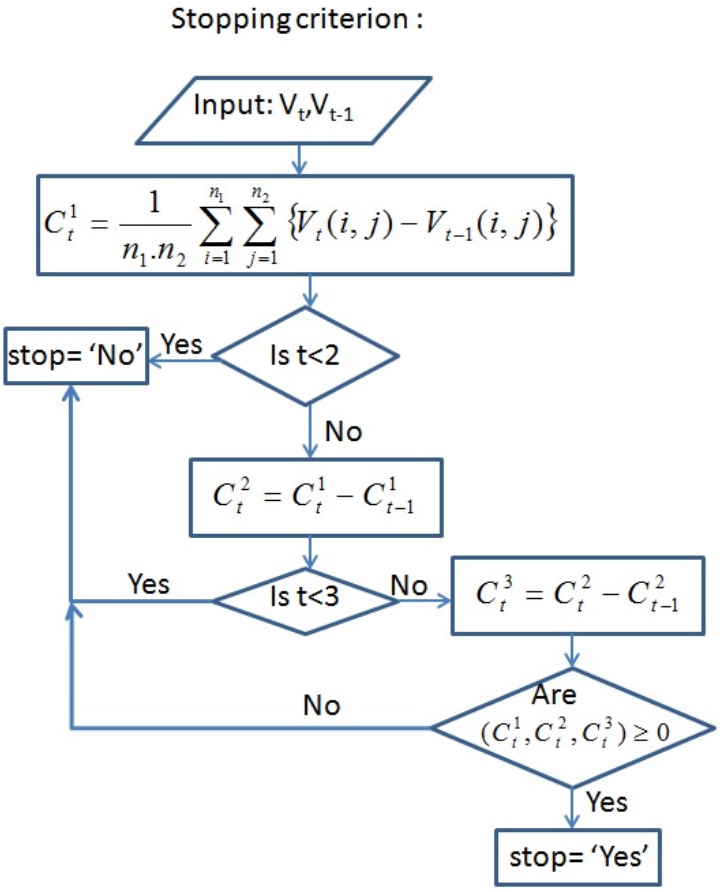

Figure 3.3: The stopping criterion for the iterative algorithm. If the number of iteration 't' is less than 3, or if the sign of the C_t^1, C_t^2, C_t^3 are not all non-negative, then iterations are continued. However, if all the first three derivatives of C become non-negative, the iterations are stopped.

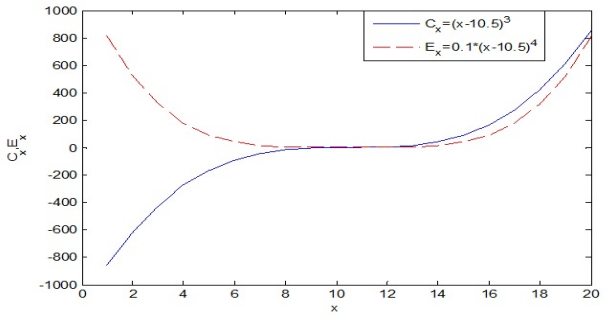

x=	1	2	3	4	5	6	7	8	9	10	11	12	13	14	15	16	17	18	19	20
C_x	-857.4	-614.1	-421.9	-274.6	-166.4	-91.13	-42.88	-15.63	-3.375	-0.125	0.125	3.375	15.63	42.88	91.13	166.4	274.6	421.9	614.1	857.4
C^1_x	0	243.3	192.3	147.3	108.3	75.25	48.25	27.25	12.25	3.25	0.25	3.25	12.25	27.25	48.25	75.25	108.3	147.3	192.3	243.3
C^2_x	0	0	-51	-45	-39	-33	-27	-21	-15	-9	-3	3	9	15	21	27	33	39	45	51
C^3_x	0	0	0	6	6	6	6	6	6	6	6	6	6	6	6	6	6	6	6	6
E_x	814.5	522	316.4	178.5	91.51	41.01	15.01	3.906	0.506	0.006	0.006	0.506	3.906	15.01	41.01	91.51	178.5	316.4	522	814.5
E^1_x	0	-292.5	-205.6	-137.9	-87	-50.5	-26	-11.1	-3.4	-0.5	0	0.5	3.4	11.1	26	50.5	87	137.9	205.6	292.5
E^2_x	0	0	86.9	67.7	50.9	36.5	24.5	14.9	7.7	2.9	0.5	0.5	2.9	7.7	14.9	24.5	36.5	50.9	67.7	86.9
E^3_x	0	0	0	-19.2	-16.8	-14.4	-12	-9.6	-7.2	-4.8	-2.4	0	2.4	4.8	7.2	9.6	12	14.4	16.8	19.2

Figure 3.4: Theoretical example for curves corresponding to the iterative change in blood vessels C_x and iterative error incurred E_x. The repeated root for curves E_x, C_x occurs in the region with medium Q. As iterations proceed beyond the repeated root, the first three derivatives of E_x and C_x become non-negative.

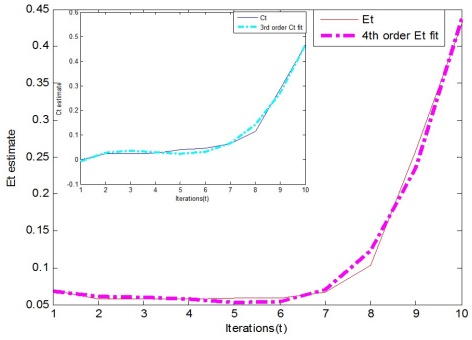

Figure 3.5: Change in segmented vessel estimates C_t and the iterative error incurred E_t for an image from the DRIVE Test data set along with the best fit polynomials for C_t with degree 3 and for E_t with degree 4, respectively.

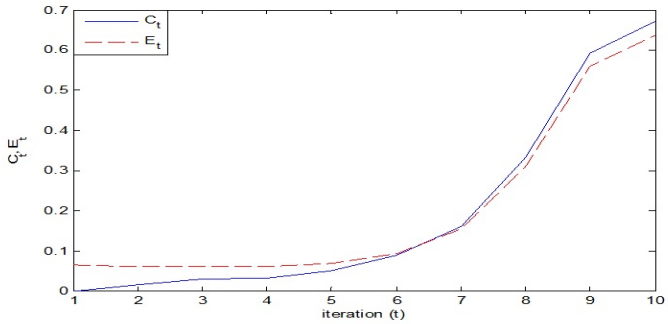

t=	1	2	3	4	5	6	7	8	9	10
C_t	0	0.014411	0.028886	0.030909	0.050725	0.088534	0.161522	0.332414	0.592704	0.672145
C^1_t	-	0.014411	0.014475	0.002023	0.019816	0.037809	0.072988	0.170892	0.26029	0.079441
C^2_t	-	-	6.47E-05	-0.01245	0.017793	0.017993	0.035179	0.097904	0.089399	-0.18085
C^3_t	-	-	-	-0.01252	0.030245	0.0002	0.017187	0.062724	-0.00851	-0.27025
E_t	0.063718	0.061024	0.060395	0.060854	0.068377	0.092657	0.154564	0.310398	0.560054	0.6376
E^1_t	-	-0.00269	-0.00063	0.000459	0.007523	0.02428	0.061907	0.155834	0.249656	0.077547
E^2_t	-	-	2.06E-03	0.001088	0.007064	0.016757	0.037626	0.093928	0.093822	-0.17211
E^3_t	-	-	-	-0.00098	0.005976	0.009693	0.020869	0.056301	-0.00011	-0.26593

(a)

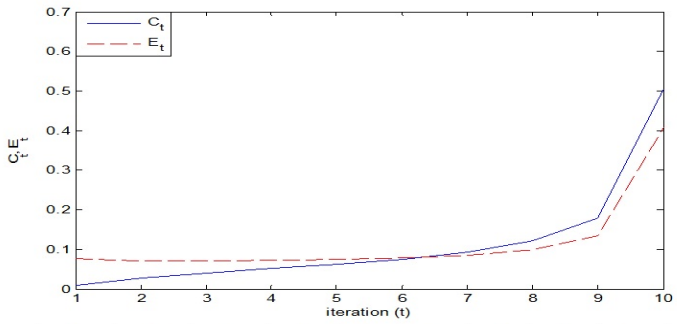

t=	1	2	3	4	5	6	7	8	9	10
C_t	0.00949	0.028507	0.039219	0.05156	0.062629	0.074647	0.092831	0.121814	0.179898	0.506854
C^1_t	-	0.019018	0.010712	0.01234	0.01107	0.012018	0.018184	0.028983	0.058084	0.326956
C^2_t	-	-	-0.00831	0.001628	-0.00127	0.000948	0.006167	0.010799	0.029101	0.268872
C^3_t	-	-	-	0.009934	-0.0029	0.002219	0.005219	0.004632	0.018302	0.239771
E_t	0.075937	0.070125	0.069837	0.071733	0.074235	0.078142	0.08586	0.099358	0.133435	0.40887
E^1_t	-	-0.00581	-0.00029	0.001896	0.002502	0.003907	0.007718	0.013498	0.034077	0.275435
E^2_t	-	-	0.005524	0.002185	0.000606	0.001404	0.003812	0.005779	0.02058	0.241357
E^3_t	-	-	-	-0.00334	-0.00158	0.000799	0.002407	0.001968	0.0148	0.220778

(b)

Figure 3.6: The vessel estimate curves C_t and E_t for a particular image from (a) DRIVE Test, and (b) STARE, respectively. The stopping iterations are (a) $t_f = 5$, (b) $t_f = 4$. In (a) the three consecutive derivatives for E_t and C_t become non-negative at the same iteration step. In (b), the iteration for three consecutive non-negative derivatives corresponding to C_t and E_t are different.

Table 3.3: Comparative Performance of Proposed Model with existing works on the DRIVE and STARE data sets.

Test Data:	DRIVE	Test			
Method	ACC	SPEC	SEN	AUC	Time
Niemeijer et. al. [26]	0.942	0.969	0.689	0.93	-
Staal et. al. [27]	0.944	0.977	0.719	0.952	15 mins
Soares et. al. [28]	0.946	0.978	0.733	0.961	∼3 mins
Ricci et. al. [29]	0.959	0.972	0.775	0.963	-
Marin et. al. [13]	0.945	0.98	0.706	0.958	∼90s
Fraz et. al. [12]	0.948	0.981	0.74	0.974	∼100 s
Jiang et. al. [22]	0.891	0.90	0.83	0.932	8-36s
Mendonca et. al. [17]	0.945	0.976	0.734	-	2.5min
Al-Diri et. al.[23]	-	0.955	0.728	-	11 mins
Lam et. al. [21]	0.947	-	-	0.961	13 mins
Budai et. al. [24]	0.949	0.968	0.759	-	11s
Miri et.al. [18]	0.943	0.976	0.715	-	∼50s
Proposed	**0.949**	**0.978**	**0.739**	**0.967**	**2.45s**
Test Data:	STARE				
Staal et. al. [27]	0.952	0.981	0.697	0.961	15 mins
Soares et. al. [28]	0.948	0.975	0.72	0.967	∼3 mins
Ricci et. al. [29]	0.965	0.939	0.903	0.968	-
Marin et. al. [13]	0.952	0.982	0.694	0.977	∼90s
Fraz et. al. [12]	0.953	0.976	0.755	0.976	∼100 s
Hoover et. al. [15]	0.9275	0.81	0.65	0.75	5min
Jiang et. al. [22]	0.901	0.90	0.857	0.929	8-36s
Lam and Yan [20]	0.9474	-	-	0.9392	8 mins
Mendonca et. al. [17]	0.944	0.973	0.699	-	3min
Al-Diri et. al.[23]	-	0.968	0.752	-	-
Lam et. al. [21]	0.957	-	-	0.974	13 mins
Budai et. al. [24]	0.938	0.975	0.651	-	16s
Proposed	**0.956**	**0.984**	**0.732**	**0.967**	**3.95s**

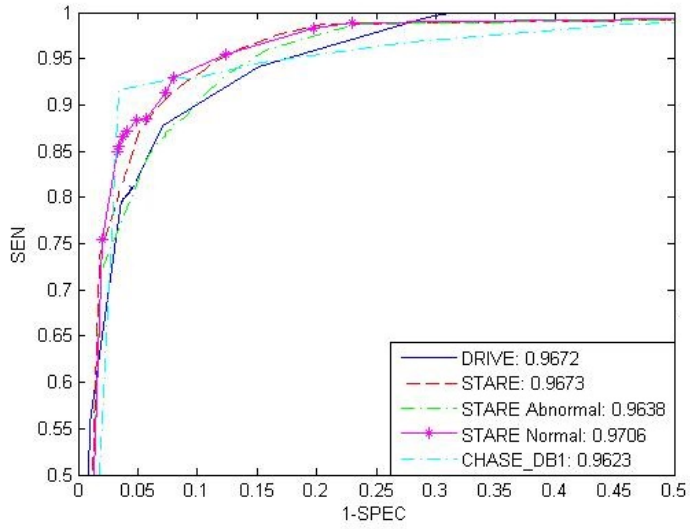

(a)

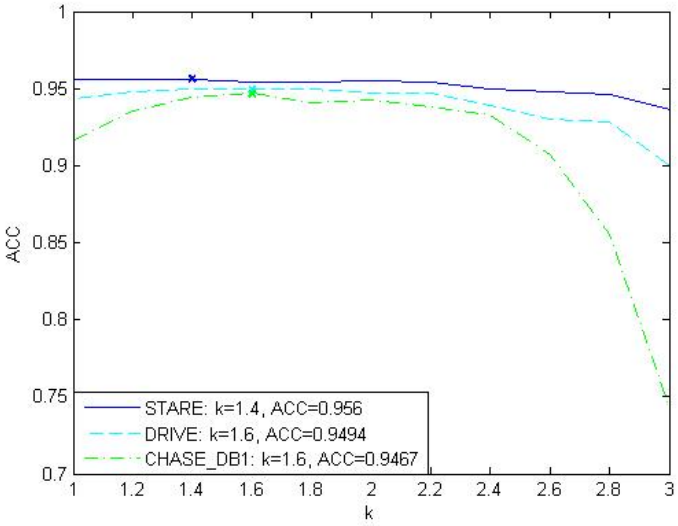

(b)

Figure 3.7: (a) ROC curves for blood vessel segmentation on DRIVE test, STARE and CHASE_DB1 data sets. (b) Variation in mean segmentation accuracy by varying the thresholds. Highest ACC is achieved for the DRIVE Test, STARE and CHASE_DB1 data sets with $k = [1.4, 1.6, 1.6]$, respectively.

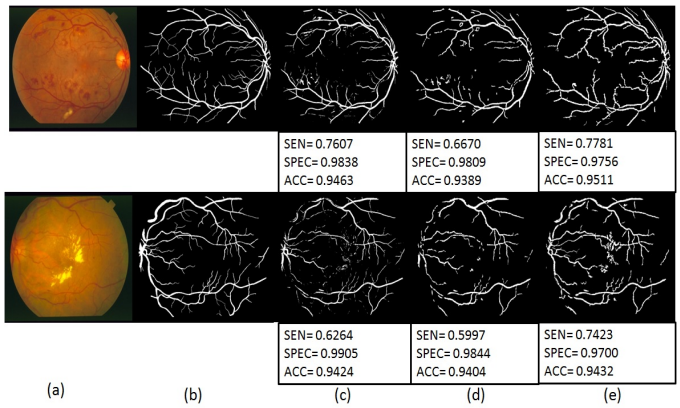

Figure 3.8: Vessel segmentation on abnormal images. First row depicts vessel segmentation on an image with red lesions while the second row depicts segmentation on an image with bright lesions. (a) Image. (b) Manually marked vessels. (c) Segmentation by Soares et. al. (d) Segmentation by Marin et. al. (e) Segmentation by proposed method.

Table 3.4: Segmentation Performance on the STARE Abnormal data set.

Method	ACC	AUC	Time
Hoover et. al. [15]	0.9211	0.7590	5 mins
Jiang et. al. [22]	0.9352	0.9343	8-36 s
Mendonca et. al. [17]	0.9426	-	3 mins
Soares et. al. [28]	0.9425	0.9571	3 mins
Vermeer et. al. [19]	0.9287	0.9187	-
Marin et. al. [13]	0.9510	-	90 s
Lam and Yan [20]	0.9474	0.9392	8 mins
Lam et. al. [21]	0.9556	0.9707	13 mins
Proposed	**0.9535**	**0.9638**	**3.87 s**

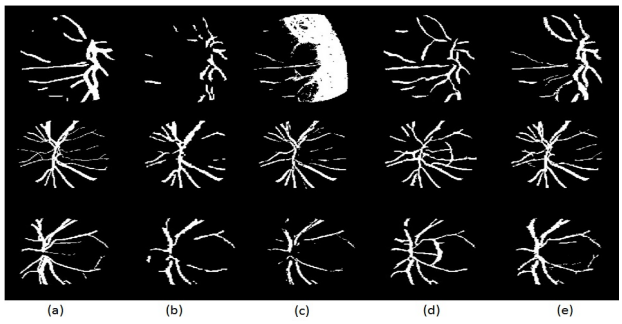

Figure 3.9: Peripapillary vessels segmented for the STARE set of images. (a) Second Human Observer. (b) Marin et. al. method. (c) Soares et. al. method. (d) Hoover et. al. method. (e) Proposed Method.

Table 3.5: Peripapillary Vessel Analysis. ACC and the standard deviation is given in () with respect to the two human observers.

Method	First Observer	Second Observer
	DRIVE Test	
Supervised		
Marin et. al. [13]	0.9141 (0.0165)	0.9189 (0.0177)
Soares et. al. [28]	0.9116 (0.0178)	0.9167 (0.0141)
Staal et. al. [27]	0.9103 (0.0202)	0.9146 (0.0176)
Unsupervised		
Jiang et. al. [22]	0.8625 (0.0261)	0.8656 (0.0243)
Proposed	**0.9202 (0.0227)**	**0.9227 (0.0183)**
	STARE	
Supervised		
Marin et. al. [13]	0.8053 (0.0372)	0.7189 (0.0584)
Soares et. al. [28]	0.8038 (0.0480)	0.7239 (0.0536)
Unsupervised		
Hoover et. al. [15]	0.7685 (0.0341)	0.7179 (0.0387)
Proposed	**0.8181 (0.0256)**	**0.7741 (0.0587)**
	CHASE_DB1	
Unsupervised		
Proposed	**0.9043 (0.0353)**	**0.9049(0.0368)**

Chapter 4

Automated Optic Disc Segmentation

4.1 Introduction

Automated detection of optic disc (OD) is important for early detection of glaucoma [39]. Disc size, neuro-retinal rim and cup area features are used to detect a glaucomatous retina [40]. OD and the position of vessel origin (VO) are the main anatomical features in retinal fundus images. The VO position is an important reference point for detecting the macula, and thereby grading macular pathologies such as diabetic maculopathy, macular edema and macular ischemia [41]. Also, automated OD detection plays an important role in developing automated "diagnosis expert systems" for diabetic retinopathy (DR), as its segmentation is a key component to correctly identify other bright features in the images such as the bright lesions (hard exudates or cotton-wool spots) [42] [3]. Besides the position of the OD, the VO seed point is another important feature of a fundus image that is needed for vessel tracking methods to detect vessel features like vessel tortuosity and vessel branching patterns [42]. Also, automated segmentation of the OD boundary and the VO position are essential for automated eye motion tracking during laser surgeries [40].

The detection of the OD region is challenging due to the fact that the size, shape and color of the OD vary from one person to another and with the field of view (FOV) of the fundus images. Estimates regarding the size of the OD vary from one-seventh

of an entire image, or from one-tenth to one-fifth of the image [43]. Along with the disparity in the size and shape of the OD in images, another challenge arises from fundus images that depict a relatively dark OD due to illumination issues of the non-mydriatic camera. Additionally, in images with multiple abnormalities, such as images with myelinated nerve fiber, the detection of OD becomes significantly more challenging. Also some prior works have failed to detect the OD in images with exudates similar in shape and size as the OD [44]. Other concerns adding to the challenge of segmenting the region of the OD include instances when peripapillary atrophy is present and the shape of the OD is further distorted.

In this chapter, we detect the OD at the intersection of the largest red region and one of the brightest regions in the fundus image such that the OD regions satisfy certain compactness constraints. The method of OD neighborhood region detection by minimizing the intensity sum and maximizing the bright region solidity, i.e., Minimum Intensity Maximum Solidity *MinIMaS*, has been presented in our earlier work [10]. In this chapter, we modify this method to maximize the vessel-sum and solidity of OD regions and propose a new algorithm referred as *Maximum Vessel-Sum and Solidity (MaxVeSS)* to detect the OD candidate region. Also, in this chapter we extend our analysis to segment the exact OD boundary and VO pixel location instead of just estimating the OD neighborhood region. This work will aid cup-to-disc ratio assessment for glaucoma detection and screening algorithms.

In this chapter, we propose an OD detection algorithm that segments the OD region with 100% success on 1487 retinal fundus images from 5 different public data sets with FOV in the range [30^o to 50^o] and computes the vessel origin with less than 10 pixels error in less than 5 seconds per image. The proposed algorithm relies on the structure of the bright regions in fundus images and their relative positions in the neighborhood of the biggest red region (the retinal blood vessels) to detect the OD region. The proposed algorithm consistently estimates the OD region such that 94.37% of the total images under evaluation have higher than 70% overlap between the manually segmented OD and the automatically segmented OD. This chapter makes three key contributions. First, selection of a *circular* structuring element, as opposed to linear during morphological transformation leads to significantly high accuracy in detecting the OD boundary and less error in detecting the VO. Second, the proposed *MaxVeSS* algorithm detects the

OD neighborhood with high accuracy. Third, the OD detection and VO location are computed by the same algorithm; these were treated as two separate problems in the past. The significance of this chapter is two-fold. First, the proposed OD boundary and VO detection algorithms presented in this chapter are the fastest reported so far. Second, the proposed OD segmentation algorithm is robust to variations in retinal images caused due to illumination artifacts or retinal abnormalities such as myelination or peripapillary atrophy.

The organization of this chapter is as follows. In Section 4.2, the existing OD detection and segmentation methods are reviewed. In Section 4.3, the proposed OD segmentation algorithm is presented. In Section 4.4 the experimental results of automated OD segmentation are presented. Conclusions and discussion are presented in Section 4.5.

4.2 Overview of Prior Work

Related work regarding OD detection using fundus images can be broadly categorized into two groups: 1) those based on the shape, color and structure of OD, and 2) those based on the properties of the retinal vasculature. The first category includes well-known methods that rely on the appearance and size of the OD [45], such as methods utilizing the highest average variation among adjacent pixels in a specific window size similar to that of the OD [43].

Other methods belonging to the first category include model-based approaches such as the template-matching method that made use of averaging of color-normalized images to yield a gray template, followed by computation of the normalized correlation coefficient to find the best match between the template and test images in [46]. Additionally, the Hausdorff-based template matching method used pyramidal decomposition, which aided the detection of large candidate objects in the image, followed by the computation of a confidence level for each OD candidate region based on the ratio of the mean intensity inside and in the immediate neighborhood of the candidate in [47]. Yet another method identified the OD location using template matching and directional matched filter in [48]. Further, the OD segmentation was performed using a fast hybrid level-set algorithm that combined the OD region information and edge gradient to

estimate the evolution of the OD curve. The first category also relates to algorithms that apply various transformations to images, such as the Haar-based discrete wavelet transform on the green plane of the image to create a resolution pyramid, where the brightest pixel at the fifth level of the pyramid is selected as the OD in [45]. Also, the Circular Hough transform has been employed to detect a large circular OD in [39] after the edges were detected in an image by applying the Sobel operator followed by thresholding. The method in [42] first located a pixel belonging to the OD region, and then applied boundary segmentation by morphology, edge detection and circular Hough transforms.

The second category of methods examine the retinal vasculature for locating the OD, since the OD is the point of entrance of the optic nerve and blood vessels which branch out into finer vessels through the retina. One such method in [44] used a fuzzy convergence algorithm that analyzed six binary vessel segmentations obtained from the green plane of the image to construct a cumulative voting image or a convergence image which was smoothened and thresholded to determine the best convergence point. Another method in [45] applied a search on the branching network patterns formed by the blood vessels to converge to the region where most paths ended, followed by the application of Hough transform on all such regions to finally locate the OD. Another method in [49] applied an OD template using the Laplacian of Gaussians to extract the vertical edges of the main blood vessels in the OD, which was correlated to the intensity of the test images using the Pearson-R correlation. The method in [50] localized the OD by tracking the blood vessels using Gabor filters to detect the peaks in nodes via phase portrait analysis and located the OD at the focal point of the vessels using Hough transform. A graph-based approach in [51] applied graph-cut techniques with compensation terms associated with the blood vessels based on the relationship between neighbor pixels and likelihood of the pixels to belong to foreground or the background based on prior information. The method in [52] applied watershed transform for detecting the OD location and disc boundary using the information regarding the major vessel arcade. Besides, maximization of vessel pattern-based entropy is used to detect the location of the OD in [53].

Some algorithms, however, have combined the two categories such as the method that locates the OD based on the structure of the OD, the convergence of blood vessels

at the OD and the variation in the size of the blood vessels entering the OD in [54]. Another method used the feature based k-nearest neighbor (kNN) classifier for training and extracting the OD in [55]. Also, another model located the OD by fitting a 16-point distribution model as an anatomical template to images by optimizing the cost function that was represented by the probabilistic vessel orientation, the width atlases and kNN based distance regression at pixel level in [56]. The method in [41] proposed an ensemble of pyramidal decomposition, edge detection, entropy-filter based detection, Hough transform and feature vector based algorithms for detecting the OD. Another method in [57] used the principal component image plane followed by removal of vessel regions, image inpainting, stochastic watershed transform and regional discrimination for the OD boundary detection.

Most existing works focusing on OD segmentation deal with OD localization or OD boundary segmentation, but not both [52]. In this chapter we propose a method that combines the two categories of OD segmentation such that the brightness, compactness, elliptical extent and vicinity of the blood vessels are properties to identify the OD boundary and the VO location. The proposed algorithm is computationally simple and it has consistent OD segmentation performances on both normal and abnormal retinal images.

4.3 Materials and Method

In this chapter, we propose a novel rule-based OD boundary segmentation and VO detection algorithm generalizable across data sets comprising of retinal images with varying fields of view (FOV), varying contrast and illumination intensities and varying retinal abnormalities. This algorithm is implemented on a Laptop (2.53 GHz Intel Core i3 and 2Gb RAM) using MATLAB. Although OD is generally the brightest element in retinal images, the entire OD region is not equally brightly illuminated. The thick blood vessels at the OD separate the OD region into several smaller brightly illuminated regions. For accurate boundary detection of the complete OD, it is imperative to detect all such bright OD regions. To facilitate this, we propose a two-step approach, where in the first step, the brightest OD candidate region is detected and its neighborhood is selected as the OD neighborhood region. In the second step, additional bright regions are

detected within the OD neighborhood. A convex hull is then created around all bright regions retained within the OD neighborhood region and a best fit ellipse around this convex hull is the segmented OD boundary. Finally, the position of VO is determined at the centroid of the blood vessels that lie within the segmented OD boundary.

The first step for OD segmentation regarding the identification of the brightest OD candidate region and the OD neighborhood is the most critical operation since the structure and pixel intensities of the OD region vary across fundus images. For instance, in some abnormal fundus images from patients with non-proliferative DR, bright lesions such as hard exudates and cotton-wool spots have similar structural compactness and brightness as the OD. Also, abnormal fundus images with myelinated nerve fiber may contain such structurally identical and bright regions as the OD. To facilitate accurate OD identification in normal and abnormal fundus images, we implement a *Maximum Vessel-Sum and Solidity (MaxVeSS)* algorithm that detects the OD neighborhood as the region where the reddest and brightest regions of the fundus image intersect under some vessel intensity and region compactness constraints.

4.3.1 Data

For OD segmentation performance analysis, retinal images are manually annotated for the OD boundary (D) and the pixel corresponding to the VO (O) using the GIMP software [58]. The proposed OD segmentation algorithm is tested on fundus images from the following publicly available data sets. All the images from the DRIVE, DIARETDB0, DIARETDB1 and CHASE_DB1 are manually annotated for the OD boundary and VO pixel location.

- DRIVE [59] data set contains 40 images with 45^o FOV and size of [584x565] or [730x490] pixels.
- DIARETDB1 [60] data set contains 89 images with 50^o FOV and size of [1500x1152] pixels.
- DIARETDB0 [61] data set contains 130 images with 50^o FOV and size of [1500x1152] pixels.
- CHASE_DB1 [30] data set contains 28 images with 30^o FOV and of size [960x999]

pixels. These images correspond to two images per patient (one image per eye) for 14 children [12].

- MESSIDOR [62] data set, contains 1200 images with 45^o FOV in 3 sets of 400 images each from 3 ophthalmic departments named Laribiosiere, CHU de Etienne and LATIM-CHU de BREST, respectively. Each image is of size [1440x960], [2240x1488], or [2304x1536] pixels respectively. The manual annotations for OD boundary of each image is obtained from [57]. The VO pixel is manually segmented for 500 images that are sub-categorized as Base 24 (data from CHU de St Etienne), Base 31, Base 32, Base 33 and Base 34 (data from LATIM-CHU de BREST) by the authors.

4.3.2 Proposed Method

OD in a retinal fundus image is generally the brightest and the most compact structure lying in the vicinity of blood vessels that are the thickest at the point of vessel origin and become narrow as they branch away from the OD. The proposed algorithm incorporates this retinal structure property to extract the major blood vessels and the bright regions in a fundus image. Next, the OD is detected as the bright region with highest compactness and the most number of blood vessel pixels in its vicinity [52] [53]. As a pre-processing step, the green plane of each color fundus image is resized to [500x500] and the pixel intensities are scaled in the range [0,1], followed by contrast enhancement, resulting in image I. Next, I is morphologically eroded using a structuring element, followed by image reconstruction. This reconstruction operation enhances the compactness of brightly illuminated regions that include bright lesions, OD and contrast variations around the blood vessels. The reconstructed image is then subtracted from I, scaled in [0,1], and subjected to contrast enhancement to yield a morphologically transformed image I_r.

Selection of a structuring element for the morphological transformation of image I to I_r is key to the detection of OD boundary. While image erosion with a small structuring element can disintegrate the OD into several small bright regions with low compactness, a large structuring element can enlarge the OD boundary, thereby leading to incorrect OD segmentation. The impact of linear and circular structuring elements

on an image from the DIARETDB0 data set is shown in Fig. 4.1. From Fig. 4.1 we observe that circular structuring elements are most suitable for detecting the bright OD regions. This is a key result of this chapter, as some prior morphological constructions were based on linear structuring elements. The impact of this selection on accuracy of OD detection and VO location is significant. Empirically, we observed that for resized fundus images to [500x500] pixels, the average minor axis lengths of the actual OD region for images from the DRIVE, DIARETDB0, DIARETDB1, CHASE_DB1 and MESSIDOR data sets are 73, 70, 60, 90 and 45 pixels, respectively. Since the OD is divided into four major quadrants by the thick blood vessels, a circle as structuring element with radius one quarter of the actual OD diameter is capable of extracting one quadrant of the OD. Thus, for the image in Fig. 4.1, the minor axis length is 70 pixels, and a circular structuring element with radius 17 pixels extracts all the major bright regions corresponding to the OD with the least error in OD boundary estimation. Further, for the images from DRIVE, DIARETDB0, DIARETDB1, CHASE_DB1 and MESSIDOR data sets, a circular structuring element with radius 18, 17, 15, 22, 11, respectively, are used for the morphological reconstruction.

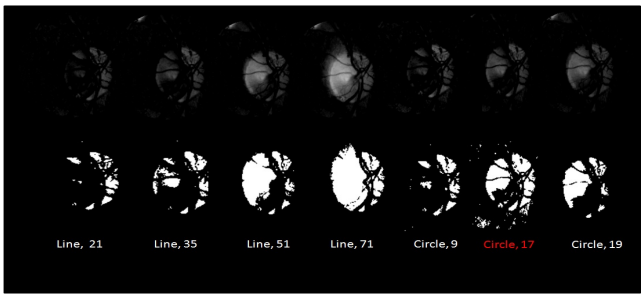

Figure 4.1: Bright region extraction using different structuring elements for morphological transformation. Top row represents morphologically transformed image I_r using a horizontal linear structuring element of a certain length (Line, [pixel length]), or a circular structuring element with a certain radius (Circle, [pixel radius]). Second row represents the image containing the bright regions obtained by thresholding the respective image I_r. For this image from DIARETDB0 data set, a circular structuring element with radius 17 results in the best segmented OD.

The process of locating the OD neighborhood region, detecting the OD boundary

($\hat{D}$) and the VO location ($\hat{O}$) is described below. The notations and their definitions used in this OD detection algorithm are defined in Table 4.1.

OD Neighborhood Detection: The MaxVeSS Algorithm

To locate the vicinity of the OD region at the intersection of the largest red region and the bright regions in image I as in [10], the major blood vessels and bright regions are first detected. To extract the major blood vessel regions from I, a smoothened low-pass filtered image $LPF(I)$ is subtracted from I to obtain a high-pass filtered image. Here, the low-pass filter is a median filter with window size [20x20] as used in [10] [31]. This high-pass filtered image is then thresholded to extract pixels less than 0, and the absolute pixel strengths of the thresholded image are contrast adjusted to extract the major vessels I_v as shown in (4.1). An image with bright regions (I_b) is extracted by adding the pixel intensities in I_r to the histogram equalized version of I, followed by scaling the resultant image in [0,1] and thresholding at pixel intensity value 0.9 in (4.2). Next, an *Overlap* function is defined with a neighborhood parameter $\nu = 30$, such that if pixels in I_v are located in the neighborhood of pixels in I_b, bright candidate regions (R) are detected in I_b [10] using (4.3). Among all these bright candidate regions, the regions that are highly elliptical (denoted by a high ratio of major and minor axis lengths $\frac{\Phi(R_e)}{\Psi(R_e)} > \chi_0, \chi_0 = 2.5$) and less compact regions with 'holes' (denoted by the ratio between the region area, ($A(R_e)$), and filled area, ($F(R_e)$), $\frac{A(R_e)}{F(R_e)} < \eta_0, \eta_0 = 0.95$) are discarded as shown in (4.4). ρ is calculated as the maximum major axis length among all the bright candidate regions in (4.5).

$$I_v = \{[I - LPF(I)] < 0\} \tag{4.1}$$

$$I_b = \{[scale(I_r + histeq(I))] \rightarrow [0,1] > 0.9\} \tag{4.2}$$

$$R_e = Overlap(I_v, I_b, \nu), e \ \in \{1, 2, ...r\} \tag{4.3}$$

$$\text{Such that}, \forall e, \ \frac{\Phi(R_e)}{\Psi(R_e)} \leq \chi_0, \frac{A(R_e)}{F(R_e)} \geq \eta_0. \tag{4.4}$$

$$\rho = max_e \Phi(R_e). \tag{4.5}$$

From all the bright candidate regions (R), the brightest candidate region for the OD

is selected based on two parameters: vessel-sum and solidity using (4.6). For computing the vessel-sum, at each bright candidate region (R_e), a circular mask is generated whose center is at the centroid of R_e with radius ρ. Next, the sum of pixel intensities of all the vessel pixels in I_v lying within each such circular mask is computed as vessel-sum by a function $Vessel\text{-}Sum(R_e)$. Solidity of a bright candidate region is a measure of the compactness of shape, and it is computed as the ratio of the area to the area within a convex hull bordering the region ($Solidity(R_e) = \frac{A(R_e)}{A(H(R_e))}$) [10]. Now, the brightest OD region must be the bright candidate region with Maximum Vessel-Sum and Solidity *(MaxVeSS*. If the region with maximum vessel-sum is not same as the region with maximum solidity ($e_1 \neq e_2$), then the region with maximum vessel-sum is discarded ($R = R \backslash R_{e_1}$), and (4.6) is re-evaluated for the remaining regions till convergence is achieved in (4.6).

$$\Lambda(R) = [e_1, e_2 : e_1 = \arg\max_e Vessel\text{-}Sum(R_e), \quad e_2 = \arg\max_e Solidity(R_e)]. \tag{4.6}$$

$$R_{OD}(\Lambda(R)) = \begin{cases} R_{e_1} = R_{e_2} & : e_1 = e_2 \\ R_{OD}(\Lambda(R = R \backslash R_{e_1})) & : e_1 \neq e_2. \end{cases} \tag{4.7}$$

Once the OD candidate region is detected as R_{OD}, the centroid of this region is detected as $\Theta(R_{OD})$, and the OD neighborhood region is detected as a circular region centered at $\Theta(R_{OD})$ with radius ρ. This OD neighborhood is denoted by a sub-image mask $S^{R_{OD}}$.

The *MaxVeSS* algorithm detects the OD candidate region, the OD neighborhood and also the major blood vessels as shown in Fig. 4.2. The exact OD boundary and VO is then estimated using these segmented retinal components. It is noteworthy that for some existing DR screening tools such as the one in [3], exact OD boundary detection is not required since detection and masking out of the OD neighborhood removes instances of false positives for bright lesion detection. Hence, the *MaxVeSS* algorithm can be a useful module for such screening tools, especially for images with varying FOVs.

OD Boundary Detection

Once the OD neighborhood and the brightest OD candidate region are detected, the next task is to detect the exact OD boundary. The morphologically reconstructed image I_r is masked with the OD neighborhood mask ($S^{R_{OD}}$) and thresholded, using threshold parameter ω, to obtain an image containing bright regions. ω is computed using Otsu's threshold method from the superimposed image $[I_r \circ S^{R_{OD}}]$. The bright regions are then further subjected to region-based thresholding, where the bright regions that are highly elliptical, or that have holes in them, or that have a significantly small area, are discarded. The remaining bright regions are contained in image T, as defined in (4.8).

$$\begin{aligned} T = \left\{ I_r \circ S^{R_{OD}} \right\} > \omega, : T = [R_k, k = 1, ...n_k], \\ \text{such that}, \forall k, \ \frac{\Phi(R_k)}{\Psi(R_k)} \leq \chi, \frac{A(R_k)}{F(R_k)} \geq \eta, A(R_k) \geq 30. \end{aligned} \tag{4.8}$$

From all the retained bright regions in image T, the location of the OD candidate region is detected as the region containing the pixel $\Theta(R_{OD})$ (i.e., $\Theta(R_{OD}) \in R_{OD} \subseteq T$). Next, the bright regions in T that lie within one disc-diameter from R_{OD} are detected as the probable OD regions (P). Thus, the bright regions in T whose centroids are located within δ pixels from $\Theta(R_{OD})$ are included in image P in (4.9). A convex hull (H) is then constructed around all the regions in P (4.10). Next, the centroid ($\Theta(H)$), the major axis length ($\Phi(H)$) and minor axis length ($\Psi(H)$) of the convex hull H are computed and an ellipse is fitted corresponding to these measurements. This best fit ellipse is resized to the original image dimensions this is the segmented OD boundary ($\hat{D}$) in (4.11).

$$\forall \ T = [R_k | k = (1, ...n_k])], \ R_{OD}, \text{ identify } P \subseteq T, \tag{4.9}$$

$$P = [R_{OD} \cup R_l : ||\Theta(R_l) - \Theta(R_{OD})||_2 \leq \delta], l \leq n_k.$$

$$H \leftarrow \textbf{Convex Hull } (\mathbf{P}). \tag{4.10}$$

$$\hat{D} \leftarrow \text{Ellipse with } [\Phi(H), \ \Psi(H), \ \Theta(H)]. \tag{4.11}$$

The threshold parameters for OD boundary detection are empirically determined. To determine the thresholds for images with $45 - 55^o$ FOV, 5 images from the DIARETDB0 data set were selected such that each image had significant bright lesions, poor illumination or laser scar marks. On analyzing the compactness measures for the OD regions and the scar or bright lesion regions on these 5 images, the threshold values [χ, η, δ] were estimated for all the images from DRIVE, DIARETDB1, DIARETDB0, and MESSIDOR data set as [4.4, 0.97, 54]. For the CHASE_DB1 images with 30^o FOV, these threshold values were empirically determined using the first two images from the left and right eye of the first patient as [3.4, 0.95, 60], respectively. The steps for detecting bright regions within the OD neighborhood mask around the OD candidate region and segmentation of the OD boundary are illustrated in Fig. 4.3.

Vessel Origin detection

Once the OD boundary is segmented, the next task is to detect the position from which the optic nerve originates, or the pixel location of the VO. For this, a binary image mask corresponding to the segmented OD boundary ($S^{R_{OD}}$) is superimposed on the major blood vessel image (I_v). The VO pixel ($\hat{O}$) is located at the centroid of the vessels in the resulting superimposed image. The steps to VO location detection are illustrated in Fig. 4.4.

4.4 Results

4.4.1 Metrics

The robustness of the proposed method for OD boundary segmentation and VO pixel detection is analyzed based on distribution of certain performance metrics. These performance metrics are described in terms of the area of overlap between the manually segmented actual OD (D) and the automated segmented OD ($\hat{D}$), and the distance in pixels between the segmented and manual ODs and VOs as shown in Fig. 4.5. For each test image, the area of the manually marked OD also detected by the automated algorithm (TP, true positive), area of the falsely detected OD by the automated algorithm (FP, false positive), area of the actual OD missed by the automated segmentation (FN,

false negative), and area within the retinal region that is not the OD (TN, true negative) are computed. The performance metrics to analyze the robustness of the proposed OD segmentation algorithm are described as follows.

- S (Overlap Score) - It denotes the fraction of overlapping area between the actual and segmented OD, i.e., $S = \frac{A\{D \cap \hat{D}\}}{A\{D \cup \hat{D}\}}$. Higher S denotes better automated segmentation.

- M (Mean absolute OD distance) - It denotes the mean shortest distance in pixels between the circumference of the segmented and actual OD. To compute M, sample points are detected on the circumference of the segmented and actual disc every 3^o ranging from [0 to 360^o]. Let the sampled points on the actual OD be $[X_1, ...X_{n_D}]$, while the points on the segmented OD be $[Y_1, ...Y_{n_{\hat{D}}}]$, where $n_D = n_{\hat{D}} = 120$. The shortest distance of each sampled point on the actual disc from the sampled points on the segmented disc is computed using (12). Finally, the mean of these distances is computed using (13). Smaller M denotes better segmentation.

- SEN (Sensitivity) - It denotes the fraction of the actual OD area detected by the automated algorithm. Higher SEN denotes better segmentation.

- FPR (False Positive Rate) - It denotes the fraction of falsely detected OD area. Lower FPR denotes better segmentation.

- Acc (Accuracy) - It denotes the fraction of correctly identified pixels to the total number of pixels in the retinal region, i.e., $Acc = \frac{TP+TN}{TP+TN+FP+FN}$. Higher Acc denotes better segmentation.

- Δ (VO error) - It denotes the Euclidean distance in pixels between the manually marked VO (O) and the detected VO ($\hat{O}$). Smaller Δ denotes better segmentation.

- Time- It denotes the average OD boundary segmentation and VO detection time per image for the particular data set measured in seconds. The average processing time is inversely proportional to the computational complexity of an automated segmentation algorithm.

- Success (%) - It represents the percentage of images in a particular data set where the OD is successfully identified. Successful OD identification occurs when the automatically detected VO ($\hat{O}$) lies within the boundary of the manually segmented disc (D).

$$\forall\ [X_{i'} \in D : i' = 1, ...n_D],\ [Y_{j'} \in \hat{D} : j' = 1, ...n_{\hat{D}}], \tag{4.12}$$

$$m_{D,\hat{D}}(i') = \min_{j'} ||X_{i'} - Y_{j'}||_2,$$

$$m_{\hat{D},D}(j') = \min_{i'} ||Y_{j'} - X_{i'}||_2,$$

$$M = \frac{1}{2}\left\{ \frac{1}{n_D}\sum_{i'}^{n_D} m_{D,\hat{D}}(i') + \frac{1}{n_{\hat{D}}}\sum_{j'}^{n_{\hat{D}}} m_{\hat{D},D}(j') \right\}. \tag{4.13}$$

The overlap score metric estimates the fractional area common to the actual and segmented OD, while the mean absolute OD distance represents the closeness of fit between the actual and segmented OD boundaries. The importance of analyzing both these metrics together is illustrated using two examples in Fig. 4.6. In both these examples, S metric is same, while the M metric varies. In such a case, the instance with a lower M value represents a better segmented OD, since it enables better estimation of blood vessel-based fiduciary points within the OD region.

The performance metrics for the OD segmentation algorithm are analyzed in terms of the mean and standard deviation of the particular metrics across all images in each data set under analysis, and the distribution of the overlap score, the mean absolute distance, and the pixel error in the VO location. These performance metrics are analyzed with respect to existing OD segmentation algorithms to assess the comparative robustness of the proposed method.

4.4.2 Segmentation Performance

The OD mean and standard deviation of the OD segmentation performance metrics using the proposed algorithm is shown in Table 4.2. While the OD boundary segmentation analysis is performed on all 1200 images from the MESSIDOR data set, the VO location is detected in 500 images that were manually annotated for this work. Hence,

the mean pixel error for VO location detection (Δ) is evaluated on 500 images in the MESSIDOR data set, and this change in the number of images under analysis is denoted by the symbol + in Table 4.2.

We observe that the proposed algorithm has better averaged segmentation metrics across all test images when compared to another recent algorithm in Morales et. al. [57]. Additionally, from Table 4.2, we observe that the proposed algorithm achieves mean $\Delta = 7.36$ in about 4.36 seconds per image. Also, the proposed OD segmentation algorithm has a significantly low false positive region identification rate, thereby resulting in more accurate OD boundaries and better fiduciary point estimation within the OD region.

Next, the comparative performance of the proposed OD boundary segmentation algorithm with existing works is shown in Table 4.3. Here, we observe that for the DRIVE data set, the proposed method has the best OD boundary segmentation metrics so far. The proposed algorithm achieves significantly lower standard deviation for M and 100% OD segmentation success when compared to all other methods. This demonstrates the robustness of the proposed algorithm to retinal variability due to pathology.

For the DIARETDB1 data set, we observe that the proposed method is out-performed only by the stochastic watershed transform-based method in Morales et. al. [57]. However, the $[FPF, Acc]$ achieved by the proposed method and the Morales et. al. [57] method are $[0.0017, 0.9963]$ and $[0.0028, 0.9957]$, respectively. Thus, the proposed method maintains a low false positive region detection rate in the test images from the DIARETDB1 data set. For the MESSIDOR data set, only the method relying on the Circular-Hough transform in Aquino et. al. [42] outperforms the proposed method in terms of the overlap score S. This variation in S is mostly due to the difference in manual markings and the variation introduced by down-sampling each image to [500x500] followed by image resizing at the end of OD boundary detection. However, the average OD boundary segmentation time taken by the method in Aquino et. al. [42] and the proposed method are 5.69 seconds and less than 4.47 seconds, respectively. Hence, the image resizing operation is beneficial from the computational complexity standpoint.

Next, in Table 4.4, we analyze the comparative performance of the proposed method for detecting the VO pixel. Here, we observe that the proposed algorithm achieves the lowest VO detection error in terms of Δ in the least computational time, and a

‡ Mean and standard deviation computed for 500 manually marked images.

consistent OD segmentation success rate of 100% over all the test data sets. We point out that the use of a circular structuring element, instead of linear, in the morphological transformation step led to an improvement of 8% and 5% in the overlap score (S), reduction of 2.25 and 1.25 pixels in mean distance (M), and error reduction of 1.22 and 1.9 pixels in VO location for DRIVE and DIARETDB1 databases, respectively.

Examples of the best and worst OD segmentation performance obtained using the proposed algorithm on the images from all the 5 public data sets are shown in Fig. 4.7. We observe from the worst automated segmentation instances that the proposed algorithm has significant OD segmentation accuracy in retinal images with improper illumination and pathology. The images with least automated segmentation accuracy from MESSIDOR data set have blurred OD boundary due to prominent peripapillary atrophy. The proposed method is successful in detecting the OD neighborhood region in these images, but the exact automated OD boundary detection for such images is challenging. Further, in Fig. 4.8, we observe that the proposed algorithm is robust to fundus images with retinal abnormalities around the OD region, such as images with myelination and peripapillary atrophy with relatively low severity.

4.4.3 Distribution of Performance metrics

The overlap score between manually annotated disc and the segmented disc is regarded as a significant indicator of OD segmentation accuracy [42] [52]. Analysis of the S metric distribution on the test data sets is shown in Table 4.5. We observe that for all the test data sets, the proposed method has the highest percentage of image with $S \geq 0.7$. For the DRIVE data set, the distribution of the S metric is significantly better than the methods in Salazar et. al. [51]. For the MESSIDOR dataset, the method in Aquino et. al. [42] has better performance for $S > 0.75$. However, the proposed algorithm demonstrates consistent performance on this data set with 96% images having $S \geq 0.7$.

Additionally, the fit between the segmented and actual OD boundary has been extensively used to demonstrate the performance of OD segmentation algorithms in [48] [41]. The MESSIDOR data set contains 400 images from three data subsets named: CHU de St Etienne, LaTIM-CHU de BREST, and Lariboisiere and thus, it represents a wide variety of images with varying severities of pathologies, the distribution of the M metric has been analyzed on this data set in existing works [48] [42]. For comparative

analysis of the OD boundary segmentation performance, the distributions of the M metric for the images from the MESSIDOR data set are shown in Table 4.6. Based on the M metric, and assuming the average OD radius to be 70 pixels for the images from the MESSIDOR data set [41], four categories of OD boundary segmentation can be defined as: Excellent ($M \leq 3.5$), Good ($M \leq 7$), Fair ($M \leq \frac{70}{3}$), and Poor ($M > \frac{70}{3}$) [48]. From Table 4.6, we observe that the proposed algorithm has more images in the Excellent, Good and Fair segmentation category than the existing methods.

Finally, the distributions of the M metric and Δ metric on all the test data sets are shown in Fig. 4.9. Since low values of both these metrics indicate good OD segmentation accuracy, hence the percentage of images in each data set that have $[M \leq \text{mean}(M)]$ and $[\Delta \leq \text{mean}(\Delta)]$ are shown in Table 4.7. Here, we observe that for all the data sets, more than 53% of the images have small Δ values, and more than 55% images have low M metric. The average OD radius for all the images from the DRIVE, DIARETDB1, DIARETDB0 and MESSIDOR data sets has been estimated as 60-70 pixels in [52], [48], while for the CHASE_DB1 data set, the average OD radius is measured to be 90 pixels. From Fig. 4.9, we observe that the proposed segmentation method achieves Δ consistently less than 35 pixels for all test images, thereby ensuring 100% success of OD segmentation.

4.5 Conclusions and Discussion

In this chapter, we have proposed a rule-based OD segmentation algorithm that is robust to fundus images with varying FOV, illuminations and pathologies. Since the complete OD region is not equally brightly illuminated, portions of the complete OD are detected in two steps. In the first step, the brightest and most compact OD candidate region is detected at the intersection of the bright regions and the retinal vasculature. Also, the OD neighborhood is detected in this step. In the second step, additional bright OD regions within the OD neighborhood are detected based on two compactness parameters, which are, the ratio of area and convex area and ratio of the area to the filled area. A convex hull is then estimated around all the bright candidate OD regions and a best fit ellipse corresponding to the centroid, major and minor axis lengths of this convex hull is estimated as the segmented OD boundary. The centroid of the major blood vessels

within detected OD boundary is the VO location. The proposed algorithm is the fastest segmentation method reported so far and it results in consistent OD boundary segmentation and VO location detection across normal and pathological retinal images. The OD boundary segmentation performance of the proposed algorithm has lower standard deviation in the error between manually segmented and automatically estimated OD boundary when compared to recent works in [57]. The high computational speed can be attributed to the down sampling all the fundus images to [500x500] followed by up sampling to original image dimensions at the end of the OD boundary detection step. Although this down and up sampling method introduces some errors in the segmented OD boundary, these errors are significantly small when compared to the computational speed thus achieved.

In this chapter the compactness of the bright OD regions is determined by two metrics. The first metric is the ratio of the area and convex area for a bright region. A high value for this metric denotes compact OD region boundaries when compared to bright lesions such as hard exudates that contain irregular edges and have a low value for this metric. The other compactness metric is the ratio of area to the filled area, such that a bright OD region would have a high value for this metric, while regions with 'holes' in them would have a lower value. This metric further eliminates bright lesion regions. These two compactness metrics are more effective for automated OD region segmentation when compared to the metrics defined in prior works, such as the ratio of squared perimeter to the area of a bright region in [52].

The most important feature of the proposed segmentation algorithm is that it is a rule-based method and generalizable to images with FOV varying from [40^o to 55^o] where the OD is always present in the fundus image. For images with [30^o to 35^o], the OD may not be present in particular angles of the retinal shots. In such cases, if a portion of the OD is visible in the image, an OD boundary is correctly estimated as shown in the first example of Fig. 4.10. However, if the OD is entirely absent in the fundus image, and then a false OD region may be detected by the proposed algorithm as shown in the second and third examples in Fig. 4.10. In such situations, the thickness of the major blood vessels within the segmented OD region can be analyzed to discard these instances of false OD detection. It is known that the blood vessels are thickest at the OD in any retinal image. Hence, as a post-processing step in images with [30^o to

35^o] FOV, the segmented OD region mask is superimposed on the blood vessel image followed by image erosion using linear structural element of size 7-15 pixels at 0 degree and 90 degree orientations. If OD exists in a particular image, then the thickness of the small eroded regions should be greater than 10-15 pixels. Otherwise, the OD boundary is discarded to eliminate falsely segmented OD regions. Future work will be directed towards accurate blood vessel thickness estimation at the OD region for detecting neovascularization at the optic disc and hypertensive retinopathy.

The other important feature of the proposed algorithm is that it robustly detects the OD boundary and VO in retinal images with additional abnormalities around the OD region. For instance in images with myelinated nerve fiber and peripapillary atrophy, existing methods [48] have resulted in poor segmentation performance while the proposed algorithm has fair to good OD segmentation performance on such images. Future work will be directed towards combining the proposed algorithm with automated glaucoma detection algorithms that measure the variations in cup-to-disc ratio to detect the disease severity.

Table 4.1: Definition of Notation.

Notation	Meaning
I	Pre-processed green plane of the fundus image.
I_r	Morphological reconstruction of the green plane image.
I_v	Blood vessel image obtained by high-pass filtering and thresholding I.
I_b	Bright region image obtained by thresholding I_r.
$Overlap$ (I_v, I_b, ν)	Function that retains regions in I_b that are closer to the regions in I_v than ν pixels.
$\Phi(R_e)$	Major axis length of a region R with index number 'e'.
$\Psi(R_e)$	Minor axis length of a region R with index number 'e'.
$A(R_e)$	Area of a region R with index number 'e'.
$F(R_e)$	Area after holes in region R with index number 'e' are filled.
ρ	Maximum major axis length among all bright candidate regions.
$Solidity(R_e)$	Function computing the ratio of the area and convex area for a particular region R with index number 'e'.
$Vessel\text{-}Sum$ (R_e, ρ)	Function computing the sum of vessel pixels from image I_v within a circular masked region generated at the centroid of region R_e with radius ρ.
$\Theta(R_e)$	Centroid pixel of a region R_e.
R_{OD}	OD candidate region that has the highest solidity and highest vessel sum in its neighborhood.
$S^{R_{OD}}$	OD neighborhood mask generated around region R_{OD}.
T	Thresholded image from $I_r \circ S^{R_{OD}}$.
P	Image obtained by retaining the bright regions in T that are less than 'δ' pixels away from the region R_{OD}.
H	Convex hull containing the all regions in the image.
$\hat{D}$	Best fit ellipse around H.
$\hat{O}$	Segmented VO pixel.

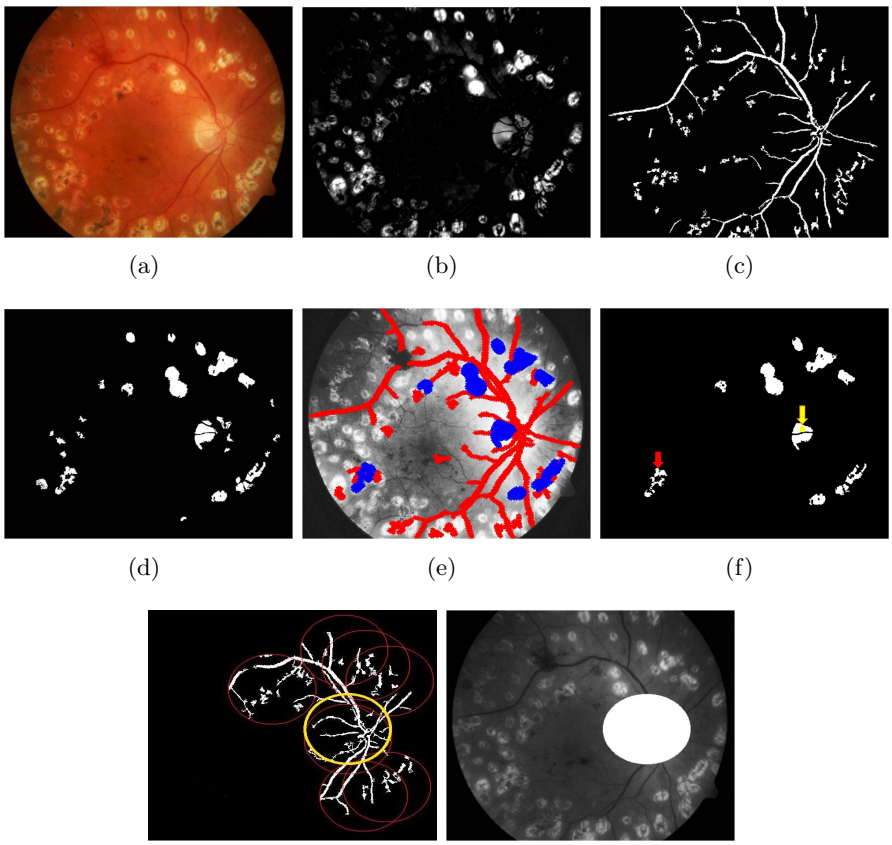

Figure 4.2: Steps involved in extracting the brightest OD sub-region and the OD neighborhood. (a) Original image from DIARETDB0. (b) Morphologically reconstructed image I_r. (c) Major vessels extracted as I_v. (d) Bright regions extracted in image I_b. (e) Intersecting bright candidate regions (R in blue) and the vessel regions (red). (f) Solidity of regions in R is computed. The region depicted by red arrow is discarded since that region has 'holes' in it, i.e., $\frac{A(R_e)}{F(R_e)} < \eta_0$. The region depicted by yellow arrow has the maximum solidity. (g) Circular discs estimate vessel-sum within them for each region in R. The region with yellow boundary has the maximum vessel-sum. (h) OD neighborhood detected ($S^{R_{OD}}$).

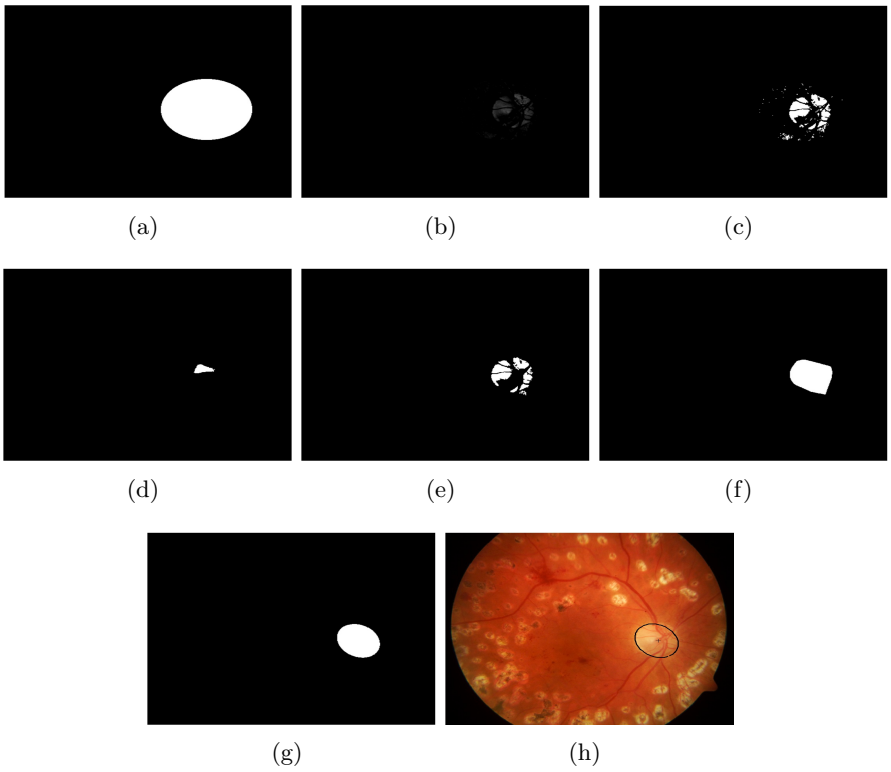

Figure 4.3: The OD boundary segmentation steps for an image from DIARETDB0 data set. (a) OD neighborhood mask ($S^{R_{OD}}$). (b) Superimposed image $I_r \circ S^{R_{OD}}$. (c) Bright regions detected in image T after thresholding image (b). (d) The OD candidate region (R_{OD}) is located among the bright regions in T. (e) Bright regions in T that are close to the R_{OD} are retained as image P. (f) Convex hull (H) constructed around all regions in image (e). (g) Best fit ellipse to the convex hull. (h) The segmented OD boundary ($\hat{D}$).

Table 4.2: Mean performance metrics and their standard deviation () of the Proposed Method on the test data sets.[‡]

Data	S	M	SEN	FPR	Acc	Δ	Time
DRIVE	0.8165 (0.097)	4.87 (3.49)	0.8967 (0.077)	0.0021 (0.0023)	0.9959 (0.0043)	9.16 (4.21)	4.71 (3.21)
DIARETDB1	0.8060 (0.074)	4.15 (1.59)	0.8855 (0.057)	0.0017 (0.001)	0.9963 (0.001)	6.80 (3.56)	3.84 (1.69)
DIARETDB0	0.7774 (0.093)	4.91 (2.44)	0.8660 (0.068)	0.0021 (0.001)	0.9956 (0.002)	7.53 (4.76)	3.79 (0.87)
CHASE_DB1	0.8077 (0.075)	5.19 (2.03)	0.8962 (0.047)	0.0032 (0.001)	0.9941 (0.002)	8.09 (4.34)	3.63 (0.35)
MESSIDOR	0.8331 (0.075)	3.39 (1.58)	0.9143 (0.072)	0.0015 (0.0008)	0.9979 (0.001)	7.31 (4.19)[‡]	4.47 (2.00)[‡]

(a) (b) (c)

Figure 4.4: The VO pixel location steps. (a) Superimposed image $S^{R_{OD}} \circ I_v$. (b) The centroid pixel denoted by red arrow. (c) The VO pixel located.

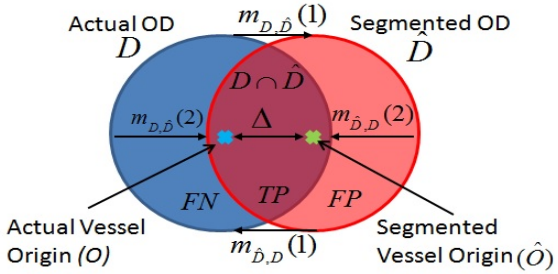

Figure 4.5: The metrics used to evaluate the performance of automated OD segmentation.

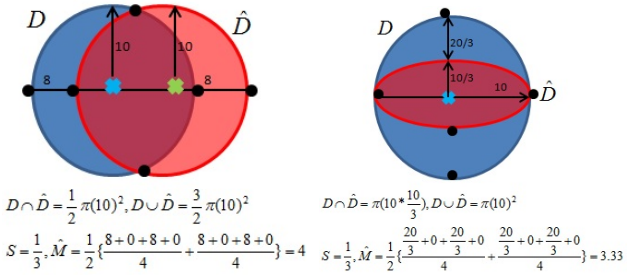

(a) (b)

Figure 4.6: Examples of automated OD segmentation performance. In both cases $S = \frac{1}{3}$. $\hat{M}$ is estimated using 4 sample points on the actual and OD boundaries denoted by the solid black dots. (a) has higher $\hat{M}$ than (b), hence (b) is a better segmentation.

Table 4.3: Comparative Performance of OD Boundary Segmentation with existing works.

Method	S	M	SEN	Success (%)
DRIVE				
Soparaphak et. al.[63]	0.179 (0.06)	20.94 (15.6)	0.80	98.61
Walter et. al.[64]	0.300 (0.13)	12.39 (8.3)	-	77.5
Seo et. al.[65]	0.316 (0.09)	11.19 (4.1)	-	95
Kande et. al.[66]	0.287 (0.08)	17.42 (8.1)	-	95
Stapor at. al.[67]	0.325 (0.15)	9.85 (6.0)	-	87.5
Lapuscu et. al.[68]	0.403 (0.08)	8.05 (7.6)	-	95
Welfer et. al.[52]	0.415 (0.08)	5.74	-	100
Zeng et. al.[69]	0.559	10.24	0.65	85
Boykov et. al.[70]	0.553	9.97	0.74	95
Salazar et. al.[51]	0.707	6.68	0.84	97.5
Morales et. al.[57]	0.716 (0.17)	5.85 (10.2)	0.854	100
Proposed	**0.816 (0.09)**	**4.87 (3.5)**	**0.9**	**100**
DIARETDB1				
Soparaphak et. al.[63]	0.298 (0.09)	16.31 (5.3)	0.80	93.70
Walter et. al.[64]	0.372 (0.11)	15.52 (5.3)	-	92.13
Seo et. al.[65]	0.353 (0.07)	9.74 (4.6)	-	80.89
Kande et. al.[66]	0.332 (0.05)	8.35 (3.2)	-	88.76
Stapor at. al.[67]	0.341 (0.09)	6.02 (5.6)	-	78.65
Lapuscu et. al.[68]	0.309 (0.13)	13.81 (9.1)	-	86.51
Welfer et. al.[52]	0.434 (0.11)	8.31 (4.1)	-	97.7
Zeng et. al.[69]	0.384	17.49	0.55	75.28
Boykov et. al.[70]	0.540	10.74	0.76	85.4
Salazar et. al.[51]	0.757	6.38	0.86	96.7
Morales et. al.[57]	0.817 (0.13)	2.88 (3.0)	0.922	100
Proposed	**0.806 (0.07)**	**4.15 (1.6)**	**0.89**	**100**
MESSIDOR				
Yu et. al.[48]	0.83	7.7	-	98.3
Aquino et. al.[42]	0.86	-	-	100
Morales et. al.[57]	0.823 (0.14)	4.07 (6.1)	0.93	100
Proposed	**0.833 (0.07)**	**3.39 (1.6)**	**0.91**	**100**

Table 4.4: Comparative Performance of VO detection with existing works.

Method	Δ	Success (%)
DRIVE		
Soparaphak et. al.[63]	16.98	98.61
Yu et. al.[71]	-	97.5
Lalonde et. al.[47]	13.21	97.22
Ravishankar et. al.[72]	14.67	86.10
Qureshi et. al.[41]	15.95	100
Niemeijer et. al.[73]	20.69	67.35
Rangayyan et. al.[50]	23.2	100
Dehghani et. al.[74]	15.9	100
Proposed	**9.16**	**100**
DIARETDB1		
Soparaphak et. al.[63]	13.05	93.70
Yu et. al.[71]	-	98.9
Lalonde et. al.[47]	20.84	75.46
Ravishankar et. al.[72]	11.95	76.41
Qureshi et. al.[41]	11.95	94.02
Niemeijer et. al.[73]	20.41	77.04
Youssif et. al.[75]	17	100
Proposed	**6.80**	**100**
DIARETDB0		
Soparaphak et. al.[63]	11.89	95.29
Yu et. al.[71]	-	99.2
Lalonde et. al.[47]	20.63	77.56
Ravishankar et. al.[72]	11.41	80.12
Qureshi et. al.[41]	12.23	96.79
Niemeijer et. al.[73]	18.55	78.20
Proposed	**7.53**	**100**

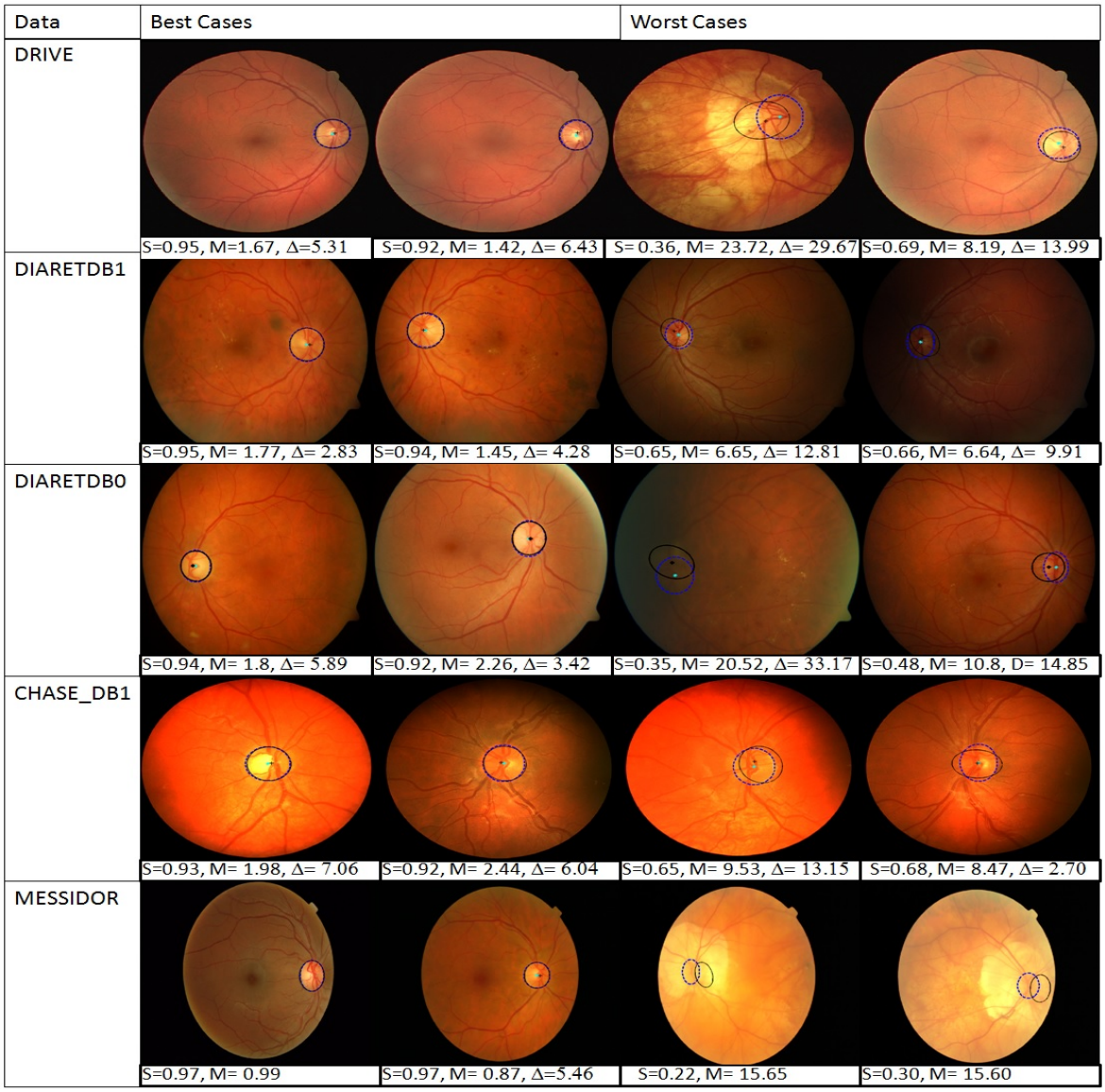

Figure 4.7: Best and worst OD segmentation performances achieved using the proposed algorithm. The first two columns demonstrate the best OD segmentation cases. Third and fourth columns demonstrate the worst OD segmentation cases. The dotted blue outline represents the manually annotated OD (D) while the solid black circle represents the automatically segmented OD ($\hat{D}$). The cyan (*) represents the manually marked VO (O), while the black (*) represents the automated VO detected ($\hat{O}$). For all the worst case performances, the automated VO lies within the manually marked OD boundary, thereby showing that the proposed OD segmentation algorithm has 100% ACC on all the 5 public data sets.

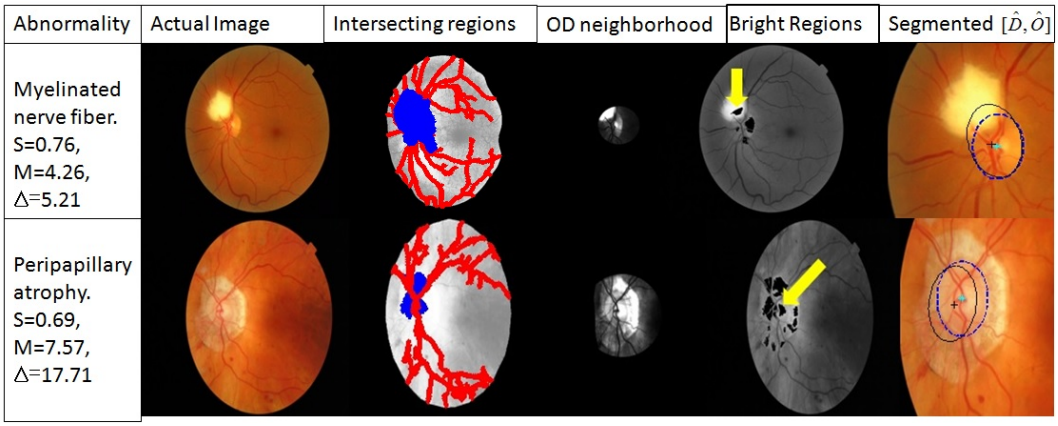

Figure 4.8: Examples of automated OD segmentation on images, taken from the MESSIDOR data set, with abnormalities around the OD regions. First column shows the original image. Second column shows the reddest and bright region overlapping using the *MaxVeSS* algorithm. Third column shows the OD neighborhood mask superimposed on the green plane image I. Fourth column shows the bright regions (T) in black superimposed on the image I. The brightest OD candidate region (R_{OD}) is indicated by the arrow. The fifth column shows the final best-fit ellipse detected (solid black line) and VO detected (black *) compared to the manually segmented OD boundary (dotted blue line) and manual VO (cyan *).

Table 4.5: Percentage of images in particular overlapping intervals.

Method	$S \geq 0.9$	$S \geq 0.85$	$S \geq 0.75$	$S \geq 0.7$
DRIVE				
Zheng et. al.[69]	2.5	7.5	17.5	20
Boykov et. al.[70]	0	0	12.5	27.5
Salazar et. al.[51]	5	25	50	57.5
Proposed	**17.5**	**40**	**85**	**95**
DIARETDB1				
Zheng et. al.[69]	1.12	2.25	5.62	10.11
Boykov et. al.[70]	2.25	8.99	28.09	38.2
Salazar et. al.[51]	11.24	32.58	60.67	70.78
Proposed	**10.11**	**31.46**	**73.03**	**91.01**
DIARETDB0				
Proposed	**5.38**	**22.5**	**68.34**	**82.5**
CHASE_DB1				
Proposed	**10.71**	**39.29**	**82.14**	**89.28**
MESSIDOR				
Aquino et. al.[42]	46	73	90	93
Yu et. al.[48]	25	45	77	77
Proposed	**19.33**	**46.83**	**85.25**	**96**

Table 4.6: Percentage of images in particular 'M' intervals for the MESSIDOR data sub-sets: CHU de St Etienne, LaTIM-CHU de BREST, and Lariboisiere.

	Excellent	Good	Fair	
Method	M$\leq$ 3.5	M$\leq$ 7	M$\leq$ 14	M$\leq \frac{70}{3}$
CHU de St Etienne				
Yu et. al.[48]	29	64	89	98
Proposed	**59.25**	**97.75**	**99.25**	**100**
LaTIM-CHU de BREST				
Yu et. al.[48]	33	64	87	96
Proposed	**59**	**99.25**	**100**	**100**
Lariboisiere				
Yu et. al.[48]	34	71	90	98
Proposed	**57.25**	**98.5**	**100**	**100**
All				
Yu et. al.[48]	32	66	89	97
Aquino et. al.[42]	40	79	97	97
Proposed	**58.5**	**98.5**	**99.75**	**100**

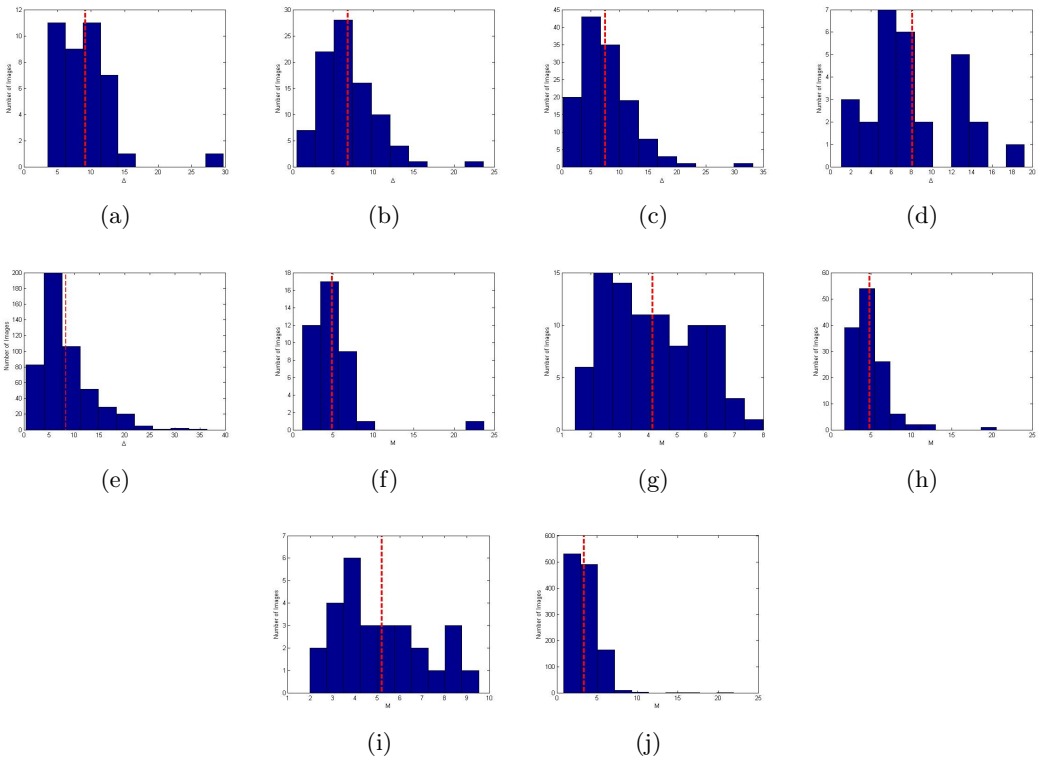

Figure 4.9: Histograms showing the distribution of Δ and M in the data sets. The red line indicates the mean values (mean (Δ), mean(M)). The distribution of Δ is shown in (a) DRIVE (b) DIARETDB1 (c) DIARETDB0 (d) CHASE_DB1 (e) MESSIDOR (500 manually annotated images). The distribution of M is shown in (f) DRIVE (g) DIARETDB1 (h) DIARETDB0 (i) CHASE_DB1 (j) MESSIDOR.

Table 4.7: Percentage of images where [$\Delta \leq$ mean(Δ)] and [$M \leq$ mean(M)].

Data Set	$\Delta \leq$ mean(Δ) (%)	$M \leq$ mean(M) (%)
DRIVE	57.5	57.5
DIARETDB1	53.94	57.30
DIARETDB0	60	55.83
CHASE_DB1	53.57	60.71
MESSIDOR	63.8	63.4

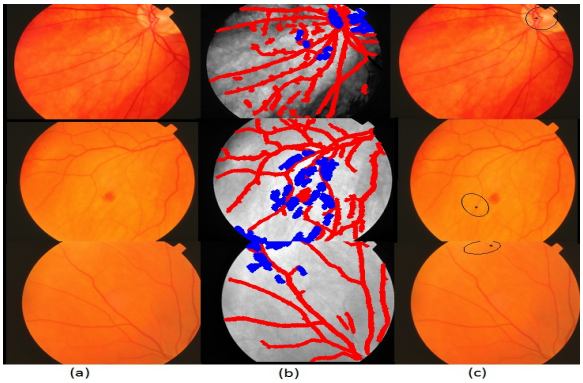

Figure 4.10: Examples of images with 30^o FOV that require post-processing to eliminate false OD detection. (a) Original image. (b) Intersecting blood vessel (red) and bright (blue) regions detected. (c) Automated OD boundary and VO detected. Analysis of the thickness of the blood vessels within the segmented OD region can be used as a post-processing step to eliminate such false detections.

Chapter 5

Automated Non-Proliferative Diabetic Retinopathy Detection

5.1 Introduction

According to a study by the American Diabetes Association, diabetic retinopathy (DR) had affected more than 4.4 million Americans of age 40 and older during 2005-2008, with almost 0.7 million (4.4% of those with diabetes) having advanced DR that could lead to severe vision loss [76]. Early detection and treatment of DR can provably decrease the risk of severe vision loss by over 90% [77]. Thus, there is a high consensus for the need of efficient and cost-effective DR screening systems [4]. Unfortunately almost 50% of diabetic patients in the United States currently do not undergo any form of documented screening exams in spite of the guidelines established by the American Diabetes Association (ADA) and the American Academy of Ophthalmology (AAO) [4]. Statistics show that 60% of the patients requiring laser surgery to prevent blindness do not receive treatment [77]. The major reasons for this screening and treatment gap include insufficient referrals, economic hindrances and insufficient access to proper eye care. Telemedicine, with distributed remote retinal fundus imaging and grading at either local primary care offices or centralized grading remotely by eye care specialists, has increased access to screening and follow-up necessary treatment [78].

Computer-aided screening systems have recently gained importance for increasing

the feasibility of DR screening, and several algorithms have been developed for automated detection of lesions such as exudates, hemorrhages and micro-aneurysms. However, micro-aneurysms are considered to be the primary indicators of DR, and among the noteworthy prior works that aimed at detecting DR, in [46], color normalization and contrast enhancement was applied in the pre-processing steps on fundus images followed by fuzzy C-means clustering for image segmentation, and classification of candidate regions into bright lesions and non-lesions. In [79], micro-aneurysms were detected using template matching in wavelet sub-bands followed by thresholding. Another approach to detect micro-aneurysms based on multi-scale correlation filtering and dynamic thresholding was also developed in [80]. Another method based on extraction of AM-FM features of fundus images, followed by dimensionality reduction and hierarchical clustering, and the use of partial least square method to assign DR severity grade has been presented in [81].

The novel contribution of this chapter is a fully automated, fast and accurate DR detection and grading system that can be used for automated screening for DR and treatment prioritization. So far an automated DR screening system, Medalytix [82], has been used for screening normal patients without DR from abnormal patients with DR on a local data set, with sensitivity in the range 97.4-99.3% on diabetic patients in Scotland. The screening outcome combined with manual analysis of the images that are classified as abnormal by the automated system has shown to reduce the clinical workload by more than 25% in Scotland [82]. Another automated DR screening system grades images from a local data set for unacceptable quality, referable, non-referable DR with sensitivity 84% and specificity 64% [4] [83]. Both these automated systems motivate the need for a fast and more accurate DR screening and prioritization system. The proposed DR detection system is capable of detecting lesions and generating a severity grade for non-proliferative DR (NPDR) in under 6 seconds with 100% sensitivity and 53% specificity. Such a system will ensure that no patient with DR is missed for follow-up treatment, and will be critical in prioritizing eye-care delivery measures for patients with highest DR severity.

The design of the proposed DREAM system is novel since it aims at outlining 3 separate DR detection stages, and minimizing the run-time complexity of each stage to ensure a fast detection system. We propose a feature size reduction followed by

selection of lesion classifiers that have low computational complexity, such that the total time to detect retinopathy lesions and to generate a severity grade is less than 6 seconds for a fundus image. Additionally, the proposed system contains an initial image enhancement module in Stage 1 that enhances the contrast and edge sharpness in fundus images so that images are not rejected based on poor image quality. Existing automated DR screening systems such as the VA screening system [83] rejects about 18% of the images, while Medalytix [82] rejects about 5% of the images based on their bad image quality. The proposed system has not rejected any image so far on account of poor image quality and hence, it is more suitable for automated DR screening and prioritization.

This chapter makes two major contributions. The first major contribution is identification of the top 30 features from a set of 78 features for classifying bright and red retinopathy lesions. We implement feature ranking based on the feature weights generated by AdaBoost [84]. We demonstrate how feature reduction reduces computational complexity of lesion classification by 94-97% in terms of mean processing time per image. The second contribution is a novel *two-step hierarchical binary classification* method that rejects false positives in the first step and in the second step, bright lesions are classified as cotton wool spots (CWS) or hard exudates (HE), and red lesions are classified as hemorrhages (HA) and micro-aneurysms (MA), respectively. This hierarchical classification method reduces the time complexity by 18-24% over a parallel classification method that trains separate classifiers for identifying CWS, HE, HA and MA from false positives. While identifying the optimal bright and red lesion classifiers, we analyze a variety of feature based classifiers such as GMM, kNN, SVM, AdaBoost, and combinational classifiers, and select an optimal classifier set that ensures high specificity for bright lesion classification and high sensitivity for red lesion classification, and low computational time complexity. In our case, we found that GMM is a preferred choice of classifier for detecting bright lesions, and kNN is a preferred choice for detecting red lesions.

The algorithms used in Stage 1 for image segmentation, detection of optic disc, blood vasculature and one-step classification of red and bright lesions in Stage 2 for one public data set have been presented in our earlier work [10]. In this chapter, we extend our analysis to construct a complete 3-stage automated system that not only

detects retinopathy lesions, but also generates a DR severity grade for every fundus image. This chapter introduces a novel two-step hierarchical classification method in Stage 2, it analyzes the importance of feature reduction and feature ranking, and it combines the number of lesions in Stage 3 to generate a DR severity measure and tests the performance of the proposed automated DR detection system on another public data set.

The organization of this chapter is as follows. In Section 5.2, the functionalities of each of the three-stages of the proposed DR screening system is mathematically defined. Section 5.3 describes each of the three stages in separate sub sections. Results regarding the performance of lesion classification and DR severity grading, time complexity analysis and comparison of the proposed system with prior works are presented in Section 5.4 followed by concluding remarks and discussion in Section 5.5.

5.2 Method and Materials

The three-stage algorithm to automatically detect and grade the severity of diabetic retinopathy using ophthalmic fundus images is shown in Fig. 5.1. For each fundus image in JPEG format, the green plane (I_{green}) is used for information extraction.

In Stage 1, a minimum-intensity maximum-solidity (MinIMaS) algorithm [10] is invoked to detect the regions corresponding to the optic disc (R_{OD}) and vasculature (R_{vasc}) as the image background from I_{green}. Next, candidate regions corresponding to red lesions (R_{RL}) and bright lesions (R_{BL}) are detected as foreground (R_{fore}). This is mathematically represented below.

$$R_{OD}, R_{vasc}, R_{fore} \subseteq I_{green} \tag{5.1}$$

$$R_{fore} = R_{BL} \cup R_{RL}. \tag{5.2}$$

In Stage 2, classifiers are used in two hierarchical steps. In step 1, candidate lesion regions (R_{BL}, R_{RL}) are classified as true lesions (R_{TBL}, R_{TRL}) and non-lesions (R_{NBL}, R_{NRL}), respectively. In step 2, the true bright lesions are further classified as hard exudates ($\hat{R_{HE}}$) and cotton wool spots ($\hat{R_{CWS}}$), while the true red lesions are classified as micro-aneurysms ($\hat{R_{MA}}$) and hemorrhages ($\hat{R_{HA}}$). This is mathematically

represented in (5.3)-(5.5). The classified regions are compared to manually annotated ground-truth regions ($R_{HE}, R_{CWS}, R_{MA}, R_{HA}$).

$$R_{BL} = R_{TBL} \cup R_{NBL}, R_{RL} = R_{TRL} \cup R_{NRL} \tag{5.3}$$

$$R_{TBL} = \hat{R_{HE}} \cup \hat{R_{CWS}} \tag{5.4}$$

$$R_{TRL} = \hat{R_{MA}} \cup \hat{R_{HA}}. \tag{5.5}$$

In Stage 3, the number of red lesions and bright lesions are counted and combined using a combination function (Ψ) defined in (5.6)-(5.8) to generate a DR severity grade per image (G). An image with $G = 0$ implies no DR, $G = 1$ implies mild DR, $G = 2$ implies moderate DR and $G = 3$ implies severe DR, respectively.

$$HE = |\cup_j \hat{R_{HE}}(j)|, CWS = |\cup_{j'} \hat{R_{CWS}}(j')| \tag{5.6}$$

$$MA = |\cup_m \hat{R_{MA}}(m)|, HA = |\cup_{m'} \hat{R_{HA}}(m')| \tag{5.7}$$

$$\forall\ I, G = \Psi(HE, CWS, MA, HA) \tag{5.8}$$

$$where,\ G = \{0, 1, 2, 3\}. \tag{5.9}$$

5.2.1 Data

We train and test our DR screening system for normal patients and patients with DR using two public datasets that are described as follows.

- DIARETDB1 data set [60] consists of 89 images with 50^o FOV. These 89 images have been separated to two groups: 28 training images and 61 test images, by the authors such that the training and test data sets were independent of one another. All the 89 images are manually annotated for lesions as ground truth ($R_{HE}, R_{CWS}, R_{MA}, R_{HA}$).
- MESSIDOR data set [62] contains 1200 images with 45^o FOV. Each image is manually assigned a DR severity grade.

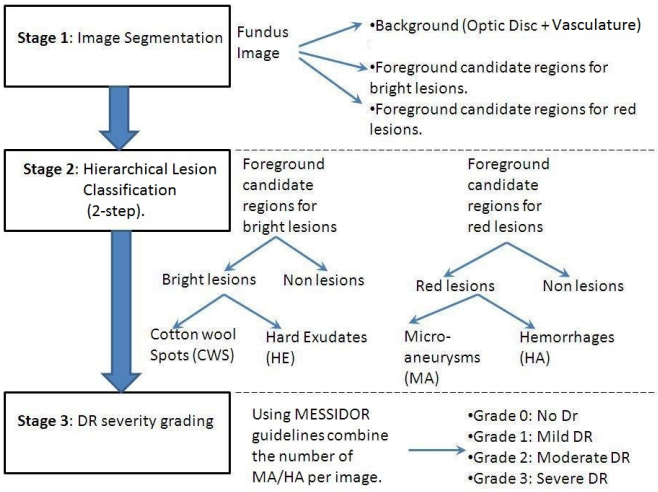

Figure 5.1: The three-stage algorithm for grading DR severity using fundus images. The system flow depicts the functionalities of the three individual stages and their interconnections.

5.2.2 Lesion Classification

Once each fundus image is segmented in stage 1, foreground regions corresponding to bright (R_{BL}) and red (R_{RL}) retinopathy lesions can be detected as candidate objects. However, classification of these candidate lesion objects is imperative to reduce instances of false positives, and to categorize bright lesions as hard exudates or cotton wool spots, and red lesions as hemorrhages or microaneurysms, respectively. Thus, to achieve lesion classification, we extract features corresponding to each candidate object, as explained in Section 5.3.2. Every candidate object can be represented by a feature vector ($\mathbf{x}$) corresponding to the location of the object in the feature space. While training classifiers, the feature vectors of the objects from the training set of images are scaled in [0,1]. If the object is manually annotated as a lesion, then a class label $y = 1$ is assigned to the object. Based on the groundtruth, if the object is not a lesion, then $y = 0$. Object vectors from the test set of images ($\mathbf{x}^*$) are similarly scaled in [0,1], and the class labels determined using groundtruth (y^*) are compared with the class labels, assigned by the classifiers ($\hat{y^*}$), which correspond to class 1 or class 0.

The individual classifiers analyzed here can be categorized into two kinds based on the computational complexity. The first kind of classifiers incur low computational complexity such as kNN [85], and GMM [86] with two multivariate Gaussians, one Gaussian corresponding to class 0 and another to class 1. The second kind of classifiers with high computational complexity include kernel space SVM [87] [88] and AdaBoost [32], [84]. The Bayesian combination of these two categories of classifiers using the Dempster-Shafer theory [89] is also analyzed. Such a combinational classifier, SVM+GMM combines the independent prior probabilities from the SVM and GMM classifiers, and SVM+kNN combines the priors from SVM and kNN, respectively. These classifiers are implemented in MATLAB and the priors for the SVM classifier for the combinational classifiers are computed using the libSVM toolbox [90].

5.3 Proposed System

In the proposed automated system, all images are preprocessed first to eliminate false photographic artifacts and illumination inconsistencies. The pre-processing module proceeds by histogram equalization and contrast enhancement on I_{green}, followed by scaling all pixel intensities in the range [0,1] resulting in image I_m. Next, since the quality of images vary among data bases, it is necessary to enhance the sharpness and illumination of certain images especially when the images are scanned film prototypes. I_m is filtered using the Laplacian of Gaussian filter to extract the gradient variations (I_h). Next, $(I_m - I_h)$ is median filtered to obtain the enhanced images as shown in Fig. 5.2. Following the pre-processing module, the three detection stages are invoked for DR severity detection per image.

5.3.1 Stage 1: Image Segmentation

In the first stage, it is imperative to mask out the regions corresponding to the optic disc (OD) and major portions of the blood vasculature. This is important since a bright OD may otherwise be mistaken for a bright lesion, and the vasculature can be falsely detected as a red lesion in subsequent automated stages if not masked out in the early stage. For this purpose, a region based *MinIMaS* algorithm [10] is invoked, which detects the regions that lie on the intersection of the largest red region and the bright regions in

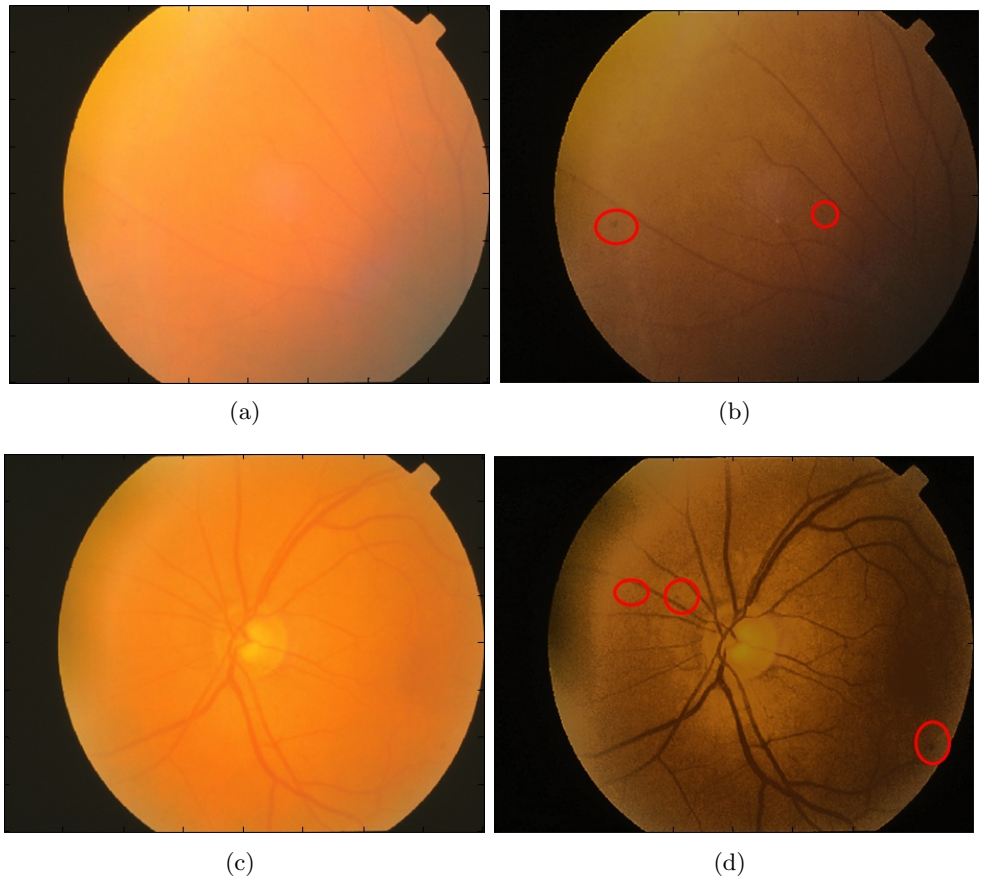

Figure 5.2: Original blurry images are enhanced by spatial filtering. (a), (c) Fundus image (I), (b), (d) Filtered image with enhanced red lesions marked in red circles.

the image. Once all such intersecting bright regions are identified (R), then the region containing the OD ($R_{OD} \subset R$) is the bright region with minimum pixel intensity sum ($Intensity$, due to the dark pixels corresponding to thick blood vessels occurring at the OD region), and maximum compactness (Sol) as represented in (5.10). If the region with minimum pixel intensity sum is not the same as the region with maximum solidity ($i_1 \neq i_2$), then the region with minimum pixel intensity sum is discarded ($R = R \backslash R_{i_1}$), and (5.10) is re-evaluated for the remaining regions till convergence is achieved.

$$\text{If, } R = \{R_1, R_2, ...R_r\}, i \in \{1, 2, ...r\}, \tag{5.10}$$

$$\Lambda(R) = [i_1, i_2 : i_1 = \arg\min_i Intensity(R_i), \quad i_2 = \arg\max_i Sol(R_i)].$$

$$R_{OD}(\Lambda(R)) = \begin{cases} R_{i_1} = R_{i_2} & : i_1 = i_2 \\ R_{OD}(\Lambda(R = R \backslash R_{i_1})) & : i_1 \neq i_2. \end{cases} \tag{5.11}$$

After R_{OD} detection, to detect major portions of the blood vasculature (R_{vasc}), each image is gradient smoothened by median filtering (I_{bg}), and subtracted from image I_m to obtain the shade corrected image ($I_{sc} = I_m - I_{bg}$), followed by thresholding and region growing. The largest red region extracted after region growing corresponds to R_{vasc}.

Once the OD and blood vessels are detected and masked out as background regions, foreground candidate regions (R_{fore}) that may represent retinopathy lesions are detected, thereby resulting in a segmented image [10]. This process is shown in Fig. 5.3. Once the fundus images are segmented and the foreground candidate regions are detected, the second stage of the algorithm is invoked that classifies the bright candidate regions (R_{BL}) and red candidate regions (R_{RL}) as retinopathy lesions.

5.3.2 Stage 2: Lesion Classification

Following foreground detection, for all the 6 classifiers under analysis, a training data set was used to obtain the optimal parameters for classification, and a separate test data set was used to analyze their performance.

Lesion classification is performed in two hierarchical binary (1/0) classification steps. In the first step, the bright candidate regions (R_{BL}) are classified as true bright lesions (R_{TBL}, class 1) and non-bright lesions (R_{NBL}, class 0), while the red candidate regions (R_{RL}) are classified as true red lesions (R_{TRL}, class 1) and non-red lesions (R_{NRL}, class 0), respectively. In the second level, the true bright lesions are reclassified as cotton wool spots ($\hat{R_{CWS}}$, class 1) and hard exudates ($\hat{R_{HE}}$, class 0), while the true red lesions are classified as micro-aneurysms ($\hat{R_{MA}}$, class 1) and hemorrhages ($\hat{R_{HA}}$, class 0).

Selection of features is an important aspect for lesion classification. Prior works have introduced feature sets comprising of 13 features [31] using the Spencer-Frame system, while extensions of these features up to 68 features for lesion classification have been presented in [91]. Motivated from these prior works, in this chapter, we analyze a set of 78 features that consists of most of the features from [31] and [91] along with additional structural features that are obtained using the 'regionprops' command in MATLAB. Here, 14 features are structure based features such as area, convex area, solidity, orientation etc., and 16 features correspond to the mean, minimum, maximum and standard deviation of pixels within each object region in the green plane (I_{green}), red plane (I_{red}), saturation plane (I_{sat}) and intensity plane (I_{inten}) of the RGB to HSI converted image. The 14 structure based features are useful primarily for separating the non-lesion regions from the lesion candidates. For example bright lesions (HE and CWS) in general have a higher distance from the OD region compared to the non-lesions. For the red lesion classification, the non-lesion regions generally represent fine blood vessels and hence the non-lesions on an average have a smaller distance from the blood vessels than the red lesions. Also, the blood vessels are elongated structures, and hence for the non-lesion regions, the ratio of major axis to minor axis lengths is higher than the hemorrhages or micro-aneurysms. For the second step of hierarchical bright lesion classification, hard exudates (HE) are compact bright regions with well defined boundaries as compared to the cotton-wool spots (CWS) that are larger in area, and less compact (low solidity). The remaining 48 features correspond to the mean and standard deviation of 6 second-order derivative images corresponding to coefficients of the constant, first and second-order horizontal derivative and vertical derivative images ($[1, I_x, I_y, I_{xy}, I_{xx}, I_{yy}]$) scaled in [0,1], using a Gaussian filter with zero mean and $\sigma^2 = [1, 2, 4, 8]$. These 48 features are useful for the second step of hierarchical classification.

In this chapter, we selected the top 30 features shown in Table 5.1 out of 78 features that were ranked in decreasing order of feature weights generated by AdaBoost 5.12 [32]. For this feature selection operation we used the 89 images from the DIARETDB1 [60] dataset. This process of feature selection for improving the classification performance and computational speed of the algorithm can be viewed as analogous to reverse feature elimination for horizontal pruning in decision tree-based learning as mentioned in [92].

Corresponding to each foreground candidate object for bright and red lesions, 78

features are extracted ($\mathbf{x}$), and each region is manually annotated as a lesion or non-lesion (y). Next the Adaboost algorithm in (5.12) is invoked to generate feature weights based on the linear discriminating performance of each feature, followed by feature ranking. The top 30 features were the ones with non-zero positive feature weights for classifying bright and red lesions.

While implementing Adaboost for feature selection [84], the weight of each object ('i') is first initialized ($W_{1,i}$). Next, we analyze the $F = 78$ features over $T = 100$ iteration rounds. For each feature 'j', at iteration 't', a linear classifier classifies sample x_i as $h_{t,j}(x_i)$, such that the classification outcome $h_{t,j}(x_i) = 0$ or 1. Classification error due to this 1-feature based classifier on all samples is $\epsilon_{t,j}$. At any iteration 't', the classifier with minimum $\epsilon_{t,j}$ is chosen as ϵ_t. This error (ϵ_t) is then used to update the sample weights, such that the misclassified samples are weighted more than the correctly classified samples. The final resulting classifier is a weighted linear combination of the linear classifiers in each iteration step as shown in (5.13). Also, after 'T' iterations, the weights of selected discriminating features in each iteration are combined to find the weight of each feature in the final classifier in (5.14). Features are then ranked in descending order of their contributing weights.

$$\textbf{Initialize}: W_{1,i} = 1/N, \quad t = 1:T \tag{5.12}$$

$$\textbf{Define}: \forall j = 1:F,\ h_{t,j}(\mathbf{x}_i) \in [0,1]$$

$$\epsilon_{t,j} = \sum_{i=1}^{N} W_{t,i}.\,|h_{t,j}(\mathbf{x}_i) - y_i|,$$

$$h_t = \arg\min_j \epsilon_{t,j},\ \epsilon_t = \min_j \epsilon_{t,j}$$

$$\textbf{Stop iterating if } \epsilon_t \geq 0.$$

$$\textbf{Update}: \qquad W_{t+1,i} = \frac{W_{t,i}\exp(\alpha_t(er_i))}{Z_t}$$

$$\alpha_t = \frac{1}{2}\ln(\frac{1-\epsilon_t}{\epsilon_t}),\ Z_t = \texttt{Normalizer}$$

$$er_i = \begin{cases} -1 & : h_t(\mathbf{x}_i) = y_i \\ 1 & : h_t(\mathbf{x}_i) \neq y_i. \end{cases} \quad \alpha_{t,j} = \begin{cases} \alpha_t & : \epsilon_t = \epsilon_{t,j} \\ 0 & : \epsilon_t \neq \epsilon_{t,j}. \end{cases}$$

$$\textbf{Finally}: \quad \hat{y^*} = \begin{cases} 1 & : \sum_{t=1}^{T} \alpha_t.h_t(\mathbf{x}^*) > 0 \\ 0 & : otherwise. \end{cases} \tag{5.13}$$

$$\textbf{Feature Weight}: \ S(j) = \frac{\sum_{t=1}^{T} \alpha_{t,j}}{\sum_{j}^{F}\sum_{t=1}^{T} \alpha_{t,j}}. \tag{5.14}$$

Following feature selection, each foreground candidate object is then classified using the top 30 features described in Table 5.1. The feature vector ($\mathbf{x}$) corresponding to each object in the feature space is computed. In the training phase of lesion classification, the 30-dimensional feature space, with each dimension representing a particular feature, is populated with the objects from the training set of images. The position of each object in the feature space is determined by the feature vector ($\mathbf{x}$), and the class labels of the objects belonging to the training data set (y) are used to determine the class labels of objects belonging to the test data ($\hat{y^*}$) in the testing phase. The two-step hierarchical classification approach is illustrated for an image from the DIARETDB1 data base in Fig. 5.4.

After the lesions are classified for each image, the next task is to fuse the information regarding the lesions detected to generate a DR severity level for each image [4].

5.3.3 Stage 3: DR Severity Grading

Once the regions corresponding to the retinopathy lesions are detected, and the number of hemorrhages (HA), microaneurysms (MA), hard exudates (HE) and cotton-wool spots (CWS) are computed per image using (5.6)-(5.7), lesion combination (ψ) operation defined in Table 5.2 for the MESSIDOR [62] data set can be used to generate a DR severity grade per image (G). The impact of lesion combination on DR severity have been studied in [93], [94] to derive the DR severity grading gold standards. These studies demonstrate that clinically relevant lesion combination operations require more accurate estimation regarding the number of red lesions than bright lesions. In case of bright lesions, over detection, or instances of false positives may imply macular degeneration or retinal abnormalities other than NPDR. Thus, detection of bright lesions must incur less false positives. However, for red lesion detection, failure to detect lesions will result in false interpretation of the DR severity. Thus, it is imperative for any automated system to incur low false negatives for red lesion classification. Hence, the performance criteria for selecting lesion classifiers are as follows:

- *Bright lesion classifier*: It must incur low false positives, or high specificity.
- *Red lesion classifier*: It must incur low false negatives, or high sensitivity.

5.4 Results

We analyze the performance of the three stages of the DR screening systems individually. In the first image segmentation stage, the detection of the OD region plays a vital role to ensure fewer instances of false positive while detecting bright lesions. This segmentation algorithm has shown to have an accuracy of 99.7% for OD segmentation on public data sets [10].

The metrics used for analyzing the performance of the second and third stages of the detection system are defined in terms of true positives (TP), true negatives (TN), false positives (FP), and false negatives (FN) as follows.

- sensitivity (SEN)= $\frac{TP}{TP+FN}$

- specificity (SPEC)= $\frac{TN}{TN+FP}$
- area under ROC curve (AUC).

The final goal of our DR detection system is to classify the fundus images that are free from retinopathy lesions as normal, and to classify the images with bright and red lesions as abnormal. The receiver operating characteristic (ROC) curves are obtained by varying the threshold probability in increments of 0.02 in the range [0,1], and observing the variation in SEN versus (1-SPEC) each time. The following subsections present the selection of the best set of classifiers for bright and red lesion classification that have comparatively high SEN, SPEC, and AUC. The DREAM system applies the classifiers that have a consistent performance across both data sets.

5.4.1 Feature Set and Classifier Evaluation for Data Set 1: DIARETDB1

Classification of bright lesion and red lesions vs. non-lesions for the DIARETDB1 data set has been analyzed using kNN, GMM and SVM classifiers in [10]. However, in this chapter, we extend the analysis to two hierarchical step classification, to assess the impact of combination classifiers, and to analyze the incremental importance of the classifying feature set. In lesion classification analysis, a TP region is one which is classified as a lesion and that has more than 50% of its pixels manually marked as a lesion with greater than 50% confidence by the authors of [60].

In Section 5.3.2, Table 5.1, top 30 features computed using AdaBoost, for bright and red lesion classification, are ranked in decreasing order of their contribution to lesion classification. To analyze the importance of these 30 features for lesion classification, we selected the top 'F' features, where F= $\{5, 10, 15, 20, 25, 30\}$, and observed the lesion classification performance on the test set of images from the DIARETDB1 data set. In the first hierarchical classification step, candidate regions for bright and red lesions are separated from false positives. The SEN/SPEC of each classifier with varying 'F' is shown in Tables 5.3 and 5.4 for bright lesion and red lesion classification, respectively. The threshold probabilities obtained from the ROC curves for evaluating a candidate region as a bright or red lesion in hierarchical Step 1 classification for $\{GMM, kNN, SVM + GMM, SVM + kNN\}$ are approximately $\{0.4, 0.3, 0.45, 0.35\}$,

respectively. For Step 2 classification, threshold probability is about 0.45 for all probabilistic classifiers. For the SVM and AdaBoost classifiers, a single operating point is observed since the final classifier is based on the sign of the decision principle. Also, we observe that AdaBoost generates more FNs compared to SVM, which is undesired for lesion classification. It is noteworthy that prior to this lesion classification step, the top 30 features were selected using AdaBoost on all the 89 images from the DIARETDB1 data set to obtain a better fitted feature selection strategy than using the training set of 28 images.

To compare the performance of SVM and AdaBoost with other classifiers for Step 1 bright lesion classification, using the 30 feature set, we observe that at $SEN = 0.98$, GMM, kNN, SVM+GMM, SVM+kNN have $SPEC = \{0.68, 0.45, 0.1, 0.49\}$, respectively. At $SEN = 0.92$, GMM, kNN, SVM+GMM, SVM+kNN have $SPEC = \{0.82, 0.67, 0.41, 0.71\}$, respectively. Thus, from Table 5.3, we observe that for bright lesion classification, the GMM classifier has the highest achievable specificity at a given sensitivity for the most important Step 1 of hierarchical classification. In Step 2 of hierarchical classification, all classifiers demonstrate comparable performance. Thus, hard exudates can be very well separated from cotton-wool spots using the 30 feature set. Also, due to comparable classification performances in Step 2, the low complexity GMM classifier is preferable.

To compare the performance of SVM and AdaBoost with the other classifiers for Step 1 red lesion classification, using the 30 feature set, we observe that at $SPEC = 0.99$, SEN of GMM, kNN, SVM+GMM, SVM+kNN is $\{0.67, 0.68, 0.63, 0.63\}$, respectively. And at $SPEC = 0.97$, SEN of GMM, kNN, SVM+GMM, SVM+kNN is $\{0.69, 0.72, 0.64, 0.65\}$, respectively. Also, for Step 1 classification using AdaBoost classifier with $F = \{5, 10\}$ feature set, the training process stops after $T = \{68, 43\}$ iterations, respectively, instead of completing the $T = 100$ iterations for model selection. These correspond to the entries marked by "$[SEN/SPEC]$" in Table 5.4. The reason for these incomplete training processes is that the weighted error in classification exceeds random error of 0.5. Once the feature set exceeds 15 and more features, AdaBoost classification performance improves due to appropriate model selection after the complete training process.

From Table 5.4, we conclude that for red lesion classification, kNN achieves highest

SEN for a given SPEC. Also, for Step 2 of hierarchical red lesion classification, all classifiers have comparable performances implying that micro-aneurysms can be very well separated from hemorrhages using the 30 feature set. Hence, the 30 feature set is adequate for lesion classification.

5.4.2 Classifier Evaluation for Data Set 2: MESSIDOR

For the MESSIDOR data set, classifiers are trained on 89 images from the DIARETDB1 data set with 30 features and tested on 1200 images for detection of hemorrhages and microaneurysms in each image. In this chapter, we do not analyze instances of neovascularization or proliferative DR, and we utilize the lesion combination (ψ) operation defined in Table 5.2. According to the reference standard [62], out of the 1200 images, a total of 546 images are normal ($G = 0$), and 654 are abnormal images ($G > 0$) presenting signs of DR. The DR images comprise of 153 images with retinopathy grade 1, 247 images with retinopathy grade 2, and 254 images with retinopathy grade 3. Using the 89 images from the DIARETDB1 for training, the best values of k, for kNN classifier, were found as: $k = 11$ for Step 1 red lesion classification (R_{TRL} vs R_{NRL}), and $k = 3$ for Step 2 classification of $\hat{R_{MA}}$ from $\hat{R_{HA}}$.

The performance of classifying normal images ($G = 0$) from all other images with non-zero diabetic grades ($G = 1, 2, 3$) is depicted in Table 5.5. The number of images with non-zero DR grade that are falsely graded as $G = 0$ are represented as $\#FN$ in Table 5.5. The operating point in this analysis is selected where SEN is greater than 0.9 and SPEC is approximately 0.5 [95], such that the threshold probabilities for Step 1 red lesion classification for GMM, kNN, SVM+GMM, SVM+kNN are $\{0.4, 0.3, 0.45, 0.35\}$, respectively. For Step 2 classification, the threshold probability is 0.45.

From Table 5.5, we observe that SVM+kNN and kNN have good SEN/SPEC classification combination for separating normal images from abnormal ones. In such situations, the kNN classifier is preferable since it has lower computational complexity. Also, we observe the AdaBoost introduces the highest number of FNs (abnormal images incorrectly classified as normal), which is undesired. Besides, from Table 5.5, it is evident that the lesion combination operation reduces the impact of lesion classification. However, when the number of images being screened for DR becomes significantly large,

such as in the case of the MESSIDOR data set, slight variations in classification performances can be significant. For example, in Table 5.5, for the normal to abnormal image classification, kNN and SVM+GMM have SEN/SPEC 1/0.5316, 0.9916/0.5492, respectively. Although, these performances appear similar, the significant difference is that the SVM+GMM classifier falsely classifies 10 images with DR as normal images. As the number of patients being screened for DR increases, the number of missed screenings will grow, which is undesired from an automated screening system.

Additionally, from Table 5.6, we observe that combination classifiers do not show significant improvement over single classifiers in both data sets. Also, combination classifiers introduce computational complexity, thus discouraging their use for lesion classification.

The important conclusion from the classification performance analysis of the two data sets is that, GMM may be preferred for classification of bright lesions, while kNN outperforms GMM and SVM for red lesion classification. Thus, for our three-stage screening system (DREAM), we use GMM for classification of bright lesions and on kNN for classification of red lesions.

5.4.3 Time complexity Analysis of the DREAM system

The time complexity of the proposed DREAM system for red lesion and bright lesion detection is analyzed in terms of the time required to classify the lesions and grade images using MATLAB programs. On a Laptop (2.53 GHz Intel Core i3 and 2 GB RAM), the times required per image to classify candidate objects corresponding to lesions on the image from DIARETDB1, and to grade images from the MESSIDOR data set are shown in Table 5.7.

In the DIARETDB1 data set, for each test image, the time required to classify bright candidate objects into HE/CWS, and the red candidate objects into MA/HA after rejecting false positives are analyzed using 3 classification methods. The first method (M1) uses 78 features for classifying bright objects using GMM classifier and red lesions using kNN classifier in two hierarchical steps. The second method (M2) uses the top 30 features for classification, but it uses 2 separate GMM classifiers in parallel for discriminating CWS from non-bright lesions, HE from non-bright lesions, and 2 separate kNN classifiers in parallel for separating MA from non-red lesions and HA from non-red

lesions, respectively. The third method (M3) follows the 2-step hierarchical classification using 30 features as defined in (3-5). In the MESSIDOR data set, all the 3 classification methods (M1, M2, M3) are used for red lesion classification only followed by generating a DR severity grade per image.

Table 5.7 shows a 97% time complexity reduction (from 71.63s to 2.06s) for images from DIARETDB1, and 94.18% reduction (from 59.54s to 3.46s) for images from MESSIDOR data set in the average bright and red lesion detection time required per image. This reduction in time complecity is achieved by reducing the number of features from 78 to 30 and applying the proposed 2-step hierarchical classification method.

Next, we observe that the proposed 2-step hierarchical classification method (M3) incurs 18.5% less time than the parallel classification method M2 (2.06s vs. 2.53s) for DIARETDB1 images, and 24.45% less time (3.46s vs. 4.58s) for MESSIDOR images. The best SEN/SPEC obtained by M2 and M3 on the DIARETDB1 and MESSIDOR data sets are 0.82/0.94, and 1/0.53, respectively.

5.4.4 Comparison with Prior Work

Comparative performance analysis of the proposed system (DREAM) in classifying bright and red lesions to existing works is shown in Table 5.8. The SEN/SPEC of the DREAM system is chosen from the ROC curves corresponding to the GMM classifier with 30 feature set and threshold probability 0.7 for bright lesion classification, and kNN classifier with 30 feature set and threshold probability 0.3 for red lesion classification, respectively. We observe that the DREAM system has a favorable Step 1 classification performance for bright and red lesions compared to existing methods. Additionally, the proposed system has 95% sensitivity and 90% specificity for separating micro-aneurysms from hemorrhages, and 99% sensitivity, 97% specificity for separating hard exudates from cotton-wool spots. From Table 5.8, we observe that prior works on lesion classification using the DIARETDB1 data set also demonstrated a preference for high SPEC for bright lesion classification and high SEN for red lesion classification, which is in accordance with our classifier evaluation criteria.

Comparing the performance of classification and image grading of our system with existing works on the public data set MESSIDOR [62], the proposed system achieves higher sensitivity, specificity and AUC, as shown in Table 5.9. Another ARVO 2008

version of the method in [98] tested on 400 images from this data set achieved an AUC of 0.89 in classifying images with grade 0 and grade 1 from the images with a higher retinopathy severity grade. Our system outperforms all existing methods that classify all the 1200 images from the MESSIDOR data set. In Table 5.9, the method [100] classifies normal from abnormal images by sub-sampling from the MESSIDOR image set to train, validate and test neural network classifiers. Thus, this method classifies about 300 images or less out of the 1200 images. Also, the performance of other DR severity grading methods on various local data sets is shown in Table 5.9. We observe that only the proposed system achieves 100% sensitivity, which is favorable over existing grading systems since no patient with DR is missed while screening using the DREAM system.

5.5 Conclusions and Discussion

In this chapter we have proposed a three-stage computer-aided screening system for DR (DREAM) that detects and grades fundus images for the severity of NPDR. In this chapter, we have identified a set of best 30 features out of 78 features using feature scoring by AdaBoost [84], such that the 30 feature set classifies bright and red lesions with AUC greater than 0.83 using the classifiers such as kNN, GMM and Bayesian combination of probabilistic classifiers (SVM+GMM, SVM+kNN). Additionally, time complexity analysis of the proposed 2-step hierarchical classification method using all the 78 features and the reduced 30 feature set demonstrates computational speed enhancement by more than 94% by this feature reduction operation. This time complexity analysis is a significant contribution, since to our best knowledge no prior works have reported the time complexity of the DR detection systems. The final 30 features are capable of classifying lesions under 6 seconds per image, and these 30 features are scalable across image data sets with varying fields of view.

It is noteworthy that the first stage of the DREAM system is an important step for correctly detecting the presence of diabetic retinopathy (DR). Among all the images analyzed in this chapter from the public data set of DIARETDB1 and MESSIDOR (which includes 1289 fundus images), the optic disc (OD) and blood vessels have always been correctly segmented. However, it is possible that for some fundus images with

additional retinal pathologies such as myelination or peripapillary atrophy, the entire OD region is not completely masked out. This might result in an additional bright lesion being detected by the DREAM system. Also, since the minimum distance from the OD region is a feature for lesion classification in the second stage of the system, erroneous segmentation of the OD might lead to minor inaccuracies in lesion classification. However, this classification error is significantly small since the error appears due to 1 out of 30 un-weighted features, and since the minimum distance from OD is an important classification feature for mainly bright lesions regions. Since bright lesions are not considered for evaluating the severity of DR by the proposed system, this false detection of the OD region will not impact the final DR severity grade produced by the DREAM system.

In instances when the retina severely degenerates, such as the examples shown in Fig. 5.5, where retinal vein occlusions occur, the DREAM system classifies such images as abnormal, even if the patients don't suffer from DR. Such fundus images would result in false positive outcomes by the automated screening system. However, all false positive outcomes will be further manually assessed by retinal specialists to determine follow-up treatment procedures. Hence, a patient with retinal vein occlusion will be detected as abnormal by the DR screening system, and the patient will be further manually assessed.

The lesion classification problem in the second stage of the DREAM system deals with unbalanced data sets. Hence, it is important to discuss the performance of the lesion classifiers on the unbalanced lesion candidate regions. A trained SVM classifier generally tends to classify each test sample as belonging to the majority class [87] [88], thereby causing a biased classification outcome. The AdaBoost classifier is accuracy-oriented, which means that its weighting strategy may be biased towards the majority class if it contributes more to the overall classification accuracy as mentioned in [107]. To ensure low computational complexity for the proposed DR screening system, cost-sensitive SVM and AdaBoost classifiers [107] have not been assessed in this chapter. Future works will be directed towards analyzing the impact of cost-sensitive SVM and AdaBoost for lesion classification. The GMM classifier is weighted by the number of samples belonging to class 1 or class 0 at the end of the Expectation Maximization operation, and hence it is quite robust to handling unbalanced data sets as mentioned in [108]. The kNN classifier has a localized impact while classification since each data

sample looks at its immediate neighborhood to decide its class label. Existing works [109] have shown that kNN is robust to imbalance in data set caused due to a high number of negative samples. In this chapter we observe that for the red lesion classification problem, where the numbers of negative samples are 4 times more than the number of positive samples, kNN is the best classifier, an observation which is in accordance with the existing works [109]. Combination of SVM with kNN or GMM classifiers using the Dempster-Shafer theory [89] does not significantly enhance the lesion classification performance since SVM is sensitive to the imbalance in the data, and hence, the classification performance of the combined classifiers is dampened. However, other classifier combination strategies may enhance the lesion classification performance. Future work will be focused on the assessment of other classifier combination strategies for the lesion classification problem.

Although the proposed DREAM system outperforms all existing DR screening systems, further improvement in DR classification specificity may be possible by retraining the lesion classifiers for every new test set of images, by using cost-sensitive SVM or AdaBoost classifiers for lesion classification, or by using other cost-sensitive classifier combination algorithms. Future work will be directed towards further enhancement of the DR classification performance. However, classifier retraining or cost-sensitive classifiers may incur additional computational time complexity. Additional future work can be directed towards the detection of neovascularization and vascular beading caused by proliferative DR, and drusen caused by macular degeneration.

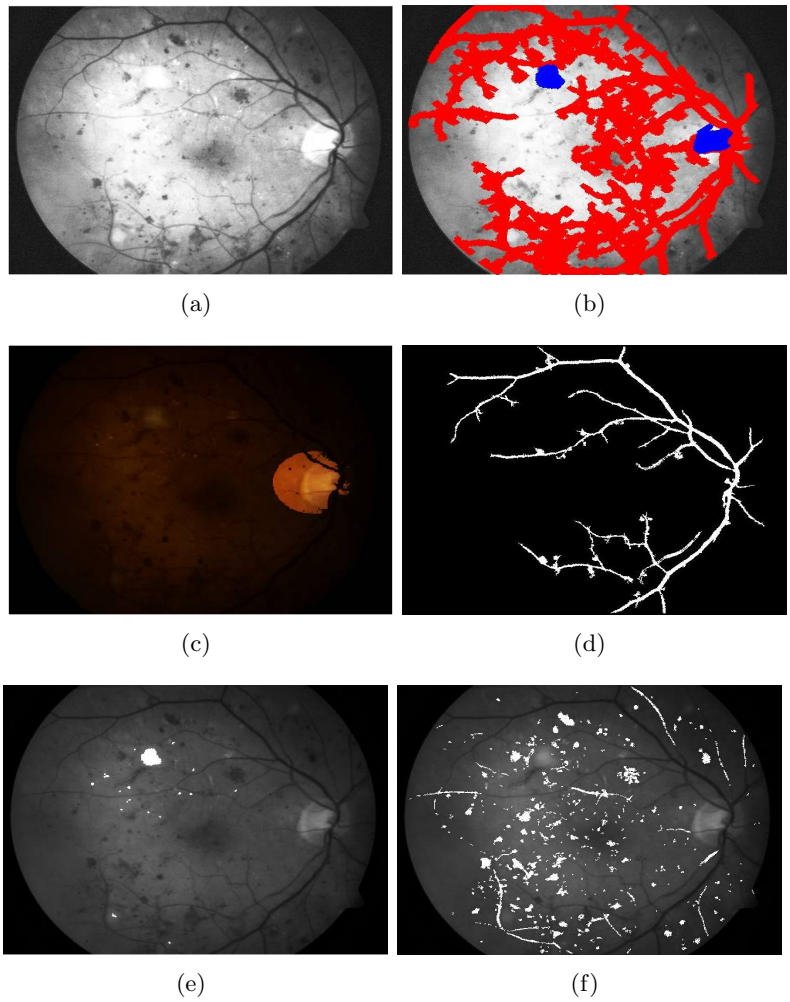

Figure 5.3: Detection of OD, vasculature and foreground candidate regions. (a) illumination corrected pre-processed image. (b) Intersecting red regions and bright regions (blue), out of which OD is selected as the bright region with highest solidity. (c) OD (R_{OD}) detected. (d) vasculature (R_{vasc}) detected. (e) Candidate bright lesion regions (R_{BL}) detected. (f) Candidate red lesion regions (R_{RL}) detected.

Table 5.1: Features for classification

Rank	Feature
1	Area: Total pixels in the object.
2	Minimum distance from center of R_{OD}
3	Major Axis length: Major axis of the ellipse (E).
4	Minor Axis length: Minor axis of the ellipse (E).
5	Variance of pixels for the object region in I_{green}.
6	Mean of pixels for the object region in I_{green}.
7	Variance of pixels for the object region in $I_{yy}, [\sigma^2 = 8]$.
8	Variance of pixels for the object region in $I_{xy}, [\sigma^2 = 8]$.
9	Diameter of a circle that with same area as the object.
10	Variance of pixel intensities for the object region in I_{red}.
11	Variance of pixel intensities for the object region in I_{sat}.
12	Length of smallest rectangle (bounding box) around the object.
13	Mean pixel intensity for the object region in I_{red}.
14	Eccentricity of an ellipse (E) estimated around the object with same normalized second central moments as the object.
15	Variance of pixel intensities for the object region in I_{inten}.
16	Filled Area: Area of the object with all holes filled.
17	Width of smallest rectangle (bounding box) around the object.
18	Minimum distance from R_{vasc}.
19	Minimum pixel intensity for the object region in I_{sat}.
20	Mean pixel intensity for the object region in I_{inten}.
21	Orientation: Angle in degrees between the x-axis and the major axis of the ellipse (E).
22	Perimeter: Distance around the object region.
23	Minimum pixel intensity for the object region in I_{red}.
24	Maximum pixel intensity for the object region in I_{inten}.
25	Minimum pixel intensity for the object region in I_{inten}.
26	Solidity = $\frac{area}{convex\ \ area}$.
27	Euler number of the object.
28	Maximum pixel intensity for the object region in I_{red}.
29	Maximum pixel intensity for the object region in I_{sat}.
30	Mean pixel intensity for the object region in I_{sat}.

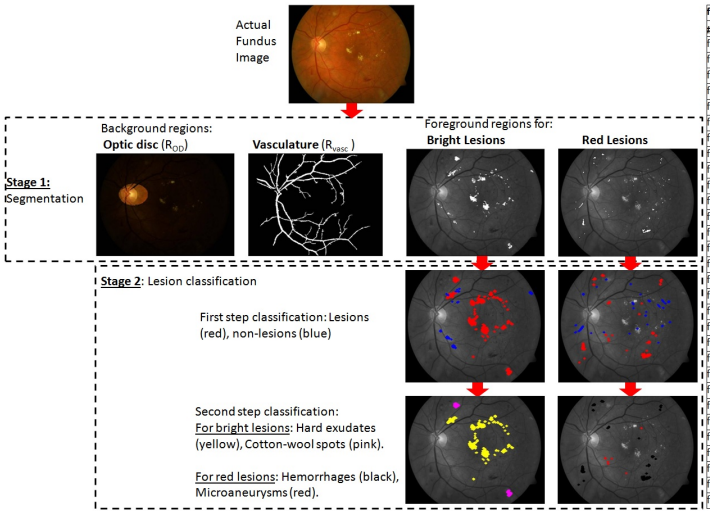

feature(Rank)	NBL	HE	CWS	NRL	HA	MA
# regions	14	51	2	29	22	6
f1	18.5714	40.6275	209	7.6207	26.4091	5.3333
f2	117.695	175.1823	253.5167	179.6377	203.0532	133.4392
f3	6.7548	7.8582	23.9723	8.6377	5.3569	3.5988
f4	3.62	4.2408	15.1823	2.0476	3.9161	2.0642
f5	4.02E-05	0.002	4.48E-04	1.79E-04	1.44E-04	1.30E-04
f6	0.8079	0.7841	0.7684	0.354	0.3441	0.3217
f7	0.0293	0.0671	0.0272	0.0276	0.0399	0.034
f8	0.0322	0.0818	0.0288	0.0252	0.0311	0.0392
f9	4.1651	5.02	16.2733	2.8412	4.8865	2.5581
f10	8.00E-05	9.10E-04	2.97E-04	2.44E-04	1.49E-05	6.97E-05
f11	4.52E-06	3.44E-05	2.17E-05	1.42E-05	8.64E-06	7.09E-06
f12	5	5.5882	17	8.3103	5.7727	2.3333
f13	0.7021	0.6371	0.5303	0.5273	0.5015	0.4833
f14	0.8328	0.7975	0.7083	0.8595	0.7512	0.8024
f15	8.00E-05	9.10E-04	2.97E-04	2.44E-04	1.49E-04	6.97E-05
f16	18.6429	41	209	7.6207	26.5909	5.3333
f17	5.4286	6.8824	25	2.3793	7	3
f18	5.3199	14.2135	21.041	7.62	10.024	11.1042
f19	0.0737	0.0754	0.0799	0.0545	0.0218	0.0112
f20	0.7021	0.6371	0.5303	0.5873	0.5015	0.4833
f21	-19.7164	9.7532	7.86055	-12.9996	29.8739	21.9229
f22	18.8822	23.3977	91.7904	9.753	20.7352	5.8856
f23	0.6902	0.6037	0.4902	0.5094	0.4836	0.4739
f24	0.7154	0.6744	0.5686	0.5413	0.5223	0.4948
f25	0.6902	0.6037	0.4902	0.5094	0.4836	0.4739
f26	0.8141	0.8965	0.7194	0.82	0.898	1
f27	0.9286	0.9804	1	0.91	1	1
f28	0.7154	0.6744	0.5686	0.5413	0.5223	0.4948
f29	0.0802	0.0897	0.1046	0.0573	0.0611	0.0619
f30	0.0769	0.0825	0.0934	0.0538	0.0567	0.0589

Figure 5.4: Two-step hierarchical classification of lesions for an image from DIARETDB1. In Stage 1 of the automated system, background regions corresponding to vasculature and optic disc are first detected. Candidate regions for bright (R_{BL}) and red lesions (R_{RL}) are then detected as the foreground. In Stage 2, hierarchical two-step classification is performed for identification of the type of lesions. In the first hierarchical classification step, foreground regions for bright lesions are classified as true lesions (red, R_{TBL}) and non-lesions (blue, R_{NBL}), and candidate regions for red lesions are classified as true red lesions (red, R_{TRL}) and non-lesions (blue, R_{NRL}). In hierarchical second-step classification, true bright lesions are classified into hard exudates (yellow, $\hat{R_{HE}}$), and cotton wool spots (pink, $\hat{R_{CWS}}$), while true red lesions are classified as microaneurysms (red, $\hat{R_{MA}}$), and hemorrhages (black, $\hat{R_{HA}}$). Corresponding to the 30 features mentioned in Table I, the average feature values for all the candidate lesion regions in the sample image is presented in the adjoining table (i.e., f_1 corresponds to feature with rank 1, which is area of the region). The features measuring distance are in terms of pixels, while the mean and variance of intensity values are scaled in [0, 1] range.

Table 5.2: The lesion combination (ψ) operation proposed for MESSIDOR.

Grade	Description
0	$(MA = 0)$ and $(HA = 0)$
1	$(0 < MA \leq 5)$ and $(HA = 0)$
2	$(5 < MA \leq 15)$ or $(0 < HA < 5)$
3	$(MA \geq 15)$ or $(HA \geq 5)$

Table 5.3: SEN/SPEC for Two Hierarchical Step Bright Lesion Classification on DIARETDB1 Data Set.

Classifier	No. of features					
	5	10	15	20	25	30
Step 1:	R_{TBL}	vs	R_{NBL}			
GMM	0.62/0.85	0.66/0.85	0.73/0.85	0.79/0.85	0.87/0.85	**0.89/0.85**
kNN	0.67/0.85	0.76/0.85	0.81/0.85	0.81/0.85	0.84/0.85	0.86/0.85
SVM	0.67/0.63	0.89/0.62	0.84/0.69	0.95/0.76	0.95/0.72	0.98/0.59
SVM+GMM	0.60/0.84	0.66/0.85	0.70/0.85	0.76/0.85	0.78/0.85	0.81/0.85
SVM+kNN	0.68/0.85	0.73/0.85	0.77/0.85	0.79/0.85	0.83/0.85	0.86/0.85
Adaboost	0.61/0.90	0.62/0.94	0.73/0.95	0.85/0.85	0.85/0.87	0.92/0.79
Step 2:	$\hat{R_{HE}}$	vs	$\hat{R_{CWS}}$			
GMM	0.94/0.97	0.97/0.97	0.98/0.97	0.98/0.97	0.98/0.97	0.99/0.97
kNN	0.82/0.97	0.87/0.97	0.88/0.97	0.95/0.97	0.96/0.97	0.98/0.97
SVM	0.95/0.98	0.97/0.96	0.95/0.99	0.97/0.99	0.98/0.99	0.99/1
SVM+GMM	0.93/0.97	0.94/0.97	0.97/0.97	0.97/0.97	0.97/0.97	0.98/0.97
SVM+kNN	0.95/0.97	0.96/0.97	0.97/0.97	0.97/0.97	0.97/0.97	0.98/0.97
AdaBoost	0.93/0.92	0.95/0.93	0.96/0.91	0.96/0.98	0.97/0.95	0.98/0.98

Table 5.4: SEN/SPEC for for Two Hierarchical Step Red Lesion Classification on DIARETDB1 Data Set.

Classifier	No. of features					
	5	10	15	20	25	30
Step 1:	R_{TRL}	vs	R_{NRL}			
GMM	0.61/0.85	0.64/0.85	0.69/0.84	0.70/0.85	0.74/0.85	0.79/0.85
kNN	0.60/0.84	0.69/0.83	0.75/0.85	0.77/0.85	0.79/0.84	**0.80/0.85**
SVM	0.60/0.84	0.53/0.89	0.47/0.91	0.48/0.91	0.50/0.91	0.61/0.99
SVM+GMM	0.51/0.85	0.59/0.85	0.58/0.85	0.64/0.85	0.69/0.85	0.72/0.85
SVM+kNN	0.52/0.85	0.57/0.85	0.68/0.85	0.74/0.85	0.73/0.85	0.75/0.85
AdaBoost	[0.65/0.79]	[0.97/0.23]	0.51/0.97	0.56/0.97	0.59/0.97	0.60/0.97
Step 2:	$\hat{R_{MA}}$	vs	$\hat{R_{HA}}$			
GMM	0.74/0.90	0.75/0.90	0.79/0.90	0.80/0.90	0.81/0.90	0.82/0.90
kNN	0.75/0.90	0.76/0.90	0.84/0.90	0.93/0.90	0.94/0.90	0.95/0.90
SVM	0.83/0.94	0.86/0.95	0.87/0.96	0.85/0.97	0.94/0.97	0.97/ 1
SVM+GMM	0.82/0.90	0.85/0.90	0.88/0.90	0.91/0.90	0.92/0.90	0.97/0.90
SVM+kNN	0.80/0.90	0.87/0.90	0.90/0.90	0.92/0.90	0.94/0.9	0.95/0.90
AdaBoost	0.80/1	0.87/1	0.90/1	0.91/0.99	0.91/0.98	0.92/0.98

Table 5.5: Results of classification and lesion combination on MESSIDOR data set.

Statistics	kNN (DREAM)	GMM	SVM	SVM+ GMM	SVM+ kNN	Ada Boost
Grade:	(0 vs 1,2,3)					
SEN	1	1	0.8474	0.9916	1	0.8062
SPEC	0.5316	0.5316	0.6975	0.5492	0.5324	0.7648
# FN	0	0	182	10	0	231
Grade:	(0 vs 1)					
SEN	0.8940	0.9070	0.8974	0.9004	0.9053	0.8689
SPEC	0.5894	0.5158	0.5189	0.5330	0.5781	0.6312
# FN	61	53	50	58	52	75
Grade:	(0 vs 2)					
SEN	0.9507	0.9295	0.8787	0.9263	0.9568	0.8484
SPEC	0.5046	0.5035	0.5811	0.5033	0.5065	0.6773
# FN	36	49	89	51	32	111
Grade:	(0 vs 3)					
SEN	0.9888	0.9814	0.9479	0.9710	0.9876	0.9350
SPEC	0.4872	0.4842	0.5662	0.495	0.5097	0.6661
# FN	8	14	34	20	9	45

Table 5.6: AUC assessment on 3 data sets

Data set	kNN	SVM+kNN	GMM	SVM+GMM
DIARETDB1: R_{TBL}	0.9434	0.9533	0.9593	0.9222
DIARETDB1: R_{TRL}	0.8414	0.8356	0.8663	0.8300
MESSIDOR: (0/1,2,3)	0.9039	0.9097	0.8911	0.8826
MESSIDOR: (0/1)	0.9238	0.9151	0.923	0.9201
MESSIDOR: (0/2)	0.8915	0.8975	0.8831	0.8755
MESSIDOR: (0/3)	0.9314	0.9343	0.9087	0.9399

Table 5.7: Timing Analysis per image in seconds

Classification Method	Mean	Max	Min	Std. dev.
DIARETDB1				
M1 (F=78, hierarchical)	71.63	93.69	48.85	11.27
M2 (F=30, parallel)	2.53	7.67	1.16	2.17
M3 (F=30, hierarchical)	2.06	3.33	0.98	1.50
MESSIDOR				
M1 (F=78, hierarchical)	59.54	$2.58 \text{x} 10^3$	3.25	212.84
M2 (F=30, parallel)	4.58	7.55	1.64	1.60
M3 (F=30, hierarchical)	3.46	5.39	1.55	0.67

Table 5.8: Comparison of Lesion Detection Performance (%) on DIARETDB1

Lesion Type	Method	SEN (%)	SPEC (%)
Red	Bhalero et.al.[96]	82.6	80.2
Red	Kauppi et.al.[60]	77.78	76.47
Red	Proposed (DREAM)	80	85
Bright	Sophorak et.al.[97] (47 images)	43.48	99.31
Bright	Walter et.al.[98] (47 images)	66	98.64
Bright	Welfer et.al.[99] (47 images)	70.48	98.84
Bright	DREAM (61 images)	74.2	98

Table 5.9: Comparison of DR Severity Grading Performance for separating Normal from Abnormal images

Method	SEN (%)	SPEC (%)	AUC
MESSIDOR Data			
Sanchez et.al.[95]	92.2	50	0.876
Agurto et.al.[81]	92	54	0.84
Antal et.al.[101]	96	51	0.875
Esnaashari et.al.[100] ($\leq$ 300 images)	95	89.29	-
Barriga et.al.[102](400 images)	98	67	0.86
DREAM	100	53.16	0.904
Local Data			
Agurto et.al.[103](2247 images)	92	51	0.89
Acharya et.al.[104](300 images)	82	88	-
Acharya et.al.[105](331 images)	82	86	-
Usher et.al.[106](1273 images)	94.8	52.8	-

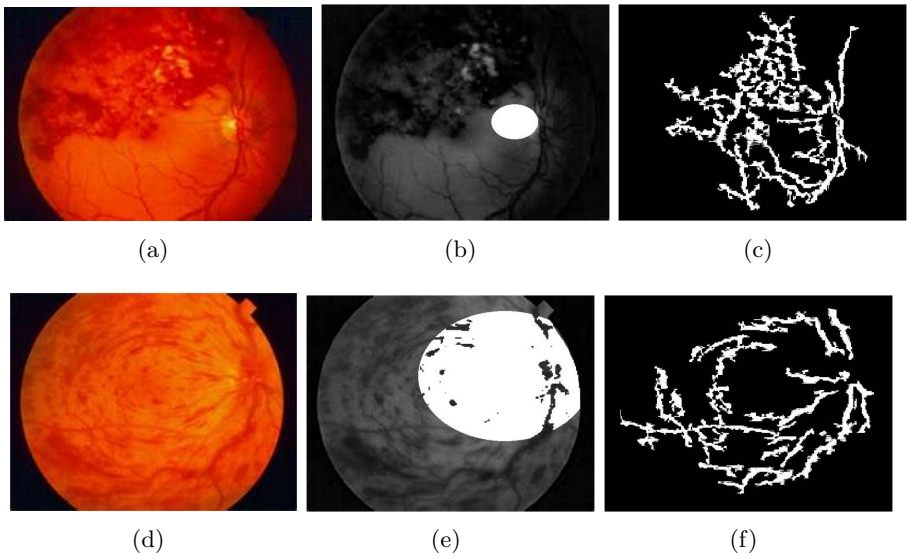

(a) (b) (c)

(d) (e) (f)

Figure 5.5: DREAM system on public domain images with severe retinal degeneration. (a), (d) Original image. (b), (e) OD region detected with error. (c), (f) Vasculature detected in first stage. Both images (a), (d) are classified as images with DR by the DREAM system.

Chapter 6

Automated Proliferative Diabetic Retinopathy Detection

6.1 Introduction

Diabetic retinopathy (DR) is the leading cause of preventable blindness among the people of working age in developed countries [3]. DR is generally categorized into the classes of non-proliferative DR (NPDR) and proliferative DR (PDR). Signs of NPDR include microaneurysms, cotton wool spots, hard exudates and hemorrhages [3]. Depending on the presence of such features the severity of NPDR can be categorized into three stages of mild, moderate, and severe [50]. As the disease progresses to its proliferative stage retinal ischemia, caused by inadequate blood supply to the retina, can trigger abnormal vessel changes, such as venous beading, intra-retinal microvascular abnormalities (IRMA) and new vessel growth. The development of new vessel-like regions is called neovascularization and it can lead to acquired blindness if untreated. Based on the position of neovascularization in the retina, it can be classified into two categories. If the new-vessel-like structures occur on or within one optic disc (OD) diameter centered at the papilla, then they are classified as neovascularization at the disc (NVD), otherwise they are classified as neovascularization elsewhere (NVE).

Patients with PDR are mostly treated with laser surgery, otherwise known as scatter laser treatment, which aids shrinking of abnormal blood vessels [110]. A few thousand laser burns are placed in areas of the retina away from the macula, thus causing the

fine abnormal vessels to shrivel. Laser surgery is found to be more effective for vision restoration on patients where the fine blood vessels have not begun to bleed [110]. Thus, early detection of PDR significantly reduces the chances of acquired blindness. However post surgery, the visible laser scars can enlarge considerably, or sub-retinal fibrosis can occur. Fibrosis generally refers to the response of a tissue to injury, such as laser treatment, ischemia or neovascularization [111]. In such instances, the retinal surface may bear several bright circular patches depicting the laser scars, or bright elongated resolution of damaged tissues due to fibrosis. Thus, for accurate screening of images with PDR from normal images without DR, it is necessary to identify bright abnormal regions such as laser scars or fibrosis, and vessel abnormalities such as NVD and NVE.

Even though there are many screening programs in effect for the detection and diagnosis of NPDR, only early signs of PDR warrant preventive measures to stop the progression of PDR into later stages which can ultimately lead to acquired blindness [34]. Currently, there is a need for improved detection, diagnosis, and analysis of changes in the retina due to NPDR as well as PDR in screening programs. Although a lot of NPDR screening and detection algorithms have been developed till date, significantly less attention has been focused on detecting symptoms of PDR. One existing work in [112] detects instances of NVD by classification of the ridge lines obtained after watershed transform is applied on the blood vessels in the OD region. Fifteen features are used for classification of NVD ridge lines using the support vector machines (SVM) classifier. This method has a high accuracy for detecting new vessel-like regions at the OD that are clinically relevant. However, the features described in this chapter are not generalizable for detecting NVE or other symptoms of PDR. Another work in [50] monitors the openness of the major temporal arcade on 11 images from the publicly available STARE data set [15] for PDR prognosis. This method limits the analysis on images with a centered OD and is not clinically significant due to the small data set under analysis. Another approach in [113] performs fractal analysis at the vessel branching points on 27 fluorenscein labeled images to detect instances of neovascularization. This method analyzes a small data set and relies on fluorenscein images rather than funds images, which is undesirable for automated screening systems. Some other approaches rely on adaptive thresholding techniques for extraction of blood vessels from fundus images, but the detection of neovascularization after the extraction of blood vessels is

not presented [114]. In this chapter, we present a novel method that detects the various manifestations caused by PDR using structural features. This method is tested on 170 images from a public and local data set, and found to have a PDR screening accuracy of 93%.

This chapter makes three key contributions. First, four discriminating structural features are identified for detecting abnormal regions that appear as manifestations of PDR. These features combine basic structural properties such as major axis length, minor axis length, area, convex area, filled area and perimeter and aid identification of certain criteria for abnormal vessel region and bright region detection from fundus images with varying fields of view (FOV) and illumination. The proposed method for determining parametric thresholds for PDR detection is a novel approach. Second, a novel feature is identified as the number of vessel segmented regions obtained after performing watershed transform on the vessel region in the OD neighborhood. This feature discriminates images with NVD from the images without NVD. Third, a novel NVE detection algorithm is described that detects small and large hemorrhage regions in the vicinity of blood vessels using fundus images. This NVE detection algorithm utilized iterative identification of vessel segments followed by a structural feature-based decision making process that separates the NVE segments from the vessel segments.

The organization of this chapter is as follows. In Section 6.2, the proposed PDR detection algorithm is presented. In Section 6.3 the experimental results of PDR screening and identification of NVD and NVE are presented. Conclusions and discussion are presented in Section 6.4.

6.2 Materials and Method

In this chapter, we propose a novel rule-based abnormality detection algorithm for screening images with PDR from normal fundus images and locating the abnormalities on images with varying FOV, contrast and illumination intensities. The first step for abnormality detection is separation of the various regions of interest. Since detection of NVD entails analysis of blood vessels in the OD region while detection of NVE entails analysis of the blood vessels other than the OD region, hence the first processing step involves detection of the OD region neighborhood as the region where the reddest and

brightest regions of the fundus image intersect under some vessel intensity and region compactness constraints using the *Minimum Intensity Maximum Solidity (MinIMaS)* algorithm described in [10]. The OD neighborhood region masks ($\hat{D}$) detected by the *MinIMaS* algorithm are shown in Fig. 6.1.

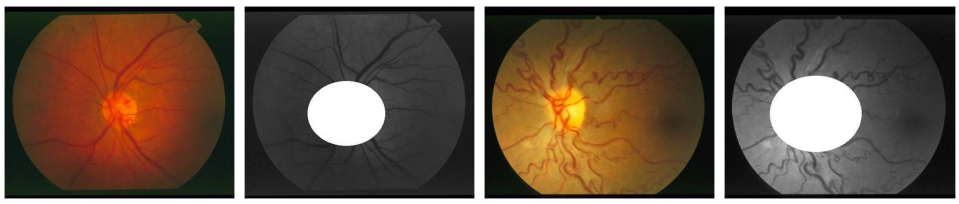

(a) (b) (c) (d)

Figure 6.1: Automated OD detection using the *MinIMaS* algorithm. (a) (c) Actual fundus image from STARE data set. (b) (d) Segmented OD mask $\hat{D}$ superimposed on the green plane of the actual image.

Once the OD region mask is extracted, bright retinal abnormalities corresponding to laser scars and fibrosed tissues are detected in the fundus images under test such that all the images containing such bright abnormalities are considered as abnormal images with some degree of PDR that must be inspected manually by a specialist for further assessment. Following the detection of bright abnormalities, the blood vessel structure is analyzed in the OD neighborhood region for detection of dense blood vessels indicating NVD. Finally, blood vessels are analyzed in the regions apart from the OD neighborhood to detect instances of NVE. Several structural features were examined to detect the retinal abnormalities such as: area, perimeter, orientation, eccentricity, extent etc. The most discriminating features for each vessel or bright region 'e' are computed using the estimates of the major axis length (Φ), minor axis length (Ψ), area (A), perimeter (P), area of convex hull bordering the region (C), and area by filling all the 'holes' within the region (F). These four most discriminating features analyzed for each region 'e' are defined as follows:

1. $\Delta_1(e)$- Roundedness: the ratio of the major to minor axis length of the region ($\frac{\Phi(e)}{\Psi(e)}$). Since laser scars are mostly circular in shape, they have a low roundedness

value close to unity. Fibrosed tissues and hemorrhages caused by neovascularization and more elliptical in structure and hence they have a high roundedness value.

2. $\Delta_2(e)$- Solidity: the ratio of the area to the convex hull bordering the region ($\frac{A(e)}{C(e)}$). Laser scars are convex structures and hence they have a high solidity close to unity. Fibrosed tissues regions may be convex or concave and hence solidity values can vary between 0.4 to 1. NVE regions generally have high solidity.

3. $\Delta_3(e)$- Filled-rate: the ratio of the area to the filled area ($\frac{A(e)}{F(e)}$). Laser scars and fibrosed tissue regions are large solid structures without any 'holes' in them, and hence they have a high filled-rate ratio. NVE regions connected to fine blood vessels appear to have holes in them and hence NVE regions have a low filled-rate ratio.

4. $\Delta_4(e)$- Compactness: the ratio of the area to the perimeter of the region ($\frac{A(e)}{P(e)}$). This feature detects compact concave regions. Laser scars have small areas and hence they have a small value for compactness. Fibrosed tissue regions have large area, but comparatively small perimeter when compared to exudate regions that have a comparatively larger perimeter due to the tattered edges. Thus, fibrosed tissue regions have a large compactness that help to distinguish them from exudate regions and false regions around the blood vessels that get extracted due to contrast variations. Also, NVE regions have high compactness.

The method of extracting bright and vessel regions whose features are then extracted and examined to detect laser scar and fibrosed tissue, NVD and NVE are described in the following subsections. Using a training set of PDR and normal images, a range of threshold values can be determined for each of the four discriminating features mentioned above corresponding to a bright or vessel regions that are indicative of PDR. Once the threshold values for these features are determined, the performance of abnormality detection on the test set of images are analyzed. The proposed method is tested with images from a public data set and a local data set. The images in both the data sets are described below.

- STARE: This public data set contains images with size 700x605 pixels and 35^o

FOV. 22 images from this data set have PDR while 40 images are normal without any signs of DR. To train the abnormality detection modules described in the following subsections, 3 PDR images with names [im0232, im0356, im0340] and 2 normal images with names [im0198, im0216] are used. The trained algorithm is then tested on the remaining 19 abnormal images with PDR and 38 normal images.

- Local: Fundus images with $30^o - 50^o$ FOV are imaged using the Topcon camera from 45 patients with PDR at the University of Minnesota, Department of Opthalmology. For each patient, 1-2 images are selected per eye for analysis. A total of 117 images with PDR are collected. All imaged patients neither had any prior record of laser surgery nor did they have a history of severe NPDR. All images have significant neovascularization and automated location of these instances will aid laser surgery and follow up treatment. To train the abnormality detection modules, 4 images from the first patient are used. The trained algorithms are then tested on the remaining 113 images.

6.2.1 Detection of Laser Scars and Fibrosis

As a pre-processing step, the green plane of each color fundus image is resized to [500x500] and the pixel intensities are scaled in the range [0,1], followed by contrast enhancement, resulting in image I. Next, I is morphologically eroded using a circular structuring element of radius 15, followed by image reconstruction. This reconstruction operation enhances the compactness of brightly illuminated regions. The reconstructed image is then subtracted from I, scaled in [0,1], and subjected to contrast enhancement to yield a morphologically transformed image I_m.

Since laser scars appear as bright retinal patches away from the OD region, hence the a mask is created for the retinal regions other than the OD region by combining the background fundus mask (g) with the OD neighborhood region mask ($\hat{D}$) in (6.1). Next, the morphologically reconstructed image is thresholded at pixel value 'ω' to extract thresholded bright regions in the masked retinal region in image T using (6.2). The threshold pixel value 'ω' is computed adaptively for each image using the Otsu's threshold function applied to image I_m.

$$g' = g \circ (1 - \hat{D}) \tag{6.1}$$

$$T = [(I_m \circ g') > \omega, |r \subseteq T]. \tag{6.2}$$

Corresponding to each bright retinal region 'r' in the thresholded image T, the four discriminating features $[\Delta_1, \Delta_2, \Delta_3, \Delta_4]$ are computed. The threshold ranges for these discriminating features are determined using the training set of images from the STARE data set. Laser scar regions 'r' are detected as small, circular, solid bright regions if $[1.5 \leq \Delta_1(r) \leq 2.5]$, and $[\Delta_2(r) > 0.8]$ and $[A(r) > 1000]$. If more than 5 such regions are detected in any image, the image is considered to have laser scars due to PDR. A fibrosed tissue region 'r' is detected as a bright region with large area, elliptical structure with high filled-rate and compactness if $[A(r) > 1000]$ and $[2.5 \leq \Delta_1(r) \leq 3.5]$ and $[\Delta_3(r) > 0.96]$ and $[\frac{\Delta_4(r)}{\max \Delta_4} > 0.95]$.

The steps for detecting the bright abnormal regions corresponding to laser scars and fibrosis for an image with PDR is shown in Fig. 6.2. In this training image, more than 5 laser scar regions are detected and one fibrosed tissue region is detected, and hence this image is identified as abnormal with PDR. The thresholded bright regions extracted for a normal image is shown in Fig. 6.3. In this example, no laser scar regions or fibrosed tissue regions are extracted and hence the image is identified as normal.

6.2.2 Detection of NVD

NVD causes dense blood vessel structure in the OD region. Thus for NVD detection in any fundus image, the nature of blood vessel density within 1-disc diameter from the papilla needs to be analyzed. All images from the STARE data set do not contain the OD. However, in the images with OD, the average diameter of the OD in the resized image I is found to be 90 pixels. Since the OD neighborhood region detected by the *MinIMaS* algorithm has variable diameter, hence to aid generalization, for all images with OD in the STARE data set, the OD neighborhood region mask is resized at the center to extract a new circular OD neighborhood region mask with radius 90 pixels. In images without OD, NVD is not detected.

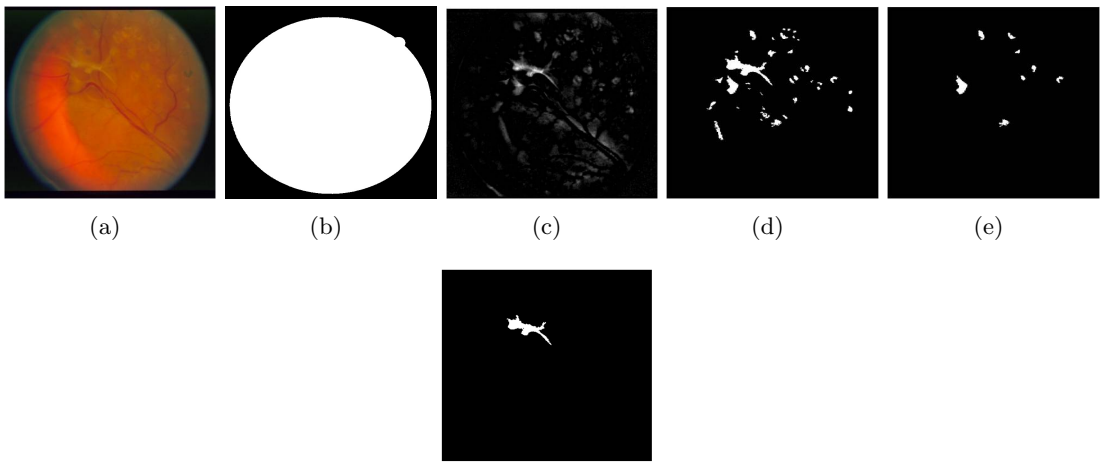

(a) (b) (c) (d) (e)

(f)

Figure 6.2: Steps for detecting laser scars and fibrosis. (a) Fundus image from STARE data set with PDR. (b) Fundus mask 'g'. (c) Morphologically reconstructed bright regions in image I_m. (d) Thresholded bright regions in image T. (e) Regions satisfying the laser scar features. (f) Region satisfying the fibrosis features.

For images with OD, an image with the blood vessel regions enhanced is extracted by applying tophat-transform to the negative of image I. For the tophat transform, 12 linear structuring elements each of length 15 pixels and 1 pixel width and angles incremented by 15^o from 0 through 180^o are convolved with the negative image [115] [12]. The length of 15 pixels for the linear structuring element is chosen to approximately fit the diameter of the biggest vessels in the images [12]. For each pixel location, the transformed pixel with the highest intensity is selected, thereby resulting in vessel enhanced image I_v. This vessel enhanced image is thresholded using a pixel value determined by the Otsu's function, thereby extracting the blood vessels in image V. The OD mask $\hat{D}$ is then applied to the extracted blood vessel image followed by watershed transform of the image $[I_v \circ V \circ \hat{D}]$ [38]. The watershed transform divides the blood vessels in the OD region into smaller regions based on the intensity variations in the vessel enhanced image. For an image with NVD, fine vessel-like structures caused by neovascularization form a thick mesh of vessels within the OD region. These fine vessel-like structures induce a large number of small segmented vessel regions by the watershed transform.

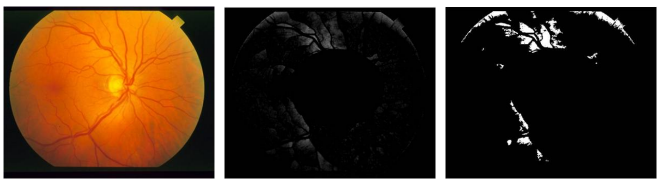

(a) (b) (c)

Figure 6.3: Performance of the laser scar and fibrosis detection module on normal images. (a) Normal image without PDR from the STARE data set. (b) Morphologically reconstructed bright regions in the retinal region, i.e., image $[I_m \circ g \circ (1 - \hat{D})]$. (c) Thresholded bright regions in image T. There are no regions in T that satisfy the laser scar or the fibrosis features.

However, for normal images, the number of watershed segmented regions in and around the OD region is found to be significantly small. Using the training set of images from the STARE data set, we observe that images with NVE have more than 130 segmented vessel regions while normal images have less than 120 segmented vessel regions by the watershed transform. Examples of segmented vessel regions by watershed transform on the training images from the STARE data set are shown in Fig. 6.4. Thus, for all test images if the OD exists, and if the number of segmented vessel regions is significantly large, the fundus image is identified to be abnormal with PDR.

6.2.3 Detection of NVE

NVE detection is the most challenging problem for automated PDR detection algorithms. While some fundus images can have several small hemorrhages close to the blood vessels, others may contain few very large hemorrhage regions. For images from the STARE data set, if at least one region with NVE features is detected, then that image is identified as abnormal with PDR. Otherwise, the image is identified as normal. However, for images from the local data set, it is already known that all images contain PDR, and hence the NVE feature thresholds values are varied to detect all regions in the fundus image with NVE features.

For NVE detection, the entire blood vessel regions need to be separated into smaller segments and analyzed for their structural features. To facilitate detection of small

vessel segments, the iterative vessel segmentation algorithm defined in [116] is used. In this iterative algorithm, the vessel enhanced image I_v is used to extract the bright vessel regions by iteratively varying the threshold. First, the *major vessels* (V_0) are extracted by thresholding image I_v for pixels greater than 0.5, and retaining the regions with area greater than 1000 pixels in (6.3). Thus, V_0 is the segmented vessel estimate (V_t) at iteration $t = 0$. Next, the following steps are iteratively performed:

For each iteration t, the pixels from the existing vessel estimate V_t are removed from image I_v and the remaining image is contrast adjusted resulting in residual image R_t in (6.4). This image R_t is thresholded at pixel value $\phi_1(t)$ to extract a binary image V_{R_t} containing new vessel regions that have an area of at least 10 pixels in (6.5). However, it is desirable for the segmented vessel to have a continuous structure and hence it is imperative to fill any gaps or holes between the existing vessel estimate V_t and the newly identified vessel pixels in V_{R_t}. Thus, the pixels in V_t and V_{R_t} are added to vessel enhanced image I_v followed by rescaling the pixels in [0,255], resulting in base image B_t in (6.6). This image B_t is then region-grown with a threshold pixel value ($\phi_2(t)$) that is a function of the iteration number in (6.7). The image obtained at the end of the regiongrow operation [38] is the new iterative vessel estimate (V_{t+1}). The iterative thresholds for $\phi_1(t), \phi_2(t)$ are given in (6.8).

$$V_0 = [(I_v > 0.5) | A(r' \subseteq (I_v > 0.5)) > 1000]. \tag{6.3}$$

$$\forall t > 0, R_t = [I_v - V_{t-1}]. \tag{6.4}$$

$$V_{R_t} = [R_t > \phi_1(t) | A(r'' \subseteq (R_t > \phi_1(t))) > 10]. \tag{6.5}$$

$$B_t = \text{scale}(\{V_{R_t} \cup V_t\} + I_v \in [0, 255]. \tag{6.6}$$

$$V_{t+1} = \text{regiongrow}(B_t, \text{seed} = 255, \text{threshold} = \phi_2(t)). \tag{6.7}$$

$$\text{Where}, \phi_1(t) = 1 - (0.05 * t), \phi_2(t) = 205 + (t-1)^{1.8}. \tag{6.8}$$

For NVE detection, the iterative identification of new vessel regions is continued till the vessel segments being iteratively identified become significantly small. For images from the STARE data set, 5 iterations are enough to identify NVE regions, while for the Local data set, vessel segments from 7 iterative steps are analyzed. Using the

iterative approach, small vessel segments are identified in image V_{R_t}. Next, for each region 'r''' in image V_{R_t} the discriminating features $[\Delta_1, \Delta_2, \Delta_3, \Delta_4]$ are computed. An NVE region is detected as a large, wide, elliptical region with with some holes and significant compactness if, $[A(r'') > a]$ and $[\Psi(r'') > p]$, and $[\Delta_1(r'') > \delta]$, and $[0.5 \leq \Delta_3(r'') \leq 0.96]$ and $[\Delta_2(r'') > 0.4]$ and $[\frac{\Delta_4(r'')}{\max \Delta_4} > 0.8]$. The thresholds $[a, p, \delta]$ for the STARE and Local data sets are [100, 12, 3], and [30, 10, 1.2], respectively. If a region from image V_{R_t} is detected as NVE, it is not added to the existing iterative vessel estimate. Only the regions that are not detected as NVE regions are added to the vessel estimate. In this way a significant portion of the blood vessels are extracted at the end of 5-7 iterative steps and the NVE regions are separated from the blood vessel regions.

For a training image with PDR from the STARE data set, the NVE region detected in first iterative step is shown in Fig. 6.5. Iterative detection of vessel segments from a normal training image from the STARE data set is shown in Fig. 6.6. In each iterative step, the regions with maximum Δ_1, Δ_4 and minimum Δ_3 are illustrated by the circular regions. For the vessel segments from the normal image, all the NVE feature criteria are never satisfied, thus identifying this image as a normal image free from NVE.

6.3 Results

The robustness of the proposed method for detecting images with PDR is analyzed on the test images from the STARE and Local data set. For the STARE data set, the normal images without any pathology that were detected as normal by the proposed method are true negatives (TN), while the images that had PDR and were identified as abnormal with PDR by the proposed method are true positives (TP). The images with PDR that are falsely identified as normal are false negatives (FN), while the normal images falsely identified as abnormal with PDR by the automated system are false positives (FP). Based on the number of TP, TN, FN, FP images, the sensitivity (SEN) and specificity (SPEC) of the proposed method for screening patients with PDR and separating them from the normal images is given in Table 6.1.

In Table 6.1 we observe that the proposed method fails to detect instances or IRMA in one abnormal image, i.e., $FN = 1$, and over detects watershed segmented vessel

Table 6.1: Performance of screening PDR images from normal images from the STARE data set.

Actual**Automated**	**PDR**	**Normal**	**Metrics**
PDR	$TP = 18$	$FN = 1$	$SEN = 94.74\%$
Normal	$FP = 3$	$TN = 35$	$SPEC = 92.11\%$

regions signifying NVD in 3 normal images, thus causing $FP = 3$. These false detections can be further reduced by increasing the number of training images and by ensuring uniformity in the level of detail captured by each image by maintaining the same angle of the retina when the fundus image is taken. Since the images from STARE data set have a wide variety of details captured in them due to the changing angle of the retinal shot, hence the present false detections were unavoidable. In spite of four incorrect detections, the proposed system achieves a PDR screening accuracy of 92.98%.

For detection of NVD on the images from the STARE data set, the number of segmented vessel regions by the watershed transform for each image is shown in Fig. 6.7. Here, we observe that the number of segmented vessel regions for the images with PDR is significantly higher than the number of segmented regions in normal images. The mean and standard deviation of the number of segmented vessel regions for images with PDR and normal images is given in Table 6.2. We observe that the average number of segmented vessel regions for PDR images from the STARE and Local data set and significantly high when compared to the normal images. It is important to note that the number of segmented vessel regions was chosen as a discriminating feature for NVD detection after analyzing its impact in comparison with other features such as the mean and variance of the total number of vessel pixels in the OD region, or the length of the ridge pixels after watershed transform [34].

For all the 117 images with PDR from the Local data set, instances of NVD and NVE are detected in all the images. Examples of NVD detection on two images from the local data set are shown in Fig. 6.8. We observe that the number of segmented vessel regions is consistently high for the images with NVD from the STARE and Local data set.

Finally, examples of NVE detection from the Local data set images are shown in

Table 6.2: Analysis of the mean and standard deviation of the number of segmented vessel regions by watershed transform on normal and abnormal images with PDR from the STARE and Local data set.

Category	mean(# of vessel regions)	std. dev. (# of vessel regions)
STARE		
PDR	138.41	96.37
Normal	72.12	31.55
Local		
PDR	182.63	89.59

Fig. 6.9. Here, we observe that small vessel-like structures in close vicinity of the blood vessels and large neovascularization regions are equally detected by the proposed method.

6.4 Conclusions and Discussion

In this chapter, we have proposed rule-based PDR detection algorithms that are consistent across fundus images with varying FOV and successful in screening PDR images from normal images along with detecting laser scars, fibrosed tissues and neovascularization in the OD region and elsewhere. Four structure-based features are identified that are capable of discriminating laser scars, fibrosis and NVE from false positives. Once trained for a particular FOV, the proposed algorithms can screen and locate manifestations of PDR using fundus images.

The first module of the proposed method detects laser scars and fibrosis. While laser scars are detected as solid circular compact bright regions with less 'holes', fibrosis is detected as elliptical shaped structures with certain compactness constraints. It is important to note that fundus images with ocular histoplasmosis or choroidal inflammation can appear similar to images with laser scars. In such cases, manual screening is necessary. The proposed algorithm for abnormal bright region detection will identify such images with choroidal abnormalities as abnormal and hence they will be subjected to manual assessment afterward.

Detection of NVD involves counting the number of segmented vessel regions after

watershed transform is applied to the vessel enhanced image in the OD region. Based on the threshold for the number of segmented regions the PDR screening performance will vary. In this chapter we observe a significantly high difference between the number of segmented vessel regions in abnormal images with PDR and in normal images. Future efforts will be directed towards manually annotating the new vessel-like structures and assessing the severity of NVD by using feature-based classifiers.

For NVE detection, small vessel segments are iteratively identified and analyzed for NVE. This iterative vessel segmentation algorithm has two degrees of freedom based on the two thresholds $[\phi_1(t), \phi_2(t)]$. For future data sets, these thresholds can be varied to increase or decrease the resolution and structure of the newly identified vessel structures per iteration. Future efforts will be directed towards manually annotating the regions with NVE and analyzing the contribution of structural features for classifying NVE regions. Also, the performance of the proposed method for automated PDR severity detection will be analyzed in future works. The proposed algorithm can also be integrated with existing NPDR screening algorithms in [3] for enhanced prioritization and resourcefulness of present day eye-care delivery.

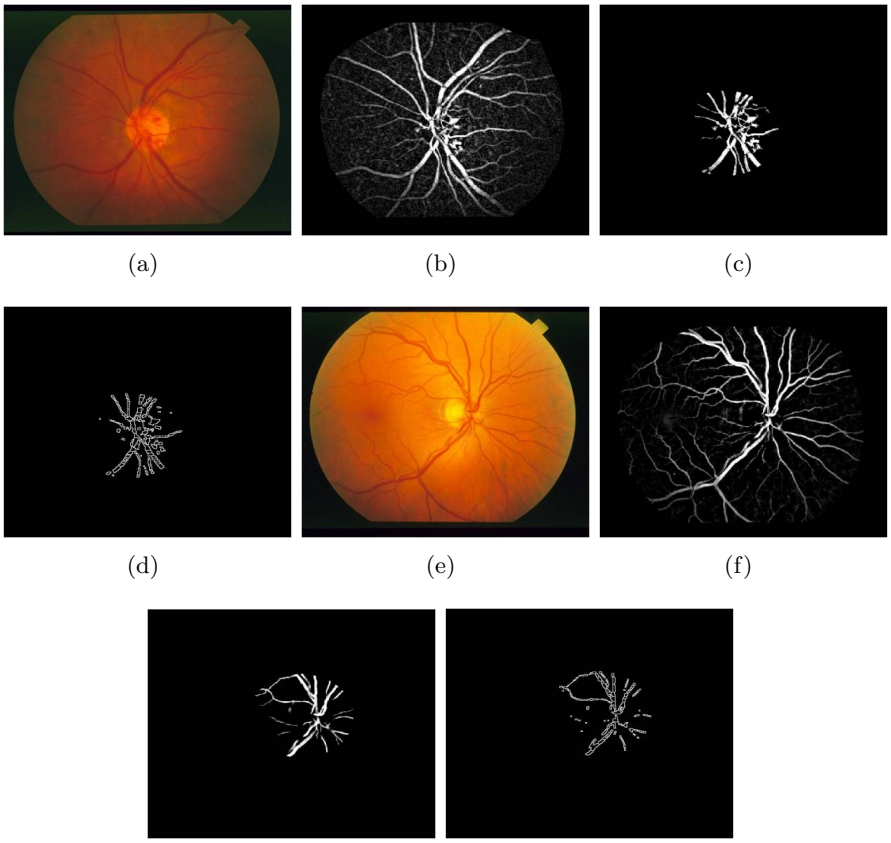

Figure 6.4: Segmentation of vessel regions by watershed transform for NVD detection on an image with NVD and a normal image from the STARE data set. (a) Image with NVD. (b) Vessel enhanced image obtained after tophat transform (I_v). (c) Vessels within 1-disc diameter, centered at the papilla. (d) Segmented vessel regions after watershed transform. (e) Normal image without NVD. (f), (g), (h), correspond to images (b), (c), (d), respectively, for the normal image.

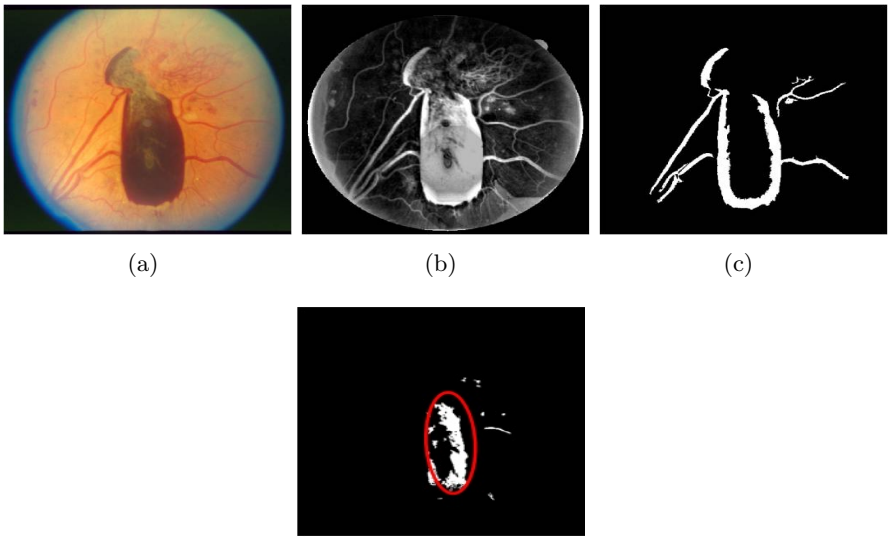

(a) (b) (c)

(d)

Figure 6.5: Example of NVE detection from an image with PDR from the STARE data set. (a) Fundus image. (b) Vessel enhanced image (I_v). (c) Initial vessel estimate (V_0) (d) Vessel residual image after first iteration V_{R_1}. The region marked by the red circle satisfies all the NVE features.

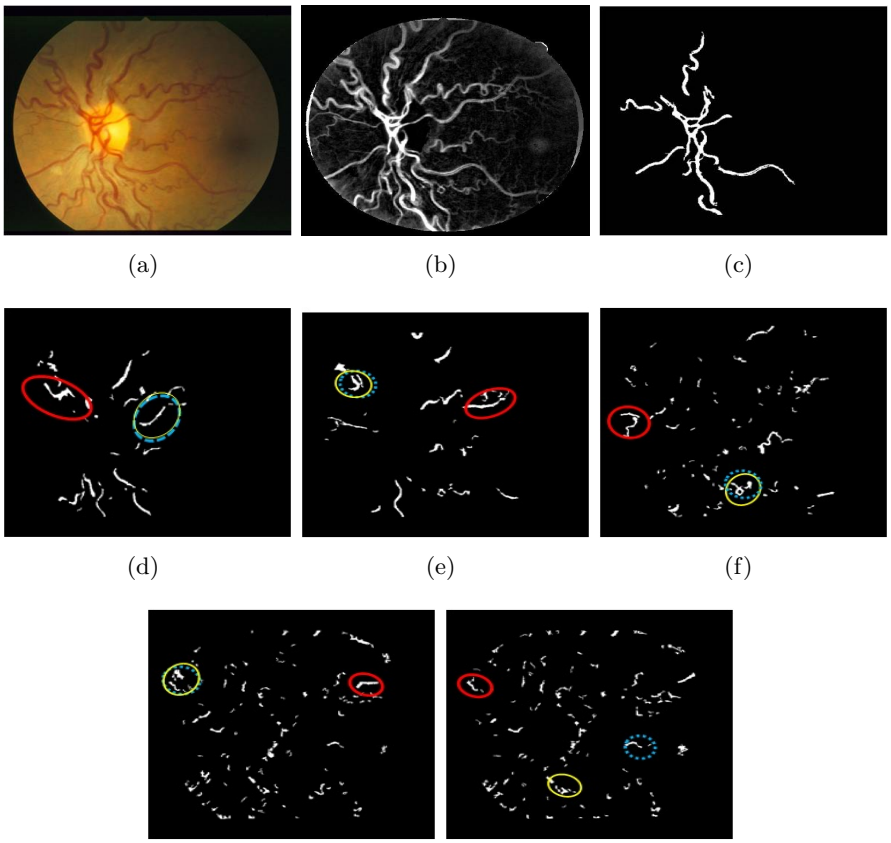

Figure 6.6: Performance of NVE detection module on a normal image from the STARE data set. (a) Normal fundus image. (b) Vessel enhanced image (I_v). (c) Initial vessel estimate (V_0) (d) Vessel residual image after first iteration V_{R_1}. (e) Vessel residual image after second iteration V_{R_2}. (f) Vessel residual image after third iteration V_{R_3}. (g) Vessel residual image after fourth iteration V_{R_4}.(h) Vessel residual image after fifth iteration V_{R_5}. In images (d) (e) (f) (g) (h) the region in red circle satisfies the NVE criterion regarding feature Δ_1, the region in yellow circle satisfies the NVE criterion for feature Δ_3, and the region in blue dashed circle satisfies the NVE criterion for feature Δ_4. Since no region in any iteration satisfies all the three criteria, hence no NVD regions are detected for this image.

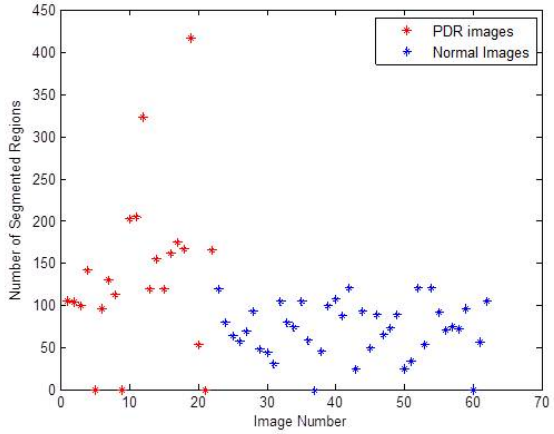

Figure 6.7: Distribution of the number of segmented vessel regions by watershed transform on images with PDR and normal images from the STARE data set. The number of segmented vessel regions for the normal images are significantly different from that of the images with PDR.

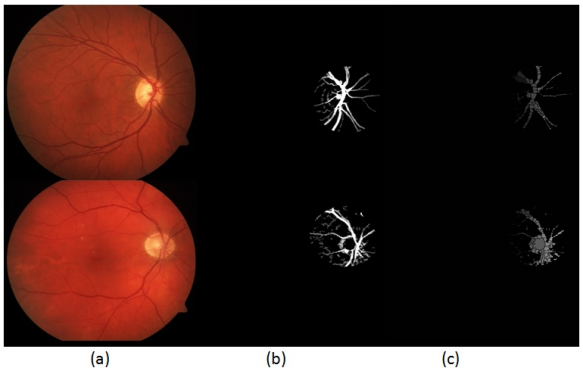

Figure 6.8: Examples of NVD detection on images from the Local data set. (a) Fundus image. (b) Enhanced vessels in the 1-OD diameter region. (c) Segmented vessel regions by watershed transform.

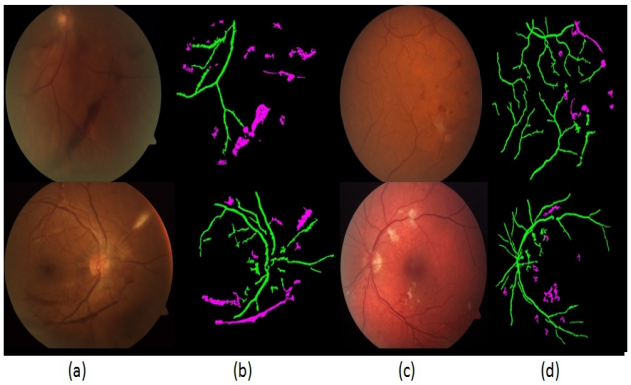

Figure 6.9: Examples of NVE detection on images from the Local data set. (a) (c) Fundus images. (b) (d) The corresponding blood vessels extracted are denoted in green, while the NVE regions detected are denoted in magenta.

Chapter 7

Automated Segmentation of Optical Coherence Tomography Images

7.1 Introduction

Diabetic macular edema (DME) is a leading cause of vision loss in patients with diabetes. The World Health Organization estimates that by the year 2020, there will be 75 million blind people and 314 million partially blind people in the world [117].While treatments are available, including intravitreal injections and macular laser therapy, not all patients respond to these. Currently, there are no reliable methods for predicting patient response to therapy. Therefore, analysis of the patient images prior to treatment may allow the development of measures to predict patient response. Optical Coherence Tomography (OCT) has been widely used to assess macular diseases, and it has enabled analysis of the extent of disorganization in the sub-retinal layers due to DME [118] [119]. Sub-retinal layer disorganization refers to the variation in the underlying retinal micro-structure due to the presence of cystoid regions or due to disruptions in the cellular architecture of the sub-retinal layers due to pathology [120]. For each patient's eye under analysis, a stack of images centered at the macula are acquired, such that reconstruction of the sub-retinal surfaces from each image belonging to the OCT

image stack aids locating disease-related abnormalities in the retinal micro-structure for follow-up treatment procedures. The goal of this chapter is to automatically segment the sub-retinal surfaces and layers in OCT image stacks from normal patients and abnormal ones, with DME, such that thickness maps corresponding to the sub-retinal layers can be further analyzed for their clinical relevance to the severity of DME.

Reliable OCT automated segmentation systems are necessary for faster retinal evaluations, since manual segmentation can take up to 12 minutes per image [121]. Several automated OCT sub-retinal layer segmentation algorithms have been developed so far with varying accuracies on normal and glaucomatous images [122]. However, no automated segmentation algorithm has been reported so far that detects the inner sub-retinal layers of the retinal micro-structure. One existing work in [123] extracts only three significant sub-retinal surfaces to analyze the mean thickness of the inner layers in the OCT images with DME. In this chapter, we extract not only the significant surfaces that suffer minimal changes due to pathology as shown in [123], but we also extract the inner sub-retinal surfaces that suffer drastic changes due to DME. The proposed work can significantly benefit clinical trials that interpret the changes in DME retinal thicknesses in response to therapy.

Existing studies on OCT images from patients with DME have shown that clinical edema causes the tomographic thickness to exceed 1.33 times the normal thickness values [124]. So far, significant relationship has been found between retinal thickness and visual acuity [124]. Other studies in [125] have shown strong correlation of visual acuity with IS/OS junction integrity, and no correlation between cystoids macular edema and visual acuity. Another study shows that the macular thickness in clinically undetectable eyes is $228\pm53\ \mu m$ [126]. In this chapter we propose an automated system that estimates the retinal layer thickness with significant reliability. Such an automated system can lead to faster and more efficient detection and treatment of patients with DME if the macular thickness for the particular patient is found to exceed the clinically acceptable levels. Additionally, such an automated system can be used for clinical trials to analyze more metrics other than the macular thickness for their clinical relevance to visual acuity.

The proposed automated OCT segmentation algorithm involves two key steps. In the first step, speckle noise introduced by the imaging systems is removed from the images. In the second step, the denoised images are subjected to model-based segmentation.

In prior efforts for denoising OCT images in the first step, OCT speckle suppression has been accomplished by median filtering [127], discrete wavelet transforms [128] and dual tree wavelet transforms [129]. In another work [130], multi-scale sparsity based tomography denoising is performed by sub-sampling the noisy OCT image, followed by dictionary parameter training, k-means clustering and final image restoration. It is observed that the sparsity based denoising approach [130] is most useful in signal retrieval from speckle noise in unaveraged OCT fames from Bioptigen SDOCT systems. However, images obtained from Spectralis OCT (Heidelberg Engineering, Germany) have built-in stabilization and averaging systems that produce significantly high SNR in the OCT images. In this chapter we analyze images from Spectralis OCT, and hence we compare the performance of the proposed Wiener deconvolution algorithm with Fourier-domain based noise variance estimator with denoising performance of the complex dual tree wavelet transform method in [129]. This comparison aids analysis regarding the importance of speckle noise removal on automated segmentation algorithms.

For the second step of automated sub-retinal surface and layer segmentation, some prior works rely on edge detection methods searching for peaks of gradient changes in column wise pixel intensities followed by interpolation [131] or edge classification [132] [133]. Such edge detection methods, however, suffer from large segmentation errors when the image pixel intensities are inconsistent and in the presence of underlying pathology. Active contours based methods were explored in [134] with a two-step kernel based optimization scheme for sub-retinal layer segmentation. Another well known graph-cut segmentation method separates a 3-D composite image into sub-retinal layers by finding a minimum cost close set in a 3D graph [135]. Modifications to this method have been used to segment the optic nerve head in [122], and an alternative segmentation approach using dynamic programming has been explored in [136] [123]. The major drawback of such graph-based 3-D segmentation methods is that they suffer from high complexity and are restrictive in their assumptions.

This chapter has three key contributions. The first contribution is the comparative analysis of the existing wavelet-transform based denoising method with a Fourier-domain structural error based denoising method presented in our previous work in [137]. In this previous conference paper, the concept of noise parameter estimation for Wiener deconvolution was described. In this chapter, we analyze the importance of

image denoising on automated sub-retinal surface and layer segmentation process. Our analysis demonstrates that although wavelet-based denoising approach achieves a high peak signal to noise ratio (PSNR) of about 28dB, it smoothens the sub-retinal layers considerably, thereby incurring two times more sub-retinal surface and layer segmentation error when compared to the proposed Fourier-domain based denoising method. The second contribution is a novel multi-resolution iterative sub-retinal surface segmentation algorithm that is adaptive and robust to normal OCT images and images with DME. An initial version of this iterative algorithm was presented in the conference paper [137], where 358 images from 15 diabetic and 2 healthy patients were subjected to the proposed Fourier-domain based automated denoising followed by segmentation. The segmentation algorithm in the conference paper was a preliminary version of the method proposed in this work without any automated segmentation performance analysis. In this chapter, the segmentation algorithm has been further fine tuned to segment images normal images and images with macular edema, and the segmentation performance for sub-retinal surface detection and sub-retinal thickness estimation has been extensively analyzed thereafter. The third contribution is the novel assessment of sub-retinal layer thickness maps that are generated using the proposed automated segmentation system on the normal and abnormal OCT image stacks. The proposed automated denoising and segmentation system is capable of extracting inner and outer sub-retinal layers in normal and abnormal images with significant reliability (i.e., correlation coefficient $(r) > 0.7, p < 0.001$), and hence the inner sub-retinal layer thickness maps can be generated and analyzed to asses progression of pathology. We introduce a novel metric that is based on the area of irregularity introduced in the inner sub-retinal layer thicknesses by DME. This metric can be clinically analyzed for its correlation to visual acuity, or it can be used to monitor the response of patients with DME over time.

The organization of this chapter is as follows. In Section 7.2, the method and materials used to analyze the proposed automated segmentation system are presented. In Section 7.3 the experimental results of automated sub-retinal surface and layer segmentation are presented. Conclusions and discussion are presented in Section 7.4.

7.2 Materials and Method

Automated analysis of sub-retinal layers from OCT image stacks involves three key steps. In the first step, each image from the stack is denoised to remove significant speckle noise introduced by the imaging systems [131]. In the proposed segmentation system a Fourier-Domain structural error metric proposed in [118] is used to estimate the additive speckle noise parameters followed by *Wiener Deconvolution* to obtain a denoised image. In the second step, each denoised image is subjected to automated sub-retinal layer segmentation by multi-resolution high-pass filtering. Seven surfaces corresponding to six sub-retinal layers are thereby extracted. In the third step, the thickness of up to six sub-retinal layers from all images of the OCT stack are extracted and interpolated to generate the sub-retinal layer thickness maps. These thickness maps can then be further analyzed to locate and assess the severity of sub-retinal disorganization caused by DME.

The three steps for automated segmentation of the sub-retinal layer thickness maps are described in the following subsections. From all the OCT data image stacks each OCT image is treated as a separate standalone image while denoising and segmenting the sub-retinal surfaces. This operation of separately segmenting each image without any information regarding the adjacent images from the OCT image stack is different from the existing graph-based segmentation approaches in [135]. Once each image is denoised, 7 sub-retinal surfaces i.e., Surface 1 to Surface 7, and 6 sub-retinal layers that are then segmented are shown in Fig. 7.1. The segmented sub-retinal layers extend from the inner limiting membrane (ILM, Surface 1) to the Bruch's Membrane (BM, Surface 7) surface. The segmented sub-retinal layers as shown in Fig. 7.1 are: the Nerve Fiber Layer (NFL, between Surface 1 and Surface 2), Inner Plexiform Layer and ganglion cell layer combined (IPL, between Surface 2 and Surface 3), Inner Nuclear Layer and outer plexiform layer combined (INL, between Surface 3 and Surface 4), Outer Nuclear Layer (ONL, between Surface 4 and Surface 5), Photoreceptor Inner/Outer Segment (IS/OS, between Surface 5 and Surface 6) and Retinal Pigment Epithelium (RPE, between Surface 6 and Surface 7). Additionally, to analyze the average retinal thickness two more combined layers are analyzed as: the Inner layer, that combines the NFL, IPL, INL and ONL (between Surface 1 and Surface 5), and the Outer layer, that combines

the IS/OS and RPE layers (between Surface 5 and Surface 7).

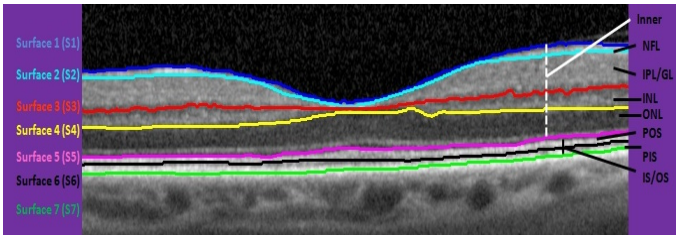

Figure 7.1: Sub-retinal surfaces and layers in OCT images for segmentation. The 7 sub-retinal surfaces are color coded as Surface 1 (Blue), Surface 2 (Cyan), Surface 3(Red), Surface 4 (Yellow), Surface 5 (Pink), Surface 6 (Black), Surface 7 (Green). The sub-retinal layers are: NFL, IPL, INL, ONL, POS, PIS, Inner and IS/OS segments.

The data for assessing the performance of automated OCT segmentation is obtained using the Heidelberg Spectralis Imaging system at the Department of Ophthalmology in the University of Minnesota. OCT image stacks from normal and abnormal eyes with DME are obtained such that each image is averaged over 12-19 frames. Each OCT image has a resolution of 5.88 μm/pixel along the length and 3.87μm/pixel along the width and [1024x496] pixels per image. To evaluate the performance of the proposed segmentation system, each image is manually annotated for all the sub-retinal surfaces. The following two sets of OCT image stacks are obtained corresponding to normal eyes and eyes with pathology.

1. Normal set: This image set comprises of OCT image stacks of the macular region from 10 healthy eyes with 19-25 images per OCT stack. A total of 203 normal OCT images are collected in this set.

2. Abnormal set: This image set comprises of macular OCT image stacks from 15 patients with DME and 19-33 images per OCT stack. A total of 357 images with sub-retinal cysts and layer disorganization are collected in this set. The Surface 6, which is not affected by DME, is not manually marked for images from this data set.

7.2.1 Automated Denoising

Speckle noise removal from OCT images is achieved based on the inherent assumption that the additive noise is Gaussian in nature. The statistical model for a noisy image (I) follows $\psi(I) = \psi(H).\psi(I_d) + \psi(N)$, where, I is the noisy OCT image, H is a 2-D point spread function (PSF), I_d is the noiseless image, N is the additive Gaussian noise and ψ denotes a particular frequency-based or texture-based transform. Some existing OCT image denoising methods in [129] [128] achieve image denoising using the above statistical model with the Wavelet-transform. However, in this chapter, we estimate additive speckle noise using the Fourier-transform as function ψ [137].

The proposed system utilizes the Wiener deconvolution algorithm that reduces the least-square error in Fourier-domain [138] as shown in (7.1).

$$\psi(I_d) = \left[\frac{1}{\psi(H)}\frac{|\psi(H)|^2}{|\psi(H)|^2 + \frac{\Sigma_N}{\Sigma_I}}\right]\psi(I), \tag{7.1}$$

where Σ_N and Σ_I represent the power spectral density of noise and the original noisy image, respectively. Assuming a Gaussian PSF (H) with zero mean and variance 10^{-3}, Σ_N is iteratively estimated for each OCT image by minimizing a Fourier-domain structural error defined in [137]. Once the additive noise variance is estimated using Fourier-domain representations of the noisy and denoised images, the Weiner deconvolution of the noisy image with the estimated noise variance parameters results in the denoised image I_d. This approach of iterative noise parameter estimation in the Fourier-domain followed by Wiener deconvolution is referred as the 'proposed system' in the following sections.

To comparatively assess the importance of speckle noise removal on automated OCT image segmentation, we selected a baseline method of image denoising by the wavelet tree-based approach in [129] [139]. Wavelet-based denoising approaches are known to estimate clean signal coefficients from the noisy ones using Bayesian estimators [139]. While wavelet coefficients with large magnitudes represent edges or texture, coefficients with small magnitude represent the smooth background regions. Thus, OCT image denoising using the wavelet shrinkage method in [129] is achieved in four steps that are: wavelet transform on the noisy image I, estimation of adaptive threshold using the wavelet transform, denoising image I using the estimated threshold, and finally inverse

wavelet transform on the denoised image. The most critical step in this wavelet-based denoising approach is the adaptive threshold estimation. While a low threshold will not produce significant denoising, a high threshold will estimate a signal with a large number of zero coefficients that will correspond to a smoothened image with no edges or texture. To facilitate optimal threshold estimation, soft-thresholding is performed as described by [139]. This method of OCT image denoising using complex dual-tree wavelet transform is referred as 'CDWT' in the following sections. The performance of OCT image segmentation and sub-retinal layer thickness map estimation using the proposed denoising approach and the wavelet-based denoising approach are compared. The pixel intensities of the denoised image is (I_d) is scaled in the range [0,1] before proceeding to automated segmentation.

7.2.2 Automated Segmentation

Every denoised image (I_d) is subjected to multi-resolution iterative high-pass filtering to extract 7 sub-retinal surfaces [137]. Several OCT image segmentation methods that involve edge detection followed by segment linking or gradient search methods have been developed so far [131]. However, most such methods fail in the presence of sub-retinal disorganization owing to pathology. Since the proposed method of sub-retinal surface segmentation overrides the need for interpolation between partially detected line segments, it is robust to normal and abnormal images with pathology.

Each sub-retinal layer in the OCT images has a distinct pixel intensity that is different from the adjacent layers. Also, some sub-retinal surfaces are more distinct than the rest, for instance the top surface of the NFL (Surface 1) or the IS/OS junction (Surface 5) are more distinct than the other surfaces. Thus, to capture each sub-retinal surface separately, it is imperative to look for the most distinct edges/surfaces first, then masking them out, and analyzing the remaining regions for the next most significant surface till all 7 surfaces have been detected. This idea is the basis for the proposed multi-resolution image segmentation approach, where the sub-retinal surfaces are segmented iteratively in decreasing order of their distinctiveness, with the most distinct surface (Surface 1) segmented first and the least distinct surface (Surface 2) segmented the last.

The proposed multi-resolution surface extraction algorithm proceeds in 6 iterative

steps, i.e., $k = [1, 2, ...6]$. In each iterative step 'k' a different source image is used. The source image (I_{s_k}) refers either to the denoised image or the negative of the denoised image, whichever enhances the distinctiveness of the surface of interest. Next, a region of interest is selected for the source image based on the region where the most distinctive edge will lie. This region of interest is denoted by a masked region G_k. Next, the region in source image I_{s_k} that lies within masked region G_k is high-pass filtered in different ways as shown in (7.2). The filtered image (I_k) is then subjected to pixel-level thresholding (Δ_k) and the regions in the remaining image are subjected to a particular decision criterion (C_k) to extract an image (I_{r_k}) with one or more regions in it that satisfy the criterion in (7.3). The top or bottom surface ($Surf_k$) of the region/regions in image I_{r_k} is determined as the segmented surface (S_k) in (7.4).

$$\forall k = [1, 2...6], I_k = HPF_k(I_{s_k} \circ G_k) \tag{7.2}$$
$$\Rightarrow I_k = I_{s_k} \circ G_k - LPF_k(I_{s_k} \circ G_k).$$
$$I_{r_k} = C_k(\Delta_k(I_k)). \tag{7.3}$$
$$S_k = Surf_k(I_{r_k}). \tag{7.4}$$

Corresponding to each iterative step (k), the choice of source image (I_{s_k}), mask for the region of interest (G_k), filter (HPF_k/LPF_k), threshold (Δ_k), decision criterion (C_k) and surface of interest ($Surf_k$) are given in Table 7.1. In most of the iterations, threshold values (Δ_k) are computed using the Otsu's threshold function [140]. Also, depending on the visibility of the vitreous tissue interface, the threshold pixel value for regiongrow operation [38] is varied in the range 230-245, such that, if vitreous tissue surface is significantly bright, then a threshold close to 230 is sufficient, otherwise, a higher threshold value may be required to extract the Surface 1 (S_1).

For an image from the Abnormal data set OCT stack, the proposed iterative surface segmentation algorithm is shown in Fig. 7.2. We observe that due to the multi-resolution nature of the proposed segmentation, the inner sub-retinal surfaces (S_2 to S_4) are correctly detected in spite of the sub-retinal disorganization that occurs due to the presence of large cystoid regions. Also, in Fig. 7.2, we observe that the proposed denoising method retains more surface edge definition at the end of image denoising when

Table 7.1: Iterative parameters for sub-retinal surface segmentation using the proposed multi-resolution high-pass filtering method. These parameters are used in (7.2)-(7.4) to obtain 7 sub-retinal surfaces in 6 iterations.

k	Source (I_{s_k})	Mask (G_k)	Filter (HPF_k/LPF_k)	Threshold (Δ_k)	Criterion (C_k)	$Surf_k$
1	I_d	whole image	HPF_1 =2-D Gaussians, horizontal and vertical	regiongrow (I_1 in [0 255], seed=255, threshold= $\{230-235\}$)	arg max (Area)	S_1 = Top (I_{r_1}), choroid= Bottom (I_{r_1}).
2	$1-I_d$	Between S_1 and choroid	LPF_2 =average [25x25]	pixel values < 0	arg max (Major Axis Length)	S_5 =Top (I_{r_2}), S_7 =Bottom (I_{r_2}).
3	$1-I_d$	Between S_5 and S_7	HPF_3 =contrast enhancement	pixel values >Otsu's Threshold estimated on I_3	-	S_6 =Bottom (I_{r_3}).
4	$1-I_d$	Between S_1 and S_5	LPF_4 =average [25x25]	pixel values >Otsu's Threshold estimated on I_4	arg max (Major Axis Length)	S_4 =Bottom (I_{r_4}), .
5	$1-I_d$	Between S_1 and S_4	LPF_5 =2-D Gaussian, horizontal [10x10]	pixel values >Otsu's Threshold estimated on I_5	arg max (Area)	S_3 =Bottom (I_{r_5}),
6	I_d	Between S_1 and S_3	LPF_6 =average [25x25]	pixel values >Otsu's Threshold estimated on I_6	arg max (Area)	S_2 =Bottom (I_{r_6}),

compared to the CDWT approach, which smoothens the edges close to the choroid. Thus, the CDWT method induces larger surface segmentation errors around the outer layers.

It is noteworthy that in certain OCT images, like the ones with the fovea as shown in Fig. 7.1, while the Surface 1 is always continuous, other surfaces, such as Surface 3 or Surface 2, may appear discontinuous in a normal OCT image. To enable the detection of complete surfaces in such cases, an exception rule is applied to detect all surfaces, apart from Surface 1, that have chances of appearing discontinuous. For this exception rule, the Surface 1 from iteration $k = 1$ is first detected and all its x-coordinates are noted. Next, from iteration 2 through 6 in Table 7.1, for each extracted surface, if the length of the surface is less than 75% of the length of Surface 1, then another region satisfying the criterion (C_k) apart from the region already selected is added to image I_{r_k}. This process is of adding regions is continued till the combined length of all regions in image I_{r_k} is greater than 75% of Surface 1's length. The final detected surface becomes the combination of surfaces from all the regions thus detected in image I_{r_k} .

7.2.3 Sub-retinal Layer Thickness Maps

Once each image from the OCT image stacks are segmented to detect 7 surfaces, the thicknesses of 6 sub-retinal layers are then estimated at every horizontal pixel position. To generate thickness maps for every sub-retinal layer, the thicknesses corresponding to each horizontal pixel coordinate from all images in the OCT stack per eye are collected

and combined by 2-D interpolation.

It is known that, each OCT scan from every data stack is about $5\mu m$ apart. Taking the horizontal pixel positions in each scan as the x-coordinate, the thickness measurements per scan in μm as the z-coordinate, and the scan number as the y-coordinate, the intermediate thickness between two adjacent scans are estimated by interpolation. Corresponding to each sub-retinal layer, a surface is thus generated, where the x-axis is the horizontal pixel coordinates, y-axis is the interpolated scan numbers and the thickness at each point is color coded as a heat map, with red signifying a thick region while blue signifies a thin region. Finally, the resulting surface is smoothened by an averaging filter of size [5x5]. Each surface thus generated, represents the sub-retinal layer thickness maps for a patient. Such thickness maps can demonstrate the sub-retinal layer and location of abnormalities that can appear owing to pathology. They can also be used to track the changes in the sub-retinal layers that occur with time as a response to treatment.

The thickness maps corresponding to the 6 sub-retinal layers from a normal OCT image stack are shown in Fig. 7.3. Here, we observe that the color bar adjoining each surface represents sub-retinal layer thickness that is less than 120 μm for all the NFL, IPL, INL, ONL, IS/OS and RPE layers. This observation coincides with the sub-retinal layer thickness maps represented in [141] for normal images, thus corroborating the reliability of the proposed system. In Fig. 7.3, we observe that for normal OCT image stacks, the proposed method estimates the thickness maps significantly better than the CDWT method, which suffers from false detections in NFL due to the vitreous tissue segments, in IS/OS and RPE layers due to smoothening around the outer regions, and in the INL and ONL layers due to smoothened inner surfaces.

7.3 Experiments and Results

The performance of automated segmentation of sub-retinal surfaces, sub-retinal layers and the thickness maps is evaluated in four sets of experiments. In the first experiment, the performance of image denoising is analyzed for normal and abnormal OCT image stacks. In the second experiment, the error in segmenting the sub-retinal surfaces is

analyzed for normal and abnormal images. In the third experiment, the mean sub-retinal layer thickness estimates obtained using automated algorithms are compared against the manual segmentation estimates. Finally, in the fourth experiment, the changes in thickness maps between normal and abnormal image stacks are analyzed.

7.3.1 Performance of Automated Denoising

For this experiment, the denoised OCT images are scaled in [0,255] and then analyzed for pixel intensities.The performance metrics for evaluating the improvement in image quality by automated denoising are defined using in terms of the image foreground region and background region. For an OCT image, the region of interest is the retinal micro-structure that lies between the ILM (Surface 1) and BM (Surface 7). Additionally, the foreground includes the choroidal region as well. Hence, to generate a global foreground and background region mask for each image, the region 10 pixels above the manually segmented Surface 1 and 50 pixels below the manually segmented Surface 7 is selected as the foreground, and the remaining regions in each image is selected as the background. Next, μ_f, σ_f and μ_b, σ_b are estimated as mean and standard deviation of pixel values in the foreground and background regions, respectively. The denoising metrics are defined as global signal to noise ratio (SNR) in (7.5), global contrast to noise ratio (CNR) in (7.6) and peak SNR (PSNR) in (7.7). For the PSNR calculation, it is assumed that each OCT image contains $[n_1 \text{x} n_2]$ pixels.

$$SNR = 20\log_{10}\frac{\mu_f}{\sigma_b}. \tag{7.5}$$

$$CNR = \frac{|\mu_f - \mu_b|}{\sqrt{0.5\left(\sigma_f^2 + \sigma_b^2\right)}}. \tag{7.6}$$

$$\forall [i,j] \in I, I_d, \tag{7.7}$$

$$PSNR = 20\log_{10}\left(\frac{\max_{i,j} I(i,j)}{\sqrt{\frac{1}{n_1 . n_2}\sum_{i=1}^{n_1}\sum_{j=1}^{n_2}(I(i,j) - I_d(i,j))^2}}\right).$$

The foreground and background regions for an abnormal OCT image and the denoising performance metrics using the proposed Fourier-domain based method and the wavelet-based CDWT approach are shown in Fig. 7.4. Here, we observe that the retinal the proposed denoising method retains the surface edges and contrast variation in

the foreground region while it significantly reduces speckle noise from the background region when compared to the denoised image using CDWT.

The comparison between denoising metrics using the proposed method and the baseline CDWT method is shown in Table 7.2. Here, we observe that for OCT images from the normal and abnormal data sets, the proposed denoising method improves the image SNR by 12-13 dB, while the CDWT method improves the SNR by 3-4 dB only. The improvement in CNR fraction by the proposed and CDWT method are about 0.5 and 0.1, respectively. However, the CDWT method achieves a PSNR about 4.5 dB greater than the proposed method. The PSNR of the proposed method is smaller than the CDWT method because of the denominator in (7.7) that denotes the similarity in structure between the denoised and noisy image, and a more similar structure will ensure a small value for this quantity. The proposed method alters the structure of the noisy image in the background region due to the underlying Fourier-domain based deconvolution strategy, while he CDWT method conserves the image structure, and hence the difference in PSNR. The importance of the gain in SNR by the proposed denoising method versus the gain in PSNR by the CDWT method on automated sub-retinal surface segmentation will be analyzed in the next experiments.

Table 7.2: Performance of OCT image denoising using the proposed method versus the baseline CDWT denoising method evaluated on normal and abnormal OCT image stacks.

Image	SNR (dB)	CNR	PSNR (dB)
Normal set			
Noisy image	17.52±1.77	2.11±0.51	-
CDWT Denoising	21.03±1.87	2.20±0.54	27.91±1.39
Proposed Denoising	30.17±5.19	2.58±0.53	23.56±0.51
Abnormal set			
Noisy image	16.92±1.74	1.79±0.105	-
CDWT Denoising	19.32±1.16	1.91±0.08	28.08±1.84
Proposed Denoising	29.23±2.23	2.32±0.11	23.67±0.38

7.3.2 Sub-retinal Surface Segmentation Error

The absolute error incurred in segmenting each sub-retinal surface using the proposed denoising method or CDWT method followed by the proposed segmentation method on the normal and abnormal OCT images are shown in Table 7.3 and Table 7.4, respectively. The mean and standard deviation in the absolute error between the automated segmented surface and the manual segmented surface for all OCT images under analysis are evaluated inμm. In Table 7.3, the segmentation error incurred by three existing segmentation algorithms on the normal images is also shown for comparison. The absolute surface segmentation error was estimated by Bagci et. al. [133] on 14 SD-OCT images, by Chiu et. al. [136] on 100 B-scans, and by Yang et. al. on 38 image scans, respectively.

Table 7.3: Mean and standard deviation of sub-retinal surface segmentation error using the proposed method, and the baseline CDWT method compared to the performance of existing methods on normal OCT images. These errors are computed in μm.

Surface	Proposed	CDWT	Bagci et. al. [133]	Chiu et. al. [136]	Yang et. al. [142]
Surface 1	1.22±0.96	8.45±3.92	4.3±0.8	2.8±2.3	2.2±0.7
Surface 2	5.80±4.47	14.77±4.34	5.7±0.7	2.5±2.0	4.3±1.0
Surface 3	2.78±1.53	13.38±6.14	5.3±0.5	3.2±2.4	3.2±0.9
Surface 4	4.55±2.15	9.55±3.89	6.1±1.0	4.8±3.4	-
Surface 5	1.71±1.38	4.27±2.17	8.8±1.2	3.8±2.9	-
Surface 6	2.51±2.35	12.90±3.13	4.3±1.1	2.8±2.4	-
Surface 7	2.05±2.17	12.58±5.01	5.5±1.0	3.2±2.8	2.4±1.2

In Table 7.3, we observe that on normal OCT images, the proposed denoising and segmentation method incurs 1-6 μm of error across all the sub-retinal surfaces, that is significantly better than the CDWT baseline denoising method followed by proposed segmentation that results in 4-14 μm of error. Also, the proposed method has lower segmentation error when compared to other segmentation algorithms on all surfaces other than Surface 2, which is the least distinctive edge. Thus, on normal OCT images, the proposed method has comparative to better sub-retinal surface segmentation performance when compared to baseline CDWT or existing algorithms.

For images from the abnormal set, the surface segmentation errors by the proposed method and baseline CDWT method is shown in Table 7.4. Since pathological changes

Table 7.4: Mean and standard deviation of sub-retinal surface segmentation error using the proposed method, and the baseline CDWT denoising method on abnormal OCT images. These errors are computed in μm.

Surface	Proposed	CDWT
Surface 1	4.02±4.82	10.97±5.64
Surface 2	26.99±10.04	22.57±5.69
Surface 3	19.97±7.49	23.64±12.18
Surface 4	16.83±8.77	20.95±11.59
Surface 5	6.81±6.42	8.02±2.29
Surface 7	3.51±2.86	7.05±1.78

due to DME do not affect the PIS layer (Surface 6), hence this sub-retinal surface was not manually annotated. For all the other sub-retinal surfaces, we observe a significant increase in the segmentation error for Surface 2, Surface 3, Surface 4 and Surface 5 for the abnormal OCT images when compared to the normal images. This increase in segmentation error is unavoidable since the disorganization caused by pathology significantly alters the inner retinal layers, making the inner surfaces significantly less distinct even for manual annotation. In Table 7.4, we also observe that for all surfaces other than Surface 2, the baseline CDWT method incurs more error on abnormal images than the proposed approach. This happens because for abnormal images with large cysts, the Surface 2 may appear very close to Surface 1 (as shown in Fig. 7.2 (g)), in which case false edges may get detected by the proposed denoising method, causing the segmentation error to increase. In such cases the CDWT approach smoothens the false edges close to the Surface 1, thereby resulting in less error for Surface 2, but in turn increasing the error for segmenting Surface 3 through Surface 7 due to this smoothing action.

Since the error in the Surface 2 is significantly high for abnormal OCT images using the proposed segmentation algorithm, the sub-retinal layer thicknesses on such abnormal images will be analyzed for the NFL and IPL layers combined (NFL+IPL, between Surface 1 and Surface 3), the INL, ONL and Outer layer (between Surface 5 and Surface 7). It is noteworthy, that although the performance of automated surface segmentation deteriorates on images with pathology, the proposed denoising and segmentation method

is adaptable for segmenting the inner sub-retinal layers in normal and abnormal images, which is a significant improvement over existing automated segmentation algorithms that have not been reported to segment sub-retinal surface in images with DME so far.

7.3.3 Sub-retinal Layer Thickness Estimation

Once the sub-retinal surfaces are segmented, the next step is to estimate average sub-retinal layer thicknesses. The mean and standard deviation of the sub-retinal layer thickness for normal and abnormal OCT images is shown in Table 7.5 and Table 7.6, respectively. In these tables the mean thickness of every sub-retinal layer segmented manually is compared with the automated sub-retinal layer thickness estimation results using the proposed method and the baseline CDWT approach. The sub-retinal layer segmentation distribution is analyzed in terms of the average layer thickness, mean correlation coefficient 'r' and R^2 statistic between the manual and automated thickness measurements made for each image at every horizontal pixel location. A higher value of 'r' and R^2 statistic for each OCT image denotes better sub-retinal layer segmentation performance.

Table 7.5: Mean and standard deviation of sub-retinal layer thickness in normal images measured in μm.

Layer	Manual	Proposed(r,R^2)	CDWT (r,R^2)
NFL	52.4±8.7	52.6±11.5(0.86,0.7)	49.4±12.2(0.62,0.4)
IPL/GL	72.7±5.6	73.3±9.3(0.79,0.6)	61.9±15.6 (0.49,0.2)
INL	57.42±7.4	59.9±10.3(0.83,0.7)	72.2±4.9(0.39,0.1)
ONL	74.97±6.0	73.1±6.8(0.83,0.7)	70.5±11.0(0.39,0.1)
IS/OS	38.02±10.5	38.2±11.0(0.77,0.6)	20.3±5.9(0.36,0.1)
RPE	35.01±6.6	35.5±10.0(0.75,0.6)	42.0±8.3(0.33,0.1)
NFL+IPL	225.9±9.1	226.9±9.9(0.98,0.9)	226.4±6.39(0.43,0.2)
Inner	244.6±10.8	245.8±11.1(0.98,0.9)	250.3±8.9(0.32,0.1)
Outer	64.5±7.1	65.1±8.64(0.82,0.7)	53.70±6.3(0.39,0.1)

In Table 7.5, we observe that for OCT images from the normal set, the proposed method incurs up to 2 μm error in estimating the mean sub-retinal layer thickness with r, R^2 consistently greater than 0.75 and 0.6, respectively. However, the baseline CDWT method incurs $3-18\mu m$ error in estimating the sub-retinal layer thickness with

significantly low r, R^2 metrics. The p-values for both the proposed segmentation system and the baseline CDWT system is < 0.01. This analysis illustrates that although average surface segmentation error between the proposed and baseline CDWT method was not very high, the error in mean sub-retinal layer thickness and distribution of sub-retinal layer thickness becomes significantly high.

Table 7.6: Mean and standard deviation of sub-retinal layer thickness in abnormal images measured in μm.

Layer	Manual	Proposed(r,R^2)	CDWT(r,R^2)
NFL+IPL	111.5±15.9	129.4±19.7(0.78,0.6)	135.6±29.7(0.75,0.6)
INL	62.7±10.6	60.9±15.0(0.73,0.5)	76.9±14.5(0.36,0.1)
ONL	89.9±15.3	81.0±13.9(0.71,0.5)	70.9±11.4(0.23,0.1)
Inner	265.6±33.1	274.9±34.6(0.92,0.8)	274.0±61.3(0.90,0.8)
Outer	60.9±8.44	57.4±14.4(0.74,0.6)	49.7±10.6(0.32,0.1)

In Table 7.6, we observe that the proposed method incurs $2-18\mu m$ error in estimating the mean sub-retinal layer thickness with r, R^2 statistics consistently more than 0.7 and 0.5, respectively. On the other hand, the baseline CDWT method incurs $12-24\mu m$ error for mean thickness estimation with (r, R^2) statistics ranging from (0.3, 0.1) to (0.9, 0.8).

7.3.4 Thickness Map Analysis

Finally, the segmented sub-retinal thickness distributions obtained for each OCT image are combined for all images from a particular OCT stack to generate thickness maps. The sub-retinal layer thickness maps for an abnormal image stack with cystic DME are shown in Fig. 7.5.

Fig. 7.5 contains the OCT scan shown in Fig. 7.2. In Fig. 7.5 we observe that the thickness maps of the proposed method resemble the manually segmented thickness maps more than the baseline CDWT method.

It is important to note that the thickness maps of INL and ONL vary significantly for normal and abnormal OCT stacks. This difference is illustrated in Fig. 7.6, where manually segmented thickness maps from two normal and two abnormal OCT stacks each are shown. In Fig. 7.6 thickness maps of the INL in normal images demonstrate

thinning at the central fovea while ONL in normal images demonstrate a relatively thick layer at the fovea with the maximum thickness below $120\mu m$. This observation is intuitive. However, in the INL maps for abnormal images with DME, the thin INL at central fovea disappears, and the ONL either appears irregular or the thickness exceeds 200 μm. These changes to the INL and ONL thickness maps occur due to the sub-retinal cysts that form or the disorganization that occurs due to pathology. Since these differences in INL and ONL thickness maps are evident, these thickness maps could in turn be used as an indicator of disease severity or risk to visual acuity in future clinical studies.

From the previous experiments we have observe that the proposed sub-retinal surface segmentation method achieves '$r > 0.8$' ($p < 0.001$) for segmenting thickness maps of INL and ONL from normal OCT stacks, but this accuracy deteriorates to 0.7 ($p < 0.001$) for thickness maps of INL and ONL in abnormal OCT stacks. Although the automated segmentation error in images with pathology is unavoidable, we observe the manual and automated thickness maps to identify some other features that may be strongly correlated to the manual thickness maps.

In Fig. 7.7, we analyze the area of irregularities in the INL and ONL thickness maps from DME patients. As observed in Fig. 7.6, the INL and ONL in abnormal images demonstrate abnormally high thickness, which appear to be plateau regions in their respective thickness maps. The contoured area of these plateau regions in INL and ONL extracted using the manual segmentations, proposed method and the Baseline CDWT approaches are shown in Fig. 7.7.

To obtain the contoured areas of irregular thickness from the manually and automated segmented thickness maps, the first step is the scale all the thickness maps in the minimum variation range that is obtained using the automated or manual methods. This means that if the thicknesses obtained by manual and automated segmentations range in [0, 120], and [0,200], respectively, then both thickness maps are scaled in [0,120]. Next, the area of the irregular plateau regions are obtained by low-pass filtering the scaled thickness map surface with an average [25x25] filter, followed by subtraction of the filtered surface from the actual and thresholding using Otsu's threshold function. Among all the regions that get extracted, the regions that lie towards the center of the surfaces with the large areas, and maximum surface pixel strength (that is indicative of

high thickness) are selected as the irregular areas. Thus, such irregular region areas that are extracted from the INL and ONL of manually and automated segmented thickness maps by the proposed and baseline CDWT approach and extracted and compared.

In Fig. 7.7 we observe that the combined area of irregular plateau regions extracted from the thickness maps of INL and ONL from manual segmentations is 7710 pixel^2, while the combined area of from the same layers obtained by the proposed method and baseline CDWT method are 7336 pixel^2 and 4321 pixel^2, respectively. Here, we observe that the manual segmentation captures the irregularity due to pathology in the INL and the ONL, while the automated segmentations capture this irregularity in the INL only. However, the combined area of irregularity from the INL and ONL obtained manually closely matches the area obtained by the proposed approach. On comparing the combined irregularity areas obtained in INL and ONL maps for the 15 OCT stacks under analysis, we observe that the proposed method and the baseline CDWT methods have $[r, R^2]$ statistics of [0.99,0.98] and [0.92, 0.85], respectively, with ($p < 0.001$). This analysis indicates that although automated segmentation on sub-retinal surfaces in abnormal OCT image stacks with DME has a lower correlation coefficient to the manual segmentations than normal images stacks, the area of irregularity obtained from thickness maps of the INL and ONL correlate highly with their manually segmented counterparts. This observation encourages the use of automated inner sub-retinal layer segmentation systems to clinically analyze pathology progression over time. Also, the combined area of irregularity in the INL and ONL can be assessed as an indicator for DME severity and visual acuity over time in future efforts.

7.4 Conclusions and Discussion

In this chapter we have proposed a novel automated segmentation system that denoises and segments 7 sub-retinal surfaces and 6 sub-retinal layers in the retinal microstructure for normal OCT images from healthy patients and in abnormal images from patients with DME in less than 35 seconds per image. The proposed system is implemented on a 2.53 GHz Intel Core i3 and 3 GB RAM Laptop system using MATLAB. Also, the sub-retinal layer thickness distributions from all images belonging to an OCT image stack are combined to generate thickness maps that aid analysis and assessment of DME with

time.

We analyze the performance of OCT speckle noise removal using the proposed Wiener deconvolution method that estimates noise parameters using a Fourier-domain structural error metric defined in [137]. The proposed denoising method is compared to wavelet-transform based CDWT method used in [129]. Our analysis shows that the proposed Fourier domain-based denoising method improves the image SNR by more than 12dB, and it retains the sub-retinal surface edges within the retinal microstructure while suppressing the speckle noise significantly in the image background, thereby incurring a PSNR of about 23.5dB. The CDWT method on the other hand conserves the sub-retinal structure of the image foreground and background by smoothing the sub-retinal edges, thereby achieving a high PSNR of about 28dB but an SNR enhancement of less than 5dB. Further analysis shows that the CDWT denoising method incurs more error while automated segmentation of sub-retinal surfaces when compared to the proposed denoising method. Thus, for the proposed sub-retinal surface and layer segmentation algorithm, the proposed Fourier-domain based denoising method is better suited.

The proposed sub-retinal surface segmentation algorithm exhibits significant reliability is extracting sub-retinal layer thicknesses for normal and abnormal OCT image stacks. These sub-retinal layer thicknesses can then be used to generate thickness maps for healthy eyes and for DME patients. The structure and thickness of the INL and ONL in healthy and abnormal OCT image stacks is observed to vary significantly. For OCT image stacks with DME, the INL and ONL demonstrate irregular plateau regions that appear due to underlying cysts and sub-retinal layer disorganizations. The proposed segmentation system is capable of capturing the combined area of irregularities in INL and ONL of abnormal image stacks with 'r=0.99'. Future efforts will be focused on further assessment of this combined area of irregularity in the INL and ONL for DME patients over time and for evaluating the correlation of this metric to visual acuity.

Another key observation is that the segmentation performance of the proposed denoising and segmentation algorithm deteriorates significantly from normal OCT images to abnormal ones, i.e., error in mean sub-retinal thickness estimation is $0-2\mu m$ for formal images and $2-18\mu m$ for abnormal images. However, the baseline CDWT denoising method followed by the proposed segmentation deteriorates significantly in estimating the distribution of sub-retinal thicknesses (low 'r' value), but the estimation of mean

sub-retinal layer thickness does not deteriorate as much, i.e., error in mean sub-retinal thickness estimation is $3-18\mu m$ for formal images and $12-24\mu m$ for abnormal images. This observation strengthens the fact that the proposed segmentation algorithm is robust and can be combined with other denoising approaches to estimate mean sub-retinal layer thickness in normal and abnormal images.

The estimation of irregular area on the thickness maps of INL and ONL using the proposed denoising and baseline CDWT methods followed by the proposed segmentation demonstrate high correlation with the area estimated from the manually segmented surfaces ($r > 0.92, p < 0.001$). This observation encourages further analysis of this irregular area metric for DME patients in future works.

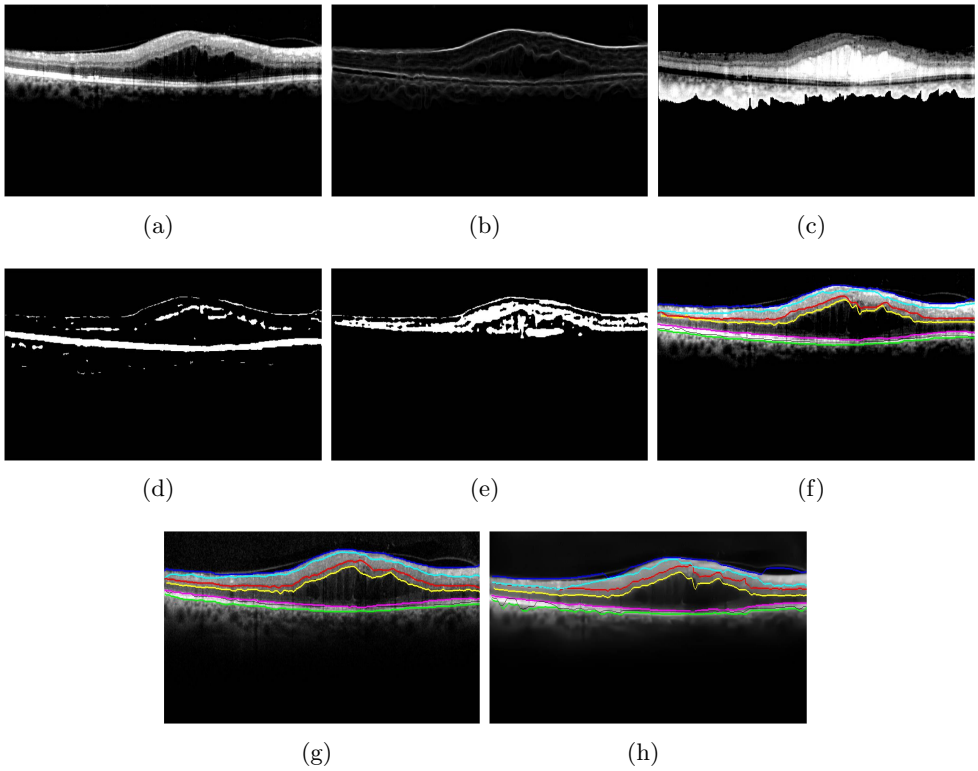

Figure 7.2: Steps for the proposed iterative multi-resolution segmentation algorithm on an abnormal OCT image. (a) Denoised image by the proposed method (I_d). (b)Image I_1 obtained after high-pass filtering in iteration $k = 1$. Thresholding this image results in the detection of Surface 1 and the choroidal segment(c) Negative source image $1 - I_d$ in iteration $k = 2$ within the region of interest marked by G_2 that extends between the Surface 1 and the choroid segment.(d) Image obtained after high-pass filtering and thresholding the image in (c) in iteration $k = 2$. The region with maximum major axis length is extracted in image I_{r_2}. The top surface of this region is Surface 5, and the bottom surface is Surface 7. (e) Image obtained in iteration $k = 4$ after high-pass filtering and thresholding. The region with maximum major axis length is selected in image I_{r_4}, and the bottom surface of this region is Surface 4. Two more iterations are performed to extract all 7 surfaces. (f) Automated segmentation achieved at the end of 6 iteration steps by the proposed method. (g) Manually marked surfaces. (h) Automated segmentation achieved using baseline CDWT approach for denoising followed by the proposed segmentation algorithm.

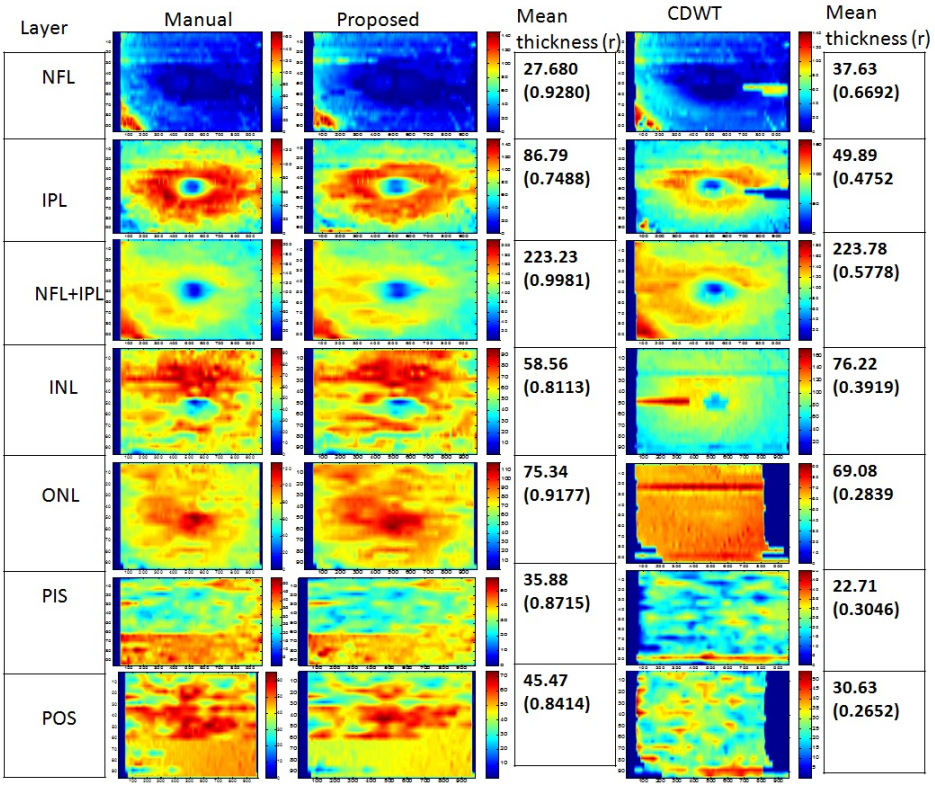

Figure 7.3: Sub-retinal layer thickness maps for a normal OCT image stack. The first column of images represents thickness maps generated by interpolating the sub-retinal thickness of each layer obtained by manual annotation. The second column of images represents the thickness maps obtained by the proposed denoising and segmentation algorithms. The third column of images represents the thickness maps obtained by the baseline CDWT denoising method followed by the proposed segmentation algorithm. For each segmented thickness map obtained by the proposed denoising method and the baseline CDWT method, the mean sub-retinal layer thickness and the correlation coefficient 'r' of automated thickness distribution with respect to the manual thicknesses are provided.

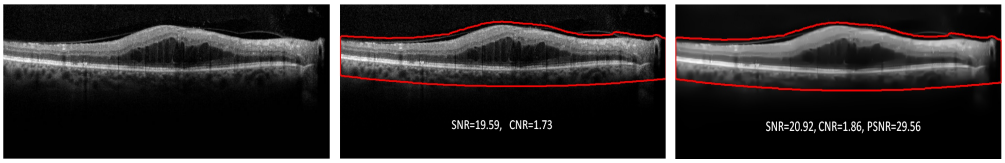

(a)

(b)

(c)

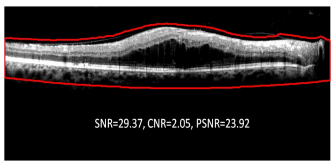

(d)

Figure 7.4: Example of automated OCT image denoising. (a) Noisy image (I), (b) The foreground region lies within the region bordered by the red boundary. All other regions are the background. (c) Denoised image by CDWT method. (d) Denoised image by the proposed method.

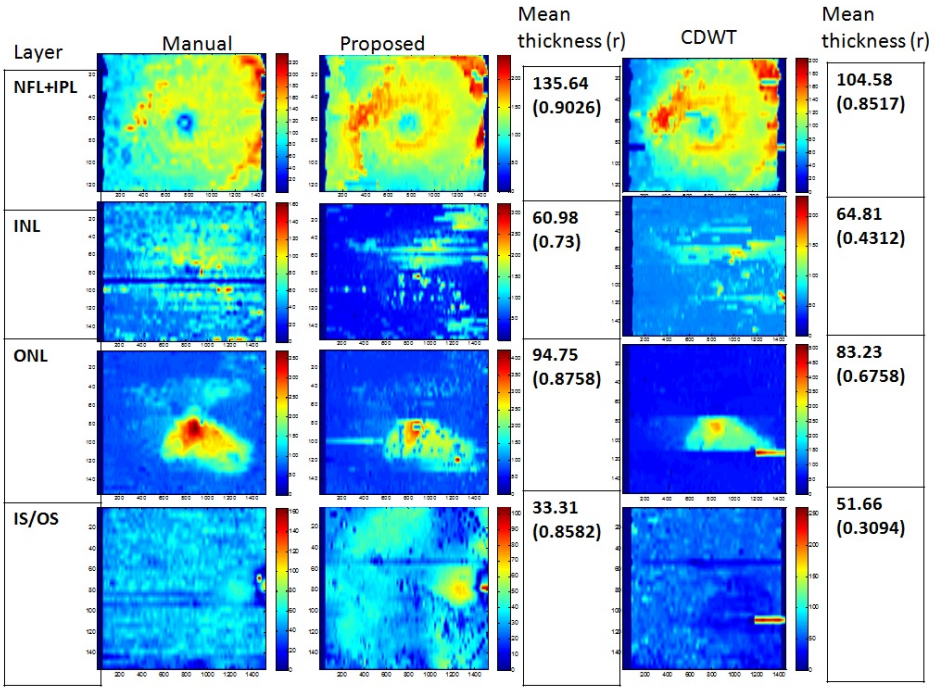

Figure 7.5: Sub-retinal layer thickness maps for an abnormal OCT image stack. The first column of images represents thickness maps generated by manual annotation. The second column of images represents the thickness maps obtained by the proposed method. The third column of images represents the thickness maps obtained by the baseline CDWT method. For each segmented thickness map obtained by the proposed denoising method and the baseline CDWT method, the mean sub-retinal layer thickness and the correlation coefficient 'r' of automated thickness distribution with respect to the manual thicknesses are provided.

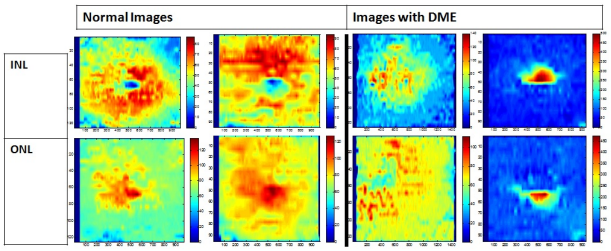

Figure 7.6: Difference between thickness maps of the INL and ONL in normal and abnormal images with DME.

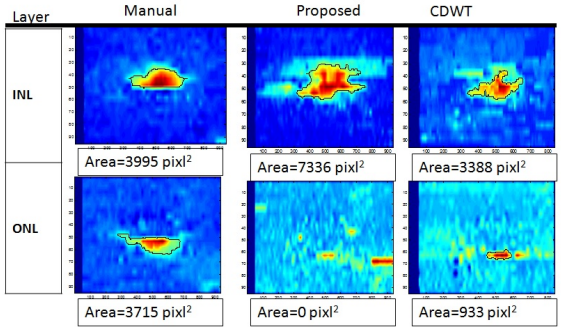

Figure 7.7: Irregular plateau regions observed in INL and ONL of the segmented abnormal OCT image stack. First second and third columns indicate thickness maps segmented manually, by the proposed method and by the baseline CDWT methods, respectively. The combined area of irregularity extracted from the INL and ONL from the manual thickness maps, are highly correlated to the combined area of INL and ONL from the automated segmentation methods.

Chapter 8

Conclusions and Future Work

8.1 Conclusions

In this thesis we have presented algorithms for automated information extraction from multi-modal ophthalmic images pertaining to the human retina. These algorithms are aimed at translating the cognitive understanding of specialists into computer intelligence. Using domain knowledge and theoretical concepts of digital image processing and machine learning, we have developed and optimized algorithms to segment the images into regions of interest and detect the presence of abnormalities due to pathologies in them. The algorithms presented here are both robust to variations in image due to the imaging cameras or pathologies, and computationally less complex when compared to existing algorithms. All the segmentation and pathology detection algorithms presented in this thesis have been analyzed using data sets that were manually annotated by specialists. The conclusions from three categories of contributions made in this thesis are as follows.

8.1.1 Automated Segmentation of Retinal Anatomical Regions in Fundus Images

In this thesis, we have presented two algorithms for automated segmentation of blood vessels from fundus images and one algorithm for automated detection of the OD boundary and vessel origin. The first algorithm for automated blood vessel segmentation uses

high-pass filtering and morphology based approach to detect major vessel regions followed by a classification-based approach to detect the fine blood vessels that are then added to the major vessels. For accurate vessel pixel identification, we analyze intensity-based pixel features to identify a most discriminating set of 8 features that classify a vessel pixel from a background non-vessel pixel. Vessel classification is done using a 2-Gaussian GMM classifier that ensures low computational complexity. This algorithm can be effectively used for detecting NVD, RoP vein occlusions and other vessel related retinal abnormalities.

The second algorithm for blood vessel segmentation uses an iterative approach to identify fine vessel segments and adding them to the existing vessel estimates. This algorithm utilizes a stopping criterion based on the rate of vessel-pixel addition to extract the best vessel estimate. Since this algorithm identifies sparse vessel segments in each iteration, it can be useful for automated detection of NVE caused by PDR, where vessel-like segments appear in close vicinity of the blood vessels.

The algorithm for OD boundary and vessel origin detection presented here is capable of detection the OD region in normal images and in images with abnormalities. This rule-based algorithm can be useful for cup-to-disc ratio measurements for patients with Glaucoma, and for detecting pathologies like NVD that affect the OD region.

8.1.2 Automated DR screening systems

Automated screenings of fundus images for DR require background detection modules for segmentation and removal of the blood vessels and the OD region in the initial stage. Next, in the foreground region, abnormal regions are detected as bright lesion and red lesions followed by classification of these lesion regions. The NPDR screening system presented in this thesis detects the most discriminating structure based feature set for classification of the lesion regions. Such a screening systems can reduce the number of images that need subsequent manual assessment by 50%.

Automated screening for PDR is a more challenging problem than NPDR, since the fine vessel-like abnormalities appear in close vicinity of the blood vessels that can be mistaken for blood vessel regions. Hence, the iterative vessel segmentation approach followed by structure-based decision making can detect these new-vessel abnormalities at the OD region and elsewhere.

8.1.3 Automated Segmentation of OCT images

Automated segmentation algorithms of sub-retinal layers for normal and pathological OCT images with DME have been presented in this thesis. These algorithms estimate the thickness of the sub-retinal layers and demonstrate the change caused by pathology. Such algorithms can aid quicker clinical assessments regarding the effectiveness of DME treatment over time.

8.2 Future Work

The algorithms presented in this thesis have been aimed at detecting abnormalities that can lead to acquired blindness in diabetic patients. Future work will be aimed at extending these algorithms to non-diabetic vision threatening pathologies such as hypertensive retinopathy. The directions for future work pertaining to each segmentation algorithm or screening system presented in this thesis are as follows.

- For the blood vessel segmentation algorithm using classification-based approach, the performance of other classifiers for vessel pixel identification can be analyzed. Also, using the Expectation-Maximization algorithm, GMM classifiers with more than 2 Gaussians can be trained for identifying fine vessel pixels. Also, the impact of the segmented vessel region for detection of NVD can be analyzed.

- For the iterative blood vessel segmentation algorithm, extensions of the proposed algorithm for blood vessel segmentation in wide-field or Optos images with more than 200^o FOV can be analyzed. Also, algorithms that use the presented methods of the blood vessel segmentation for detecting blood vessel properties such as tortuosity, arterio-venular ratio, vessel thickness and branching patterns can be developed. The effectiveness of the iterative blood vessel segmentation algorithm for NVE detection can be further analyzed.

- The automated OD segmentation algorithm presented in this thesis can be used with cup-to-disk ratio measurement modules to automatically assess the severity of Glaucoma. Also, the detection modules for the macula based on its distance from the OD region can be developed for severity analysis of maculopathy.

- The automated NPDR screening system can be analyzed on more images from locally acquired image sets for further performance verification. Also, the automated PDR detection module can be combined with the NPDR detection modules for a complete screening system for DR. Additionally, extensions to the existing DR screening system on wide field images can be analyzed.

- The automated PDR detection algorithms can be further fine-tuned using annotated training data sets. Structure-based features can be ranked in their order of their discriminating performance for detecting the laser scars, fibrosed tissues and NVE regions. Pixel-based performance evaluation for detecting fine vessel-like abnormalities can be done. Based on the abnormal vessel regions detected, the severity of PDR can also be analyzed for each fundus image.

- The proposed OCT segmentation system can be used to clinically asses the change in the inner sub-retinal layers for DME patients over time. Also, this system can be used on patients with other retinal pathologies such as Macular Telangiectasia (Mactel), maculopathy etc.

References

[1] K. Doi, "Computer-aided diagnosis in medical imaging: Historical review, current status and future potential," *Computerized medical imaging and graphics*, vol. 31, no. 4, pp. 198–211, 2007.

[2] C. for Disease Control and Prevention, "The economic impact of adult visual disorders in the united states." [Online]. Available: http://www.cdc.gov/visionhealth/publications/economic_impact.htm

[3] S. Roychowdhury, D. Koozekanani, and K. Parhi, "Dream: Diabetic retinopathy analysis using machine learning," *IEEE Journal of Biomedical and Health Informatics*, 2013.

[4] M. D. Abramoff, M. Niemeijer, and S. R. Russell, "Automated detection of diabetic retinopathy: barriers to translation into clinical practice," in *Expert Review of Medical Devices*, vol. 7, no. 2, 2010, pp. 287–296.

[5] CDC, "Diabetic retinopathy. atlanta, ga: National for chronic disease prevention and health promotion." March 23,2011. [Online]. Available: http://www.cdc.gov/visionhealth/pdf/factsheet.pdf

[6] H. M. Pakter, S. C. Fuchs, M. K. Maestri, L. B. Moreira, L. M. Dei Ricardi, V. F. Pamplona, M. M. Oliveira, and F. D. Fuchs, "Computer-assisted methods to evaluate retinal vascular caliber: What are they measuring?" *Investigative Ophthalmology and Visual Science*, vol. 52, no. 2, pp. 810–815, 2011.

[7] K. Kotliar, E. Nagel, W. Vilser, S.-F. Seidova, and I. Lanzl, "Microstructural alterations of retinal arterial blood column along the vessel axis in systemic hypertension," *Investigative Ophthalmology and Visual Science*, vol. 51, no. 4, pp. 2165–2172, 2010.

[8] A. Kochkorov, K. Gugleta, C. Zawinka, R. Katamay, J. Flammer, and S. Orgul, "Short-term retinal vessel diameter variability in relation to the history of cold extremities," *Investigative Ophthalmology and Visual Science*, vol. 47, no. 9, pp. 4026–4033, 2006.

[9] E. Nagel, W. Vilser, and I. Lanzl, "Age, blood pressure, and vessel diameter as factors influencing the arterial retinal flicker response," *Investigative Ophthalmology and Visual Science*, vol. 45, no. 5, pp. 1486–1492, 2004.

[10] S. Roychowdhury, D. D. Koozekanani, and K. K. Parhi, "Screening fundus images for diabetic retinopathy," in *2012 Conference Record of the Forty Sixth Asilomar Conference on Signals, Systems and Computers (ASILOMAR)*, 2012, pp. 1641–1645.

[11] R. Perfetti, E. Ricci, D. Casali, and G. Costantini, "Cellular neural networks with virtual template expansion for retinal vessel segmentation," *IEEE Transactions on Circuits and Systems II: Express Briefs*, vol. 54, no. 2, pp. 141–145, 2007.

[12] M. Fraz, P. Remagnino, A. Hoppe, B. Uyyanonvara, A. Rudnicka, C. Owen, and S. Barman, "An ensemble classification-based approach applied to retinal blood vessel segmentation," *IEEE Transactions on Biomedical Engineering*, vol. 59, no. 9, pp. 2538–2548, 2012.

[13] D. Marin, A. Aquino, M. Gegundez-Arias, and J. Bravo, "A new supervised method for blood vessel segmentation in retinal images by using gray-level and moment invariants-based features," *IEEE Transactions on Medical Imaging*, vol. 30, no. 1, pp. 146–158, 2011.

[14] M. Fraz, P. Remagnino, A. Hoppe, B. Uyyanonvara, A. Rudnicka, C. Owen, and S. Barman, "Blood vessel segmentation methodologies in retinal images a survey,"

Computer Methods and Programs in Biomedicine, vol. 108, no. 1, pp. 407 – 433, 2012.

[15] A. Hoover, V. Kouznetsova, and M. Goldbaum, "Locating blood vessels in retinal images by piecewise threshold probing of a matched filter response," *IEEE Transactions on Medical Imaging*, vol. 19, pp. 203–210, 2000.

[16] R. Rangayyan, F. Oloumi, F. Oloumi, P. Eshghzadeh-Zanjani, and F. Ayres, "Detection of blood vessels in the retina using gabor filters," in *Canadian Conference on Electrical and Computer Engineering*, 2007, pp. 717–720.

[17] A. Mendonca and A. Campilho, "Segmentation of retinal blood vessels by combining the detection of centerlines and morphological reconstruction," *IEEE Transactions on Medical Imaging*, vol. 25, no. 9, pp. 1200–1213, 2006.

[18] M. Miri and A. Mahloojifar, "Retinal image analysis using curvelet transform and multistructure elements morphology by reconstruction," *IEEE Transactions on Biomedical Engineering*, vol. 58, no. 5, pp. 1183–1192, 2011.

[19] K. A. Vermeer, F. M. Vos, H. G. Lemij, and A. M. Vossepoel, "A model based method for retinal blood vessel detection," *Computers in Biology and Medicine*, vol. 34, no. 3, pp. 209–219, 2004.

[20] B. Lam and H. Yan, "A novel vessel segmentation algorithm for pathological retina images based on the divergence of vector fields," *IEEE Transactions on Medical Imaging*, vol. 27, no. 2, pp. 237–246, 2008.

[21] B. Lam, Y. Gao, and A.-C. Liew, "General retinal vessel segmentation using regularization-based multiconcavity modeling," *IEEE Transactions on Medical Imaging*, vol. 29, no. 7, pp. 1369–1381, 2010.

[22] X. Jiang and D. Mojon, "Adaptive local thresholding by verification-based multithreshold probing with application to vessel detection in retinal images," *IEEE Transactions on Pattern Analysis and Machine Intelligence*, vol. 25, no. 1, pp. 131–137, 2003.

[23] B. Al-Diri, A. Hunter, and D. Steel, "An active contour model for segmenting and measuring retinal vessels," *IEEE Transactions on Medical Imaging*, vol. 28, no. 9, pp. 1488–1497, 2009.

[24] A. Budai, G. Michelson, and J. Hornegger, "Multiscale blood vessel segmentation in retinal fundus images," *Proc. Bildverarbeitung fr die Med.*, pp. 261–265, March 2010.

[25] A. Budai, R. Bock, A. Maier, J. Hornegger, and G. Michelson, "Robust vessel segmentation in fundus images," *International Journal of Biomedical Imaging*, no. 154860, 2013.

[26] M. Niemeijer, J. Staal, B. van Ginneken, M. Loog, and M. D. Abramoff, "Comparative study of retinal vessel segmentation methods on a new publicly available database," *Proc. SPIE 5370, Medical Imaging*, vol. 5370, pp. 648–656, 2004.

[27] J. Staal, M. Abramoff, M. Niemeijer, M. Viergever, and B. van Ginneken, "Ridge-based vessel segmentation in color images of the retina," *IEEE Transactions on Medical Imaging*, vol. 23, no. 4, pp. 501–509, 2004.

[28] J. Soares, J. Leandro, R. Cesar, H. Jelinek, and M. Cree, "Retinal vessel segmentation using the 2-D Gabor wavelet and supervised classification," *IEEE Transactions on Medical Imaging*, vol. 25, no. 9, pp. 1214–1222, 2006.

[29] E. Ricci and R. Perfetti, "Retinal blood vessel segmentation using line operators and support vector classification," *IEEE Transactions on Medical Imaging*, vol. 26, no. 10, pp. 1357–1365, 2007.

[30] K. U. Research, "Chase_db1," January 2011. [Online]. Available: http://blogs.kingston.ac.uk/retinal/chasedb1/.

[31] A. Frame, P. Undrill, M. Cree, J. Olson, K. McHardy, P. Sharp, and J. Forrester, "A comparison of computer based classification methods applied to the detection of microaneurysms in ophthalmic fluorescein angiograms," *Comput. Biol. Med.*, vol. 28, pp. 225–238, 1998.

[32] V. Cherkassky and F. Mullier, "Learning from data," *John Wiley and sons, New York*, 1998.

[33] H. Peng, F. Long, and C. Ding, "Feature selection based on mutual information criteria of max-dependency, max-relevance, and min-redundancy," *Pattern Analysis and Machine Intelligence, IEEE Transactions on*, vol. 27, no. 8, pp. 1226–1238, Aug 2005.

[34] K. Goatman, A. Fleming, S. Philip, G. Williams, J. Olson, and P. Sharp, "Detection of new vessels on the optic disc using retinal photographs," *IEEE Transactions on Medical Imaging*, vol. 30, no. 4, pp. 972–979, 2011.

[35] C. M. Wilson, K. D. Cocker, M. J. Moseley, C. Paterson, S. T. Clay, W. E. Schulenburg, M. D. Mills, A. L. Ells, K. H. Parker, G. E. Quinn, A. R. Fielder, and J. Ng, "Computerized analysis of retinal vessel width and tortuosity in premature infants," *Investigative Ophthalmology and Visual Science*, vol. 49, no. 8, pp. 3577–3585, 2008.

[36] A. Karperien, H. F. Jelinek, J. J. Leandro, J. V. Soares, R. M. Cesar Jr, and A. Luckie, "Automated detection of proliferative retinopathy in clinical practice," *Clinical ophthalmology (Auckland, NZ)*, vol. 2, no. 1, p. 109, 2008.

[37] T. Teng, M. Lefley, and D. Claremont, "Progress towards automated diabetic ocular screening: A review of image analysis and intelligent systems for diabetic retinopathy," *Medical and Biological Engineering and Computing*, vol. 40, pp. 2–13, 2002.

[38] R. C. Gonzalez and R. E. Woods, *Digital Image Processing*, 2nd ed. Boston, MA, USA: Addison-Wesley Longman Publishing Co., Inc., 1992.

[39] R. A. Abdel-Ghafar and T. Morris, "Progress towards automated detection and characterization of the optic disc in glaucoma and diabetic retinopathy," *Medical Informatics and the Internet in Medicine*, vol. 32, no. 1, pp. 19–25, March 2007.

[40] D. Koozekanani, K. Boyer, C. Roberts, and S. Katz, "Tracking the optic nerve head in oct video using dual eigenspaces and an adaptive vascular distribution

model," in *Proceedings of the 2001 IEEE Computer Society Conference on Computer Vision and Pattern Recognition, 2001.*, vol. 1, 2001, pp. I–934–I–941 vol.1.

[41] R. J. Qureshi, L. Kovacs, B. Harangi, B. Nagy, T. Peto, and A. Hajdu, "Combining algorithms for automatic detection of optic disc and macula in fundus images," *Computer Vision and Image Understanding*, vol. 116, no. 1, pp. 138 – 145, 2012.

[42] A. Aquino, M. Gegundez-Arias, and D. Marin, "Detecting the optic disc boundary in digital fundus images using morphological, edge detection, and feature extraction techniques," *IEEE Transactions on Medical Imaging*, vol. 29, no. 11, pp. 1860 –1869, nov. 2010.

[43] C. Sinthanayothin, J. F. Boyce, H. L. Cook, and T. H.Williamson, "Automated localisation of the optic disk, fovea, and retinal blood vessels from digital colour fundus images," *Br. J. Ophthalmol*, vol. 83, no. 8, pp. 902–910, 1999.

[44] A. Hoover, , and M. Goldbaum, "Locating the optic nerve in retinal image using the fuzzy convergence of bood vessels," *IEEE Transactions on Medical Imaging*, vol. 22, August 2003.

[45] F. ter Haar, "Automatic localization of the optic disc in digital colour images of the human retina," *M.S. Thesis*, 2005.

[46] A. Osareh, M. Mirmehdi, B. Thomas, and R. Markham, "Classification and localisation of diabetic-related eye disease," in *Computer Vision ECCV 2002*, ser. Lecture Notes in Computer Science, vol. 2353. Springer Berlin / Heidelberg, 2006, pp. 325–329.

[47] M. Lalonde, M. Beaulieu, and L. Gagnon, "Fast and robust optic disc detection using pyramidal decomposition and hausdorff-based template matching," *IEEE Transactions on Medical Imaging*, vol. 20, no. 11, pp. 1193 –1200, Nov. 2001.

[48] H. Yu, S. Barriga, C. Agurto, S. Echegaray, M. Pattichis, G. Zamora, W. Bauman, and P. Soliz, "Fast localization of optic disc and fovea in retinal images for eye disease screening," *Medical Imaging 2011: Computer-Aided Diagnosis*, vol. 7963, no. 1, p. 796317, 2011.

[49] J. Lowell, A. Hunter, D. Steel, A. Basu, R. Ryder, E. Fletcher, and L. Kennedy, "Optic nerve head segmentation," *IEEE Transactions on Medical Imaging*, vol. 23, no. 2, pp. 256 –264, Feb. 2004.

[50] R. Rangayyan, X. Zhu, and F. Ayres, "Detection of the optic disc in images of the retina using gabor filters and phase portrait analysis," in *4th European Conference of the International Federation for Medical and Biological Engineering*, 2009, vol. 22, pp. 468–471.

[51] A. Salazar-Gonzalez, Y. Li, and X. Liu, "Optic disc segmentation by incorporating blood vessel compensation," in *IEEE Third International Workshop On Computational Intelligence In Medical Imaging (CIMI)*, 2011, pp. 1–8.

[52] D. Welfer, J. Scharcanski, C. M. Kitamura, M. M. Dal Pizzol, L. W. B. Ludwig, and D. R. Marinho, "Segmentation of the optic disk in color eye fundus images using an adaptive morphological approach," *Comput. Biol. Med.*, vol. 40, no. 2, pp. 124–137, Feb. 2010.

[53] A. M. Mendonca, A. Sousa, L. Mendonca, and A. Campilho, "Automatic localization of the optic disc by combining vascular and intensity information," *Computerized medical imaging and graphics : the official journal of the Computerized Medical Imaging Society*, vol. 37(5-6), pp. 409–417, Sept 2013.

[54] M. Goldbaum, S. Moezzi, A. Taylor, S. Chatterjee, J. Boyd, E. Hunter, and R. Jain, "Automated diagnosis and image understanding with object extraction, object classification, and inferencing in retinal images," vol. 3, Sept. 1996, pp. 695 –698 vol.3.

[55] M. Niemeijer, J. Staal, B. van Ginneken, M. Loog, and M. D. Abramoff, "Comparative study of retinal vessel segmentation methods on a new publicly available database," *Medical Imaging 2004: Image Processing*, vol. 5370, no. 1, pp. 648–656, 2004.

[56] M. Niemeijer, M. Abramoff, and B. van Ginneken, "Segmentation of the optic disc, macula and vascular arch in fundus photographs," *IEEE Transactions on Medical Imaging*, vol. 26, no. 1, pp. 116 –127, Jan. 2007.

[57] S. Morales, V. Naranjo, J. Angulo, and M. Alcaniz, "Automatic detection of optic disc based on pca and mathematical morphology," *IEEE Transactions on Medical Imaging*, vol. 32, no. 4, pp. 786–796, April 2013.

[58] "Gnu image manipulation program," January 1996. [Online]. Available: http://www.gimp.org/downloads/.

[59] J. Staal, M. Abramoff, M. Niemeijer, M. Viergever, and B. van Ginneken, "Ridge based vessel segmentation in color images of the retina," *IEEE Transactions on Medical Imaging*, vol. 23, pp. 501–509, 2004.

[60] T. Kauppi, V. Kalesnykiene, J.-K. Kmrinen, L. Lensu, I. Sorr, A. Raninen, R. Voutilainen, H. Uusitalo, H. Klviinen, and J. Pietil, "Diaretdb1 diabetic retinopathy database and evaluation protocol," *Proc. of the 11th Conf. on Medical Image Understanding and Analysis (MIUA2007)*, pp. 61–65, 2007.

[61] T. Kauppi, V. Kalesnykiene, J.-K. Kamarainen, L. Lensu, I. Sorri, H. Uusitalo, H. Klviinen, and J. Pietil, "Diaretdb0: Evaluation database and methodology for diabetic retinopathy algorithms," Lappeenranta University of Technology, Finland, Tech. Rep., 2006.

[62] "Methods to evaluate segmentation and indexing techniques in the field of retinal ophthalmology." Accessed Sept 23, 2011. [Online]. Available: http://messidor.crihan.fr/download-en.php

[63] A. Sopharak, B. Uyyanonvara, S. Barman, and T. H. Williamson, "Automatic detection of diabetic retinopathy exudates from non-dilated retinal images using mathematical morphology methods," *Computerized Medical Imaging and Graphics*, vol. 32, no. 8, pp. 720 – 727, 2008.

[64] T. Walter, J.-C. Klein, P. Massin, and A. Erginay, "A contribution of image processing to the diagnosis of diabetic retinopathy-detection of exudates in color fundus images of the human retina," *IEEE Transactions on Medical Imaging*, vol. 21, no. 10, pp. 1236–1243, 2002.

[65] J. Seo, K. Kim, J. Kim, K. Park, and H. Chung, "Measurement of ocular torsion using digital fundus image," in *26th Annual International Conference of the IEEE Engineering in Medicine and Biology Society*, vol. 1, 2004, pp. 1711–1713.

[66] G. Kande, P. Subbaiah, and T. Savithri, "Segmentation of exudates and optic disk in retinal images," in *Sixth Indian Conference on Computer Vision, Graphics Image Processing*, 2008, pp. 535–542.

[67] K. Stapor, A. Switonski, R. Chrastek, and G. Michelson, "Segmentation of fundus eye images using methods of mathematical morphology for glaucoma diagnosis," in *International Conference on Computational Science*, 2004, pp. 41–48.

[68] C. Lupascu, D. Tegolo, and L. Di Rosa, "Automated detection of optic disc location in retinal images," in *IEEE International Symposium on Computer-Based Medical Systems*, 2008, pp. 17–22.

[69] Y. Zeng, D. Samaras, W. Chen, and Q. Peng, "Topology cuts: A novel min-cut/max-flow algorithm for topology preserving segmentation in n-d images," *Comput. Vis. Image Underst.*, vol. 112, no. 1, pp. 81–90, Oct. 2008.

[70] Y. Boykov and G. Funka-Lea, "Graph cuts and efficient n-d image segmentation," *International Journal of Computer Vision*, vol. 70, no. 2, pp. 109–131, 2006.

[71] S. Lu and J.-H. Lim, "Automatic optic disc detection from retinal images by a line operator," *IEEE Transactions on Biomedical Engineering*, vol. 58, no. 1, pp. 88–94, 2011.

[72] S. Ravishankar, A. Jain, and A. Mittal, "Automated feature extraction for early detection of diabetic retinopathy in fundus images," in *IEEE Conference on Computer Vision and Pattern Recognition*, 2009, pp. 210–217.

[73] M. Niemeijer, M. D. Abrmoff, and B. van Ginneken, "Fast detection of the optic disc and fovea in color fundus photographs," *Medical Image Analysis*, vol. 13, no. 6, pp. 859 – 870, 2009.

[74] A. Dehghani, H. Moghaddam, and M.-S. Moin, "Optic disc localization in retinal images using histogram matching," *EURASIP Journal on Image and Video Processing*, vol. 2012, no. 1, pp. 1–11, 2012.

[75] A.-H. Abdel-Razik Youssif, A. Ghalwash, and A. Abdel-Rahman Ghoneim, "Optic disc detection from normalized digital fundus images by means of a vessels' direction matched filter," *IEEE Transactions on Medical Imaging*, vol. 27, no. 1, pp. 11 –18, Jan. 2008.

[76] American Diabetes Association, "Data from the 2011 national diabetes fact sheet." Jan. 26, 2011. [Online]. Available: http://www.diabetes.org/diabetes-basics/diabetes-statistics/

[77] S. Garg and R. M. Davis, "Diabetic retinopathy screening update," *CliniCal Diabetes*, vol. 27, no. 4, pp. 140–145, 2009.

[78] J. Cuadros and G. Bresnick, "Eyepacs: An adaptable telemedicine system for diabetic retinopathy screening," *J Diabetes Sci Technol.*, vol. 3, no. 3, p. 509516, May 2009.

[79] G. Quellec, M. Lamard, P. Josselin, and G. Cazuguel, "Optimal wavelet transform for the detection of microaneurysm in retina photographs," *IEEE Transactions on Medical Imaging*, vol. 27, pp. 1230 –1241, 2008.

[80] B. Zhang, X. Wu, J. You, Q. Li, and F. Karray, "Detection of microaneurysms using multi-scale correlation coefficients," *Pattern Recognition*, vol. 43, no. 6, pp. 2237 – 2248, 2010.

[81] C. Agurto, V. Murray, E. Barriga, S. Murillo, M. Pattichis, H. Davis, S. Russell, M. Abramoff, and P. Soliz, "Multiscale am-fm methods for diabetic retinopathy lesion detection," *IEEE Transactions on Medical Imaging*, vol. 29, no. 2, pp. 502–512, February 2010.

[82] G. S. Scotland, P. McNamee, A. D. Fleming, K. A. Goatman, S. Philip, G. J. Prescott, P. F. Sharp, G. J. Williams, W. Wykes, G. P. Leese, and J. A. Olson, "Costs and consequences of automated algorithms versus manual grading for the

detection of referable diabetic retinopathy," *British Journal of Ophthalmology*, vol. 94, no. 6, pp. 712–719, 2010.

[83] M. D. Abramoff, M. Niemeijer, M. S. Suttorp-Schulten, M. A. Viergever, S. R. Russell, and B. van Ginneken, "Evaluation of a system for automatic detection of diabetic retinopathy from color fundus photographs in a large population of patients with diabetes," *Diabetes Care*, vol. 31, no. 2, pp. 193–198, February 2008.

[84] L. Shen and L. Bai, "Abstract adaboost gabor feature selection for classification," *Proc. of Image and Vision Computing, New Zealand*, pp. 77–83, 2004.

[85] M. Niemeijer, B. van Ginneken, J. Staal, M. Suttorp-Schulten, and M. Abramoff, "Automatic detection of red lesions in digital color fundus photographs," *IEEE Transactions on Medical Imaging*, vol. 24, no. 5, pp. 584 –592, May 2005.

[86] A. Osareh, B. Shadgar, and R. Markham, "Comparative pixel-level exudate recognition in colour retinal images," *Image Analysis and Recognition*, vol. 3656, pp. 894–902, 2005.

[87] L. Xu and S. Luo, "Support vector machine based method for identifying hard exudates in retinal images," in *IEEE Youth Conference on Information, Computing and Telecommunication, 2009. YC-ICT '09*, Sept. 2009, pp. 138 –141.

[88] U. R. Acharya, C. K. Chua, E. Y. Ng, W. Yu, and C. Chee, "Application of higher order spectra for the identification of diabetes retinopathy stages," *Journal of Medical Systems*, vol. 32, pp. 481–488, 2008.

[89] G. Shafer, "A mathematical theory of evidence," *Princeton, N.J.: Princeton University Press*, 1976.

[90] C.-C. Chang and C.-J. Lin, "LIBSVM: A library for support vector machines," *ACM Transactions on Intelligent Systems and Technology*, vol. 2, pp. 27:1–27:27, 2011, software available at http://www.csie.ntu.edu.tw/~cjlin/libsvm.

[91] M. Niemeijer, B. van Ginneken, J. Staal, M. Suttorp-Schulten, and M. Abramoff, "Automatic detection of red lesions in digital color fundus photographs," *IEEE Transactions on Medical Imaging*, vol. 24, no. 5, pp. 584 –592, May 2005.

[92] L. Talavera, "Feature selection as retrospective pruning in hierarchical clustering," *Advances in Intelligent Data Analysis*, vol. 1642, pp. 75–86, 1999.

[93] M. G. Lawrence, "The accuracy of digital-video retinal imaging to screen for diabetic retinopathy: an analysis of two digital-video retinal imaging systems using standard stereoscopic seven-field photography and dilated clinical examination as reference standards," *Trans Am Ophthalmol Soc*, vol. 102, pp. 321 – 340, 2004.

[94] A. D. S. for the Department of Health and Ageing, "Guidelines for the management of diabetic retinopathy," 2008. [Online]. Available: http://www.icoph.org/downloads/Diabetic$-$Retinopathy$-$Detail.pdf

[95] C. I. Sanchez, M. Niemeijer, A. V. Dumitrescu, M. S. A. Suttorp-Schulten, M. D. Abramoff, and B. van Ginneken, "Evaluation of a computer-aided diagnosis system for diabetic retinopathy screening on public data," *Investigative Ophthalmology and Visual Science*, vol. 52, no. 7, pp. 4866–4871, 2011.

[96] A. Bhalerao, A. Patanaik, S. Anand, and P. Saravanan, "Robust detection of microaneurysms for sight threatening retinopathy screening," in *Sixth Indian Conference on Computer Vision, Graphics Image Processing, 2008. ICVGIP '08*, Dec. 2008, pp. 520 –527.

[97] A. Sopharak, B. Uyyanonvara, S. Barman, and T. H. Williamson, "Automatic detection of diabetic retinopathy exudates from non-dilated retinal images using mathematical morphology methods," *Computerized Medical Imaging and Graphics*, vol. 32, no. 8, pp. 720 – 727, 2008.

[98] T. Walter, J.-C. Klein, P. Massin, and A. Erginay, "A contribution of image processing to the diagnosis of diabetic retinopathy-detection of exudates in color fundus images of the human retina," *IEEE Transactions on Medical Imaging*, vol. 21, no. 10, pp. 1236 –1243, Oct. 2002.

[99] D. Welfer, J. Scharcanski, and D. R. Marinho, "A coarse-to-fine strategy for automatically detecting exudates in color eye fundus images," *Computerized Medical Imaging and Graphics*, vol. 34, no. 3, pp. 228 – 235, 2010.

[100] M. Esnaashari, S. A. Monadjemi, and G. Naderian, "A content-based retinal image retrieval method for diabetes-related eye diseases diagnosis," in *International Journal of Research and reviews in Computer Science*, vol. 2, no. 6, 2011, pp. 1222–1227.

[101] B. Antal and A. Hajdu, "An ensemble-based system for microaneurysm detection and diabetic retinopathy grading," *IEEE Transactions on Biomedical Engineering*, vol. 59, no. 6, pp. 1720 –1726, June 2012.

[102] E. Barriga, V. Murray, C. Agurto, M. Pattichis, W. Bauman, G. Zamora, and P. Soliz, "Automatic system for diabetic retinopathy screening based on am-fm, partial least squares, and support vector machines," in *IEEE International Symposium on Biomedical Imaging: From Nano to Macro*, April 2010, pp. 1349 –1352.

[103] C. Agurto, E. Barriga, V. Murray, S. Nemeth, R. Crammer, W. Bauman, G. Zamora, M. Pattichis, and P. Soliz, "Automatic detection of diabetic retinopathy and age-related macular degeneration in digital fundus images," *Invest Ophthalmol Vis Sci.*, vol. 52, no. 8, pp. 5862 –5871, July 29 2011.

[104] R. Acharya U, C. K. Chua, E. Y. Ng, W. Yu, and C. Chee, "Application of higher order spectra for the identification of diabetes retinopathy stages," *J. Med. Syst.*, vol. 32, no. 6, pp. 481–488, Dec 2008.

[105] U. R. Acharya, C. M. Lim, E. Y. K. Ng, C. Chee, and T. Tamura, "Computer-based detection of diabetes retinopathy stages using digital fundus images," *Proceedings of the Institution of Mechanical Engineers, Part H: Journal of Engineering in Medicine*, vol. 223, no. 5, pp. 545–553, 2009.

[106] D. Usher, M. Dumskyj, M. Himaga, T. H. Williamson, S. Nussey, and J. Boyce, "Automated detection of diabetic retinopathy in digital retinal images: a tool for diabetic retinopathy screening," *Diabetic Medicine*, vol. 21, no. 1, pp. 84–90, 2004.

[107] Y. Sun, M. S. Kamel, A. K. Wong, and Y. Wang, "Cost-sensitive boosting for classification of imbalanced data," *Pattern Recognition*, vol. 40, no. 12, pp. 3358 – 3378, 2007.

[108] D. Williams, V. Myers, and M. Silvious, "Mine classification with imbalanced data," *IEEE Geoscience and Remote Sensing Letters*, vol. 6, no. 3, pp. 528–532, 2009.

[109] Y. Yang, "An evaluation of statistical approaches to text categorization," *Journal of Information Retrieval*, vol. 1, pp. 67–88, 1999.

[110] N. E. Institute, "Facts about diabetic retinopathy." [Online]. Available: http://www.nei.nih.gov/health/diabetic/retinopathy.asp

[111] M. Friedlander, "Fibrosis and diseases of the eye," *The Journal of Clinical Investigation*, vol. 117, no. 3, pp. 576–586, 3 2007.

[112] K. Goatman, A. Fleming, S. Philip, G. Williams, J. Olson, and P. Sharp, "Detection of new vessels on the optic disc using retinal photographs," *IEEE Transactions on Medical Imaging*, vol. 30, no. 4, pp. 972–979, 2011.

[113] A. Karperien, H. Jelinek, J. Leandro, J. Soares, R. J. Cesar, and A. Luckie, "Automated detection of proliferative retinopathy in clinical practice," *Clin Ophthalmol*, vol. 2(1), pp. 109–122, 2008.

[114] M. Akram, I. Jamal, A. Tariq, and J. Imtiaz, "Automated segmentation of blood vessels for detection of proliferative diabetic retinopathy," in *IEEE-EMBS International Conference on Biomedical and Health Informatics (BHI)*, Jan 2012, pp. 232–235.

[115] S. Roychowdhury, D. Koozekanani, and K. Parhi, "Blood vessel segmentation of fundus images by major vessel extraction and sub-image classification," *IEEE Journal of Biomedical and Health Informatics*, 2014.

[116] ——, "Iterative vessel segmentation of fundus images," *IEEE Transactions on Biomedical Engineering (submitted)*, 2014.

[117] W. H. Organization, "Vision 2020 action plan for 2006 to 2011 planning meeting." Geneva. 11 July 2006.

[118] S. Roychowdhury, D. Koozekanani, S. Radwan, and K. Parhi, "Automated localization of cysts in diabetic macular edema using optical coherence tomography images," in *35th Annual International Conference of the IEEE Engineering in Medicine and Biology Society (EMBC)*, July 2013, pp. 1426–1429.

[119] G. Wilkins, O. Houghton, and A. Oldenburg, "Automated segmentation of intraretinal cystoid fluid in optical coherence tomography," *IEEE Transactions on Biomedical Engineering*, vol. 59, no. 4, pp. 1109 –1114, April 2012.

[120] A. Gandorfer, C. Haritoglou, A. Gandorfer, and A. Kampik, "Retinal damage from indocyanine green in experimental macular surgery," *Investigative Ophthalmology and Visual Science*, vol. 44, no. 1, pp. 316–323, 2003.

[121] L. Zhao, A. E. Elsner, C. A. Clark, T. Y. Chui, J. A. Papay, B. P. Haggerty, D. A. VanNasdale, and S. A. Burns, "Semi-automatic OCT segmentation of nine retinal layers," *ARVO*, no. 4092/D1180, 2012.

[122] B. J. Antony, M. D. Abràmoff, M. M. Harper, W. Jeong, E. H. Sohn, Y. H. Kwon, R. Kardon, and M. K. Garvin, "A combined machine-learning and graph-based framework for the segmentation of retinal surfaces in sd-oct volumes," *Biomed. Opt. Express*, vol. 4, no. 12, pp. 2712–2728, Dec 2013.

[123] J. Y. Lee, S. J. Chiu, P. P. Srinivasan, J. A. Izatt, C. A. Toth, S. Farsiu, and G. J. Jaffe, "Fully automatic software for retinal thickness in eyes with diabetic macular edema from images acquired by cirrus and spectralis systems," *Investigative Ophthalmology and Visual Science*, vol. 54, no. 12, pp. 7595–7602, 2013.

[124] K. A. R. R. Afef Maalej, Wathek Cheima and G. Salem, "Optical coherence tomography for diabetic macular edema: Early diagnosis, classification and quantitative assessment," *Journal of Clinical and Experimental Ophthalmology*, vol. 0, no. 0, pp. –, 2013.

[125] T. Otani, S. Kishi, and Y. Maruyama, "Patterns of diabetic macular edema with optical coherence tomography," *American Journal of Ophthalmology*, vol. 127, no. 6, pp. –, 1999.

[126] R. Lattanzio, "Macular thickness measured by optical coherence tomography (oct) in diabetic patients," *European journal of ophthalmology*, vol. 12, no. 6, pp. 482–487, 2002.

[127] J. Rogowska and M. E. Brezinski, "Image processing techniques for noise removal, enhancement and segmentation of cartilage OCT images," *Phys. Med. Biol.*, vol. 47, no. 4, pp. 641–655, 2002.

[128] D. C. Adler, T. H. Ko, and J. G. Fujimoto, "Speckle reduction in optical coherence tomography images by use ofa spatially adaptive wavelet filter," *Opt. Lett.*, vol. 29, no. 24, pp. 2878–2880, Dec 2004.

[129] S. Chitchian, M. A. Mayer, A. R. Boretsky, F. J. van Kuijk, and M. Motamedi, "Retinal optical coherence tomography image enhancement via shrinkage denoising using double-density dual-tree complex wavelet transform," *Journal of Biomedical Optics*, vol. 17, no. 11, pp. 116 004–116 009, 2012.

[130] L. Fang, S. Li, Q. Nie, J. A. Izatt, C. A. Toth, and S. Farsiu, "Sparsity based denoising of spectral domain optical coherence tomography images," *Biomed. Opt. Express*, vol. 3, no. 5, pp. 927–942, May 2012.

[131] D. Koozekanani, K. L. Boyer, and C. Roberts, "Retinal thickness measurements from optical coherence tomography using a markov boundary model," *IEEE Trans. Med. Imaging*, vol. 20, no. 9, pp. 900–916, 2001.

[132] H. Ishikawa, D. M. Stein, G. Wollstein, S. Beaton, J. G. Fujimoto, and J. S. Schuman, "Macular segmentation with optical coherence tomography," *Investigative Ophthalmology and Visual Science*, vol. 46, no. 6, pp. 2012–2017, 2005.

[133] A. M. Bagci, M. P. N. Shahidi, R. Ansari, M. Blair, N. P. Blair, and R. Zelkha, "Thickness profiles of retinal layers by optical coherence tomography image segmentation," *American Journal of Ophthalmology*, vol. 146, no. 5, pp. 679–687, Aug 2008.

[134] A. Mishra, A. Wong, K. Bizheva, and D. A. Clausi, "Intra-retinal layer segmentation in optical coherence tomography images," *Opt. Express*, vol. 17, no. 26, pp. 23 719–23 728, Dec 2009.

[135] M. Garvin, M. Abramoff, R. Kardon, S. Russell, X. Wu, and M. Sonka, "Intraretinal layer segmentation of macular optical coherence tomography images using optimal 3-d graph search," *IEEE Transactions on Medical Imaging*, vol. 27, no. 10, pp. 1495–1505, 2008.

[136] S. J. Chiu, X. T. Li, P. Nicholas, C. A. Toth, J. A. Izatt, and S. Farsiu, "Automatic segmentation of seven retinal layers in sdoct images congruent with expert manual segmentation," *Opt. Express*, vol. 18, no. 18, pp. 19 413–19 428, Aug 2010.

[137] S. Roychowdhury, D. D. Koozekanani, and K. K. Parhi, "Automated denoising and segmentation of optical coherence tomography images," in *Asilomar Conference on Signals, Systems and Computers*, Nov 2013, pp. 258–262.

[138] Y. Liu, Y. Liang, G. Mu, and X. Zhu, "Deconvolution methods for image deblurring in optical coherence tomography," *J. Opt. Soc. Am. A*, vol. 26, no. 1, pp. 72–77, Jan 2009.

[139] C. Wagner and I. Selesnick, "Double density wavelet software." [Online]. Available: http://taco.poly.edu/selesi/DoubleSoftware/

[140] "A threshold selection method from gray-level histograms," *IEEE Transactions on Systems, Man and Cybernetics*, vol. 9, no. 1, pp. 62–66, Jan 1979.

[141] R. Kafieh, H. Rabbani, F. Hajizadeh, M. D. Abramoff, and M. Sonka, "Thickness mapping of eleven retinal layers in normal eyes using spectral domain optical coherence tomography," *arXiv:1312.3199*, Dec 2013.

[142] Q. Yang, C. A. Reisman, Z. Wang, Y. Fukuma, M. Hangai, N. Yoshimura, A. Tomidokoro, M. Araie, A. S. Raza, D. C. Hood, and K. Chan, "Automated layer segmentation of macular oct images using dual-scale gradient information," *Opt. Express*, vol. 18, no. 20, pp. 21 293–21 307, Sep 2010.